Manuscript Details

Manuscript number	ORGEO_2018_496
Title	Multiple Mineralization Events in the Zacatecas Ag-Pb-Zn-Cu-Au District, and Their Relationship to the Tectonomagmatic Evolution of the Mesa Central, Mexico
Article type	Research paper

Abstract

Mineralization in the Zacatecas district is polymetallic (Ag, Zn, Pb, Cu, and Au) and occurs as skarn-type and epithermal veins formed in different metallogenetic stages. The oldest mineralization in the district is skarn-type, Cu-rich with lesser Zn-Pb-Ag, and is considered to be close in age to felsic dikes and plugs dated at ~51 Ma. Epithermal mineralization occurs in both low- and intermediate-sulfidation styles. Intermediate-sulfidation veins (the Veta Grande, Mala Noche, El Bote, and La Cantera veins) are polymetallic, Ag-rich, hosted in ESE- to SE-striking structures, and were formed at ~42 Ma (adularia 40Ar/39Ar isochron age from Veta Grande of 42.36 ± 0.18 Ma; 2□, MSWD = 0.76). Low-sulfidation Au-(Ag) mineralization occurs in the N–S-trending El Orito vein system, which yielded an adularia 40Ar/39Ar isochron age of 29.19 ± 0.20 Ma (2□, MSWD = 1.8). These ages and the differences in structural orientation indicate that the two styles of epithermal mineralization are temporally and tectonically unrelated. The mineral paragenesis of the Mala Noche deposit consists of early skarn-type Cu mineralization overprinted by later epithermal Pb-Zn-Ag veins. Skarn-type minerals include relicts of prograde silicate minerals (diopside, hedenbergite, and garnet), retrograde silicate minerals (ilvaite, grunerite, stilpnomelane, epidote, clinochlore), and ore minerals (chalcopyrite, pyrite, sphalerite, galena, magnetite, wolframite, and minor bismuthinite). Epithermal mineralization is characterized by layered to vuggy quartz veins and breccias, with phyllic wallrock alteration (quartz, sericite-illite). The veins consist of quartz, calcite, dolomite, and ankerite with variable amounts of base metal sulfides (sphalerite, galena, pyrite, minor chalcopyrite, and rare acanthite and stromeyerite). The Veta Grande epithermal mineralization was emplaced in two main stages of Ag-rich quartz veining, with narrow selvedges of phyllic (quartz-sericite) wallrock alteration. Stage I consist of quartz, calcite, and minor adularia intergrown with pyrite, followed by sphalerite, galena, and lesser chalcopyrite, acanthite, pyrargyrite, and jamesonite. Stage II mineral paragenesis is similar to stage I but is characterized by amethystine quartz and contains less abundant sulfide minerals. The ore mineral paragenesis of the El Compas vein, within the El Orito System, consists of quartz, adularia, calcite, and chalcedony with minor pyrite, followed by rare aguilarite, naumannite, electrum, and native gold. The skarn-type and intermediate-sulfidation mineralization is coeval with Eocene subduction-related magmatism in the Zacatecas area, which is constrained by zircon U-Pb ages for igneous rocks between 51–42 Ma. The emplacement of these magmas was controlled by the same regional-scale, ESE- to SE-trending, transtensional structures that controlled the skarn-type and intermediate-sulfidation deposits. This mineralization is thus interpreted to be related to the last stages of subduction volcanism in central Mexico, under transtensional stress conditions. In contrast, no nearby magmatism is clearly related to the Oligocene low-sulfidation system. However, its age and structural orientation (N–S), combined with a regional change in magma composition from Eocene calc-alkaline to Oligocene bimodal volcanism in central Mexico, suggest that the low-sulfidation mineralization is related to post-subduction continental extension processes, reflecting the beginning of Basin and Range tectonics.

Keywords	Zacatecas Mining District Mesa Central Mexican Silver Belt Mineral Deposits 40Ar/39Ar Geochronology U/Pb Geochronology

Corresponding Author	Osbaldo Zamora Vega
Corresponding Author's Institution	University of Alberta, Canada
Order of Authors	Osbaldo Zamora Vega, Jeremy Richards, Terry Spell, Andrew Dufrane, John Williamson

Suggested reviewers	Antonio Arribas, John-Mark Staude, Paul Spry, James Saunders
Opposed reviewers	Stuart Simmons, Antoni Camprubi

Submission Files Included in this PDF

File Name [File Type]

Zamora-Vega et al_2018_OGR_Cover letter.docx [Cover Letter]

Highlights.docx [Highlights]

Graphical abstract.pdf [Graphical Abstract]

Zamora-Vega et al_2018_OGR_manuscript.docx [Manuscript File]

Zamora-Vega et al., 2018_OGR_Figures.docx [Figure]

Zamora-Vega et al., 2018_OGR_Methods and appendix.docx [MethodsX]

To view all the submission files, including those not included in the PDF, click on the manuscript title on your EVISE Homepage, then click 'Download zip file'.

Research Data Related to this Submission

Data set https://data.mendeley.com/datasets/y3rskt5rnc/draft?a=73361bee-0c08-4b49-9e51-bf34b780b4c0

Data for: Multiple Mineralization Events in the Zacatecas Ag-Pb-Zn-Cu-Au District, and Their Relationship to the Tectonomagmatic Evolution of the Mesa Central, Mexico

Description of analytical methods and results of electron microprobe analyses, wole-rock geochemistry, 40Ar/39Ar, U-Pb, and locations and descriptions of samples analyzed for geochemistry and geochronology

May 21, 2018

Dear Franco Pirajno - Editor-in-Chief,

We would like to submit for publication in Ore Geology Reviews the manuscript entitled: Multiple Mineralization Events in the Zacatecas Ag-Pb-Zn-Au District, and Their Relationship to the Tectonomagmatic Evolution of the Mesa Central, Mexico, by O. Zamora-Vega, J.P. Richards, T. Spell, S.A. DuFrane, and J. Williamson.

The Zacatecas district hosts three styles of mineralization including skarn-type, low- and intermediate-sulfidation epithermal deposits. Previous studies have not identified skarn-type and considered the low- and intermediate-sulfidation mineralizing events to be coeval and transitional to each other. In this contribution, we present a detailed mineral paragenesis for each style of mineralization and geochronological ages, Ar/Ar from the low- and intermediate-sulfidation deposits and U/Pb from subvolcanic rocks spatially related to the skarn-type deposit, to show that these mineralizing events are temporarily unrelated. We also compare the geochemistry of volcanic and subvolcanic rocks and structural geology of the Zacatecas district within a regional context to suggest a link between the different styles of mineralization in the Zacatecas district and the tectonomagmatic evolution of the Mesa Central. We hope that this work helps to clarify the relationships between different styles of mineralization in Mexico and their linkages with specific tectonic stress regimes. This paper is intended to provide the framework for a second publication on geochemical modelling for the different styles of mineralization in the Zacatecas district.

Earlier versions of this manuscript were submitted to Economic Geology in 2014 (reviewers David John, Tawn Albinson, and John-Mark Staude), and to Mineralium Deposita in 2015 (reviewers Jim Mortensen and Antoni Camprubi), but were rejected by Stuart Simmons and Georges Beaudoin, respectively, the latter on the basis of what we considered to be an unreasonably harsh review by Camprubi.

We have revised and updated the manuscript based on these reviewers' comments, but we stand by the original data and interpretations. We therefore wish to submit the paper to Ore Geology Reviews, and request that Stuart Simmons and Antoni Camprubi *not* be asked to review this work.

We hope that our manuscript can be considered for publication in Ore Geology Reviews, and will be happy to address any question reviewers may raise.

Sincerely,

Osbaldo Zamora Vega and co-authors

Highlights

- Mineralization in the Zacatecas district is polymetallic (Ag, Zn, Pb, Cu, and Au) and occurs as skarn-type and epithermal veins formed in different metallogenetic stages.
- The oldest mineralization in the district is skarn-type, Cu-rich with lesser Zn-Pb-Ag, and is considered to be close in age to felsic dikes and plugs dated at ~51 Ma.
- The intermediate-sulfidation Veta Grande is are polymetallic, Ag-rich, hosted in ESE- to SE-striking structures, and was formed at 42.36 ± 0.18 Ma (adularia $^{40}Ar/^{39}Ar$ isochron age; 2σ, MSWD = 0.76).
- The low-sulfidation El Compas vein is Au-rich, occurs in the N–S-trending El Orito vein system, and was formed at 29.19 ± 0.20 Ma (adularia $^{40}Ar/^{39}Ar$ isochron age; 2σ, MSWD = 1.8).

a) Deep-seated thrust faults produced during accretion of the Guerrero terrane in the Late Cretaceous

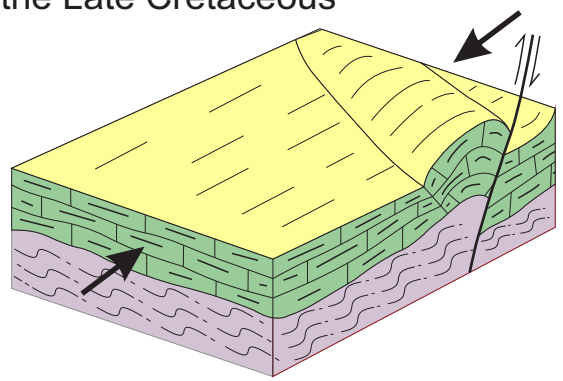

b) Emplacement of felsic dikes and skarn-type mineralization at ~51 Ma

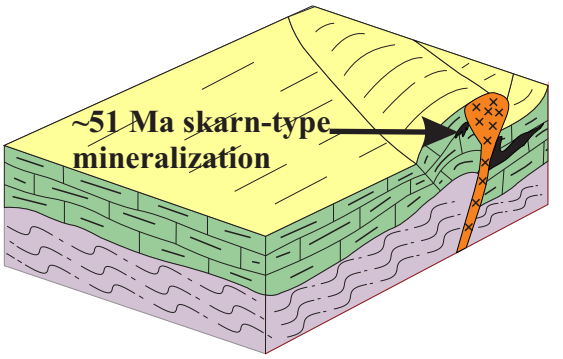

c) Shearing of skarn-type mineralization between ~51 and 48 Ma

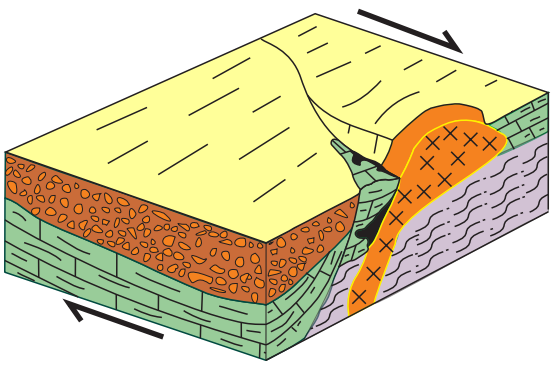

d) Emplacement of felsic dikes and ignimbrites (48-42 Ma) and intermediate-sulfidation veins

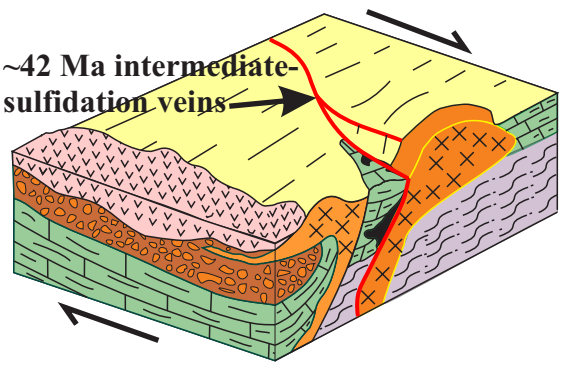

e) Continental extension and emplacement of low-sulfidation veins at ~29 Ma

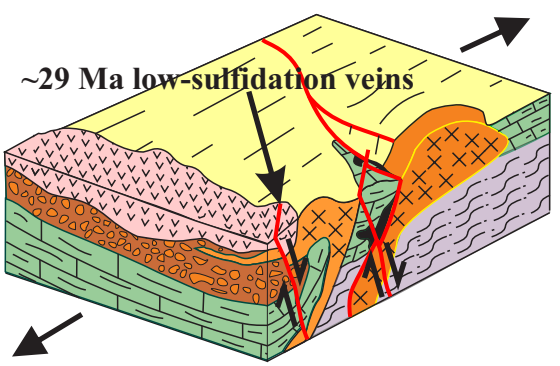

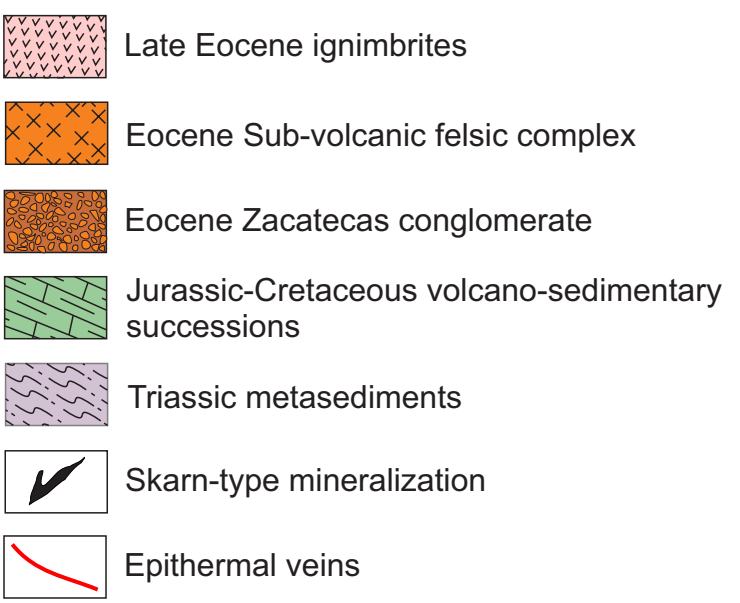

Multiple Mineralization Events in the Zacatecas Ag-Pb-Zn-Cu-Au District, and Their Relationship to the Tectonomagmatic Evolution of the Mesa Central, Mexico

Osbaldo Zamora-Vega[1,4], Jeremy P. Richards[1,2], Terry Spell[3], S. Andrew Dufrane[1], and John Williamson[4]

[1] Department of Earth and Atmospheric Sciences, University of Alberta, Edmonton, Alberta, T6G 2E3, Canada

[2] Mineral Exploration Research Centre, Harquail School of Earth Sciences, Laurentian University, 935 Ramsey Lake Road, Sudbury, Ontario, P3E 2C6, Canada

[3] Department of Geoscience, University of Nevada, Las Vegas, 4505 Maryland Parkway, Las Vegas, Nevada 89154-4010, USA

[4] Altiplano Metals Inc., 201, 8429-24 St NW, Edmonton, Alberta, T6P 1L3, Canada

Keywords:
Zacatecas Mining District
Mesa Central
Mexican Silver Belt
Mineral Deposits
$^{40}Ar/^{39}Ar$ Geochronology
U/Pb Geochronology

Abstract

Mineralization in the Zacatecas district is polymetallic (Ag, Zn, Pb, Cu, and Au) and occurs as skarn-type and epithermal veins formed in different metallogenetic stages. The oldest mineralization in the district is skarn-type, Cu-rich with lesser Zn-Pb-Ag, and is considered to be close in age to felsic dikes and plugs dated at ~51 Ma. Epithermal mineralization occurs in both low- and intermediate-sulfidation styles. Intermediate-sulfidation veins (the Veta Grande, Mala Noche, El Bote, and La Cantera veins) are polymetallic, Ag-rich, hosted in ESE- to SE-striking structures, and were formed at ~42 Ma (adularia $^{40}Ar/^{39}Ar$ isochron age from Veta Grande of 42.36 ± 0.18 Ma; 2σ, MSWD = 0.76). Low-sulfidation Au-(Ag) mineralization occurs in the N–S-trending El Orito vein system, which yielded an adularia $^{40}Ar/^{39}Ar$ isochron age of 29.19 ± 0.20 Ma (2σ, MSWD = 1.8). These ages and the differences in structural orientation indicate that the two styles of epithermal mineralization are temporally and tectonically unrelated.

The mineral paragenesis of the Mala Noche deposit consists of early skarn-type Cu mineralization overprinted by later epithermal Pb-Zn-Ag veins. Skarn-type minerals include

relicts of prograde silicate minerals (hedenbergite and garnets), retrograde silicate minerals (ilvaite, grunerite, stilpnomelane, epidote, clinochlore), and ore minerals (chalcopyrite, pyrite, sphalerite, galena, magnetite, wolframite, and minor bismuthinite). Epithermal mineralization is characterized by layered to vuggy quartz veins and breccias, with phyllic wallrock alteration (quartz, sericite-illite). The veins consist of quartz, calcite, dolomite, and ankerite with variable amounts of base metal sulfides (sphalerite, galena, pyrite, minor chalcopyrite, and rare acanthite and stromeyerite).

The Veta Grande epithermal mineralization was emplaced in two main stages of Ag-rich quartz veining, with narrow selvedges of phyllic (quartz-sericite) wallrock alteration. Stage I consist of quartz, calcite, and minor adularia intergrown with pyrite, followed by sphalerite, galena, and lesser chalcopyrite, acanthite, pyrargyrite, and jamesonite. Stage II mineral paragenesis is similar to stage I but is characterized by amethystine quartz and contains less abundant sulfide minerals.

The ore mineral paragenesis of the El Compas vein, within the El Orito System, consists of quartz, adularia, calcite, and chalcedony with minor pyrite, followed by rare aguilarite, naumannite, electrum, and native gold.

The skarn-type and intermediate-sulfidation mineralization is coeval with Eocene subduction-related magmatism in the Zacatecas area, which is constrained by zircon U-Pb ages for igneous rocks between 51–42 Ma. The emplacement of these magmas was controlled by the same regional-scale, ESE- to SE-trending, transtensional structures that controlled the skarn-type and intermediate-sulfidation deposits. This mineralization is thus interpreted to be related to the last stages of subduction volcanism in central Mexico, under transtensional stress conditions. In contrast, no nearby magmatism is clearly related to the Oligocene low-sulfidation system. However, its age and structural orientation (N–S), combined with a regional change in magma composition from Eocene calc-alkaline to Oligocene bimodal volcanism in central Mexico, suggest that the low-sulfidation mineralization is related to post-subduction continental extension processes, reflecting the beginning of Basin and Range tectonics.

1. Introduction

The Zacatecas district lies within the Mexican Silver Belt, which constitutes the largest silver province in the world. Silver mineralization occurs mainly in epithermal veins, with lesser amounts in related skarn and manto-type replacement bodies. Consequently, epithermal deposits are a major target for precious metal exploration, and understanding their evolution and links with associated intrusive and volcanic rocks is crucial for the development of exploration strategies.

Epithermal gold and silver deposits have been classified as high-, intermediate-, and low-sulfidation types based on the sulfidation states of the observed hypogene sulfide mineral assemblages (Hedenquist et al., 2000; Sillitoe and Hedenquist, 2003; Simmons et al., 2005).Previous studies have documented spatial, and in some cases, genetic relationships between intermediate- and high-sulfidation epithermal deposits, and underlying porphyry-type deposits (Sillitoe, 1999; Hedenquist et al., 2000). Other studies have shown that there is a transition from one type to another (Einaudi et al., 2003). In contrast, low-sulfidation epithermal deposits are generally not considered transitional to intermediate- or high-sulfidation epithermal systems, because they are largely formed in distinct tectonic settings, and are less clearly related to magmatism (Hedenquist et al., 2000; John, 2001; Sillitoe and Hedenquist, 2003). However, Camprubi and Albinson (2007) noted that several of the Mexican deposits have characteristics of both intermediate- and low-sulfidation mineralization styles and, therefore, cannot be classified straightforwardly within the scheme proposed by Hedenquist et al. (2000). Camprubi and Albinson (2007) proposed a new empirical classification scheme for the Mexican deposits based on their depth of formation with respect to the paleo-water table, as determined by fluid inclusion studies (Albinson et al., 2001). This scheme defined three types of deposit: type A forms at greater depths (>1000 m) from relatively high-salinity brines, and displays only intermediate-sulfidation characteristics; type B forms at intermediate depths (400–1000 m), and displays combined characteristics of intermediate- and low-sulfidation mineralization; type C exhibits only low-sulfidation characteristics and forms at shallow depths (<500 m) from dilute fluids. Under this scheme, the Zacatecas, Guanajuato, and Fresnillo ore deposits are classified as type B. The concurrence of intermediate- and low-sulfidation characteristics within a district and even within a single vein was explained by Camprubi and Albinson (2007) as reflecting a transition

from one mineralization style to the other, due to progressive neutralization of the mineralizing fluids by chemical reactions with country rocks.

Based on whole rock K-Ar dates of 4 samples from the El Orito system (26.9 ± 0.7 – 32.7 ± 0.8 Ma) and 9 samples from the Mala Noche system (30.8 ± 0.8 – 47.9 ± 1.2 Ma), Camprubi and Albinson (2007) proposed that the Zacatecas district represents a single prolonged hydrothermal system, which evolved from an intermediate-sulfidation state (Mala Noche and stage I of the Veta Grande vein systems) to a low-sulfidation state (El Orito vein system and stage II of the Veta Grande vein). This model implies that both intermediate- and low-sulfidation systems were formed under the same tectonic regime, and differs from the model developed for the Great Basin metallogenic province in the southwestern USA, where intermediate- and low-sulfidation mineralization have been related to separate calc-alkaline magmatic arc and extensional tectonics, respectively (John, 2001; Sillitoe and Hedenquist, 2003). In contrast, in this study we use $^{40}Ar/^{39}Ar$ dating of adularia from the Veta Grande and the El Compas (El Orito system) veins, and U-Pb dating of zircons from associated subvolcanic rocks to show that the intermediate- and low-sulfidation mineralization systems have different ages, which correspond to different stages in the tectonomagmatic evolution of the Mesa Central.

Figure 1.

2. Regional Geodynamic Setting

The Zacatecas mining district lies on the western border of the Mesa Central physiographic province (Fig. 1). The Mesa Central is an elevated plateau located in central Mexico. It is bounded to the south by the Mexican Volcanic Belt and partially overlaps the Sierra Madre Occidental. The Sierra Madre Occidental formed during the Cretaceous–Miocene as a result of magmatic and tectonic events related to the subduction of oceanic crust (Farallon plate) beneath the North American continent, and intracontinental Basin and Range extension (Ferrari et al., 2007). Eocene–Oligocene mineralization in the Zacatecas district is located within the western part of the Mesa Central, and is closely linked to the tectonic evolution of this region.

The basement in the western part of the Mesa Central consists of volcano-sedimentary successions of the Guerrero terrane, whereas crystalline rocks of the continental Oaxaquia block underlie the eastern part of the Mesa Central (Fig. 1). The western limit of the Oaxaquia block

represents the early Mesozoic continental margin of Mexico (Ortega-Gutiérrez et al., 1995; Keppie et al., 2003; Centeno-García et al., 2008). Siliciclastic turbidites derived from the paleocontinent formed the basement of the Guerrero terrane in the Triassic. This siliciclastic sequence, which includes the Zacatecas Formation, was deformed and metamorphosed to greenschist facies during the first accretion of the Guerrero terrane to the continent in the Early Jurassic (Centeno-García, 2005; Centeno-García et al., 2008, 2011). In the Middle–Late Jurassic, continental arc volcanic and subvolcanic rocks, red beds, and shallow-marine limestone were deposited unconformably on the crystalline basement of Oaxaquia (Jones et al., 1995; Barboza-Gudiño et al., 1998). In the Late Jurassic–Early Cretaceous, back-arc rifting caused partial detachment of the previously accreted Guerrero terrane, and volcano-sedimentary successions along with volcanogenic massive sulfides were deposited in fringing basins (Centeno-García et al., 2011). The units that represent this event in the Zacatecas district are described below as volcano-sedimentary rocks. Some of these volcano-sedimentary sequences, which are part of the Guerrero terrane, have been dated between 157.4 ± 4.1 and 139.7 ± 2.5 Ma (U-Pb on zircon; Mortensen et al., 2008). These volcano-sedimentary successions were finally accreted to the paleocontinental margin during the Late Cretaceous in a compressional arc tectonic setting (Centeno-García, 1993; Talavera-Mendoza et al., 1995; Centeno-García and Silva-Romo, 1997; Centeno-García et al., 2008, 2011). The alternating stages of subduction-collision and rifting produced structurally weak planes that may have served as channels for Eocene magma ascent and the flow of hydrothermal fluids.

Eocene clastic sedimentary and volcanic rocks overlie the Mesozoic basement in southern and western parts of the Mesa Central. Eocene–Oligocene mineralization in the Zacatecas district is located within the Guerrero terrane and is closely related in space and time with the tectonic evolution of the Eocene units. The Tertiary tectono-magmatic history of the Mesa Central has been studied extensively in terms of the relationships between sedimentation, faulting, magmatism, and volcanism (Edwards, 1955; Aguirre-Diaz and Labarthe-Hernandez, 2003; Nieto-Samaniego et al., 2005, 2007; Aranda-Gomez et al., 2007; Tristan-Gonzalez et al., 2009; Escalona-Alcázar, et al., 2016); a brief summary is provided below.

2.1 Late Cretaceous–Early Cenozoic (Laramide Orogeny)

The final accretion of the Guerrero terrane to the Mexican continental margin took place during the Late Cretaceous–early Cenozoic as part of the Laramide orogeny, and caused deformation and eastward shortening of the epicontinental Mesozoic sequences (Centeno-García, 1993; Talavera-Mendoza et al., 1995; Centeno-García et al., 2008).

The timing of the end of the Laramide compression in northern Mexico and the Mesa Central has been constrained by K-Ar and $^{40}Ar/^{39}Ar$ ages of undeformed intrusive rocks to between 55 and 43 Ma (Mujica-Mondragon and Jacobo-Albarran, 1983; Stein et al., 1993; Aranda-Gomez et al., 2007; Sole et al., 2007; Tristan-Gonzalez, 2008; Tristan-Gonzalez et al., 2009). The El Peñón Blanco granite (muscovite $^{40}Ar/^{39}Ar$ age of 50.94 ± 0.47 Ma; Aranda-Gomez et al., 2007) is the closest example of this magmatism to the Zacatecas district (located ~100 km to the southeast).

2.2 Eocene Continental Sedimentation and Volcanism (Transitional Tectonics)

Sedimentary basins associated with normal and/or strike-slip faults were developed throughout central and southern Mexico during the Eocene after the end of the Laramide orogeny as a result of a change in stress regime from compressional to tensional (Edwards, 1955; Aranda-Gomez and McDowell, 1998; Aranda-Gomez et al., 2007; Tristan-Gonzalez, 2009). These basins were filled with detritus eroded from basement rocks, granites, and volcanic rocks to produce red-bed conglomerates (Fig. 2).

Figure 2.

The presence of clasts of Laramide-type granite in these conglomerate sequences confirms that exhumation and denudation happened after the end of the compressional regime (Edwards, 1955; Aranda-Gomez et al., 2007). These conglomerates have been interpreted to be fanglomerates deposited near normal faults, and related to the first period of extension immediately after the Laramide orogeny (Edwards, 1955; Aranda-Gómez and McDowell, 1998). According to Tristan-Gonzales et al. (2009), the Eocene shift from compression (Laramide orogeny) to extension (Basin and Range) in the Mesa Central was separated by a period of crustal stress relaxation. Dextral strike-slip movements produced uplift of NNE-oriented ranges

in the Mesa Central, and subsequent ESE- to SE-trending high-angle normal faults cut these ranges in the middle Eocene (Tristan-Gonzalez, 2008; Tristan-Gonzalez et al., 2009). These faults served as channelways for the emplacement of dikes and domes of felsic rocks, and for the formation of associated intermediate-sulfidation hydrothermal systems.

Andesitic lava flows and felsic pyroclastic rocks intercalated with red beds at different levels show that volcanism was episodic during the life of the basins. In the Guanajuato district, mafic volcanic lavas intercalated with clastic sedimentary sequences were dated at 49.3 ± 1.0 Ma (K-Ar on whole rock; Aranda-Gomez and McDowell, 1998). The oldest volcanic unit overlying the Fresnillo conglomerate has been dated at 44.73 ± 0.04 Ma ($^{40}Ar/^{39}Ar$ on sadinine; Velador et al., 2010). In the Zacatecas district, pyroclastic rocks interfingered with red bed layers on top of the conglomeratic sequence were dated at 46.8 Ma (K-Ar on biotite; Ponce et al., 1988; no error reported). These pyroclastic rocks were followed by effusive felsic volcanism emplaced along reactivated SE-trending faults (Tristan-Gonzalez et al., 2009). These dates are confirmed here by U-Pb zircon ages for felsic hypabyssal and volcanic rocks in the Zacatecas district ranging from 51–42 Ma (see below). Recently, in a detailed study of the Zacatecas red conglomerate, Escalona-Alcázar et al. (2016) proposed a Palaeocene to early Oligocene depositional age based on detrital and magmatic zircons.

Eocene calc-alkaline intermediate to felsic magmas appear to have been generated during the last stages of subduction of the Farallon plate beneath the North American plate, in a mildly extensional continental arc (Atwater, 1989; Aguirre-Díaz and McDowell, 1991; Ferrari et al., 1999; Tristan-Gonzalez et al., 2009). Early stages of skarn-type, manto replacement, and epithermal Ag-Pb-Zn-Cu mineralization are spatially related to this magmatism, and a temporal relationship is inferred (Rubin and Kyle, 1988; Cannet et al., 2009).

2.3 Basin and Range

The Basin and Range province extends from the northern Rocky Mountains in the United States to the Trans-Mexican volcanic belt, and includes the Mesa Central province (Fig. 1; Henry and Aranda-Gomez, 1992; Stewart, 1998; Aranda-Gómez et al., 2000). This physiographic province is characterized by alternating NNW- to NNE-trending narrow mountain ranges and block-faulted valleys, produced by extensional tectonics that began in the Eocene or as early as the Paleocene (Stewart, 1998; Aranda-Gomez et al., 2000). Extension was initiated in western

North America by collision of the East Pacific spreading center with the North American plate (Atwater, 1989; Aguirre-Díaz and McDowell, 1991; Henry and Aranda-Gomez, 1992; Dickinson, 2006; Ferrari et al., 2007), which produced a change from a subduction to a transform boundary along the plate margin. During and after the waning stages of subduction, extension developed gradually and episodically with systematically different timing, style, and magnitude from one area to another along the Basin and Range province (Stewart, 1998; Aranda-Gomez et al., 2000). Stewart (1998) divided the Basin and Range province into eleven regions based on their physiographic and structural characteristics, within a region that extends from the southwest USA to Guanajuato in central Mexico. The Mesa Central is structurally characterized by grabens, half grabens, horsts, and locally tilted blocks concentrated on the eastern margin of the Sierra Madre Occidental (Figs. 1 and 2; Aranda-Gomez, 1989; Aranda-Gomez et al., 1989; Henry et al., 1989; Henry and Aranda-Gomez, 1992; Stewart, 1998).

The timing of the onset of Basin and Range extension in the Mesa Central has been constrained to between 32 and 28 Ma by dating of extensional hydrothermal veins and tilting (Henry and Aranda-Gomez, 1992; Aguirre-Diaz and McDowell, 1993). Late Au-rich epithermal mineralization in Zacatecas is here dated at 29.19 ± 0.20 Ma (see below), and appears to be related to the start of this extensional tectonic phase.

Magma composition also changed at this time from dominantly felsic subalkaline to felsic peraluminous and/or to bimodal styles, with the extrusion of rhyolitic and basaltic magmas along NNE- and NNW-trending normal faults related to grabens at about 29 Ma (Orozco-Esquivel et al., 2002; Rodriguez-Rios et al., 2007; Tistan-Gonzalez et al., 2009). The main bimodal volcanic events occurred between 28 and 26 Ma, but several younger pulses occurred intermittently until the Quaternary (Fig. 2; McDowell and Keizer 1977; Nieto-Samaniego et al., 2007). In the northwestern part of the Mesa Central (Durango state area), basalt lava flows dated at 29 ± 0.60 Ma (McDowell and Keizer 1977) are coeval with rhyolitic tuff, whereas in the southeastern part (San Luis Potosi state area) a rhyolite intercalated with basaltic lavas was dated at 27.6 ± 0.60 Ma (Orozco-Esquivel et al., 2002). No volcanic rocks of this age occur in the immediate Zacatecas area, but Oligocene rhyolitic and basaltic rocks have been mapped ~20 km to the southwest of Zacatecas.

Measurements of heat flow in the states of Chihuahua, Durango, and Zacatecas, which are comparable to those associated with the Rio Grande Rift anomaly in New Mexico, suggest

the presence of an incipient rift in the Mesa Central (Smith and Jones, 1979). This inference is consistent with the interpretation from seismic and gravimetric studies that the crust under the Mesa Central is thinner (~8 km) than adjacent areas (Nieto-Samaniego et al., 2005).

Topaz-bearing rhyolites enriched in silica, potassium, and fluorine in the Mesa Central, have been compared with the fluorine-rich rhyolites genetically associated with the extensional regimes of the Rio Grande rift and the Basin and Range Province in western USA (Christiansen et al., 1986; Orozco-Esquivel et al., 2002; Rodriguez-Rios et al., 2007). Topaz rhyolites in Mexico are between 32 and 27 Ma-old and are widely distributed near the eastern limit of the Sierra Madre Occidental Volcanic Province in the states of Durango, Zacatecas, and San Luis Potosí (Fig. 2; Orozco-Esquivel et al., 2002; Rodriguez-Rios et al., 2007). In the southern part of the Mesa Central (San Luis Potosí and Guanajuato), eruption of effusive rhyolites geochemically similar to these topaz-bearing rhyolites recorded a change in magma composition at about 30 Ma (Orozco-Esquivel et al., 2002). This geochemical marker has allowed the distinction between lower and upper felsic volcanic sequences. The lower felsic volcanic sequence is similar to high-K felsic rocks of the eastern Sierra Madre Occidental and hypabyssal rocks of the Zacatecas district. The upper volcanic sequence is characterized by high-silica peraluminous rhyolites with strong enrichment in fluorine and lithophile elements (Rb, Th, U, Nb, Ta, Y, rare earth elements), and strong depletion in Sr, Ba, and Eu (Orozco-Esquivel et al., 2002). These geochemical changes are attributed to high melting rates in the lower crust promoted by the beginning of crustal extension at high strain rates, documented for the Mesa Central at about 30–29 Ma (Christiansen et al., 1986; Orozco-Esquivel et al., 2002; Rodriguez-Rios et al., 2007; Tristan-Gonzalez et al., 2009). The low-sulfidation epithermal system in the Zacatecas district was developed within this period of time (see below).

2.4 The Mexican Silver Belt

Silver mineralization in central Mexico occurs as skarn, manto-type replacements bodies, chimney-like bodies, and epithermal veins, and is widely distributed from Sonora to Oaxaca. The systems define a ~1500 km-long NW-trending belt that includes the world-class mining districts of Zacatecas, Guanajuato, and Fresnillo along the east border of the Mesa Central (Fig. 1). The belt includes both Ag-Pb-Zn and Au-Ag metallogenic provinces (as defined by Clark et al., 1982) and is spatially and temporally associated with the Sierra Madre Occidental volcanic

province (Fig. 1; Damon et al., 1981; Clark et al., 1982; Camprubi et al., 2003; Camprubi and Albinson, 2007; Camprubi, 2009).

The Mexican epithermal deposits have been characterized based on their fluid inclusion compositions and relative metal contents, and grouped broadly into polymetallic (Ag-Pb-Zn) and Au-Ag-rich deposits (Fig. 3; Albinson et al., 2001). The Au-Ag-rich deposits are characterized by lower salinity fluids (0 to ~7.5 wt.% NaCl eq.), whereas polymetallic deposits have fluids with higher salinities between ~7.5 and 23 wt.% NaCl eq. (Albinson et al., 2001; Camprubi and Albinson, 2007). Camprubi and Albinson (2007) classified the Au-Ag-rich deposits as type C, equivalent to low-sulfidation type according to the criteria of Hedenquist et al. (2000), and the polymetallic deposits as type A and/or B (equivalent to intermediate-sulfidation type or combined intermediate- and low-sulfidation, respectively). Under this scheme, the Zacatecas, Guanajuato, and Fresnillo ore deposits are classified as type B.

Figure 3.

A compilation of ages for Mexican epithermal deposits shows that low-sulfidation Au-Ag-rich deposits are mostly younger than ~30 Ma, whereas the intermediate-sulfidation polymetallic deposits are mostly older than this age (Fig. 3; Albinson et al., 2001; Camprubi et al., 2003; this study), indicating a regional change in metallogenic style.

The formation of the various types of epithermal mineralization in Mexico has been related to periods of subduction-related, continental arc magmatism (Clark et al., 1982; Simmons, 1991; Randall et al., 1994; Camprubi et al., 2003; Camprubi and Albinson, 2007; Velador et al., 2010). Although this model fits for the polymetallic mineralization, the Au-Ag deposits appear instead to be related to later, post-subduction continental extension processes (see below).

2.4.1 Eocene Ag-Pb-Zn-Cu Mineralization

Eocene Ag-Pb-Zn-Cu mineralization in the Mesa Central occurs as skarn, chimney-, and manto-type deposits, and ESE- toSE-trending epithermal Ag-Pb-Zn intermediate-sulfidation veins that locally overprint skarn-type mineralization (Albinson, 1988; Lang et al., 1988; Rubin and Kyle, 1988; Nieto-Samaniego et al., 2007; Cannet et al., 2009). This mineralization is related to intermediate–felsic subvolcanic and intrusive bodies dated between 32 and 46.6 Ma (e.g., the

San Martin, Francisco I. Madero, La Colorada, Fresnillo-Fortuna, Guanajuato, Charcas, and La Paz deposits; Fig. 2).

The San Martin skarn deposit and associated epithermal veins have been genetically related to a 46.2 ± 1 Ma quartz monzonite stock (K-Ar on biotite; Damon et al., 1981; Rubin and Kyle, 1988). Skarn-type mineralization in the La Colorada and Francisco I. Madero deposits has been related to porphyritic sills and ESE- to SE-trending dikes that range in composition from diorite to tonalite, and granite (Moller et al., 2001; Cannet et al., 2009).

In the Fresnillo district, mesothermal Ag-Pb-Zn skarn and manto-type replacement bodies are related to a quartz-monzonite stock. Crosscutting relationships between the stock, manto, and veins indicate that the richer epithermal Ag-Pb-Zn veins are younger than the mesothermal deposits (De Cserna, 1976). Epithermal silver-rich mineralization has been interpreted to be formed in two separate hydrothermal pulses between 31.0 ± 0.6 and 29.1 ± 0.6 Ma (whole rock K-Ar), associated with subduction-related magmatism (Lang et al., 1988).

A similar succession of mineralizing events occurred in the Guanajuato district, starting with skarn development at 55 ± 4 Ma (K-Ar; Randall et al., 1994) related to a granite intrusion. The oldest Ag-Pb-Zn epithermal system has been dated between 30.7 ± 3 and 28.3 ± 5 Ma, and the youngest between 29.2 ± 2 and 27.0 ± 0.4 Ma (whole rock K-Ar ages; Gross, 1975). However, these dates may not be accurate because the younger hydrothermal systems may have caused disturbance of the K-Ar system. The age of the older mineralization is probably greater than the reported age, and has been related to volcanic activity that ranges from 37.0 ± 3 to 32.1 ± 1 Ma (Gross, 1975).

Based on K/Ar dating of volcanic rocks, intrusive bodies, and hydrothermal alteration, Albinson (1988) has estimated a preferred age range of between 35 and 30 Ma for the formation of epithermal Ag-Pb-Zn mineralization in the Mesa Central.

In the Zacatecas area, previous studies have indicated ages for Ag-Pb-Zn mineralization of between 35.5 and 31.1 Ma (K/Ar, no uncertainty reported; Krueger, 2000, reported in Camprubi and Albinson, 2007). However, a new date of 42.36 ± 0.18 Ma ($^{40}Ar/^{39}Ar$ on adularia; see details below) indicates an older timing for mineralization in the area.

2.4.2 Oligocene Au-Ag Mineralization

Gold-rich mineralization in the Mesa Central occurs principally in low-sulfidation epithermal deposits. This style of mineralization occurs as Au-Ag-rich quartz veins mainly controlled by NNE- to NNW-striking normal faults (e.g., Bolañitos in Guanajuato, and Pinos and El Orito System in Zacatecas; Figs. 4 and 5; Steel, 2012; Munroe, 2014). Low-sulfidation styles of mineralization also occur in paragenetically late stages of NW-striking Ag-Pb-Zn veins (e.g., Fresnillo-Southwest area; Velador, 2010), or in late NE-striking veins crosscutting Ag-Pb-Zn intermediate-sulfidation veins at high angles (e.g., Guanajuato; Randall et al., 1994).

Figure 4.

Radiometric ages of mineralization in the Mesa Central have been reported only from the Fresnillo, Guanajuato, and Zacatecas areas. In the Fresnillo-Southwest area, Au-Ag-rich quartz veins that paragenetically postdate the main stage of Ag-Pb-Zn mineralization have been dated at 29.75 ± 0.12 and 29.68 ± 0.10 Ma ($^{40}Ar/^{39}Ar$ on adularia; Velador, 2010; Velador et al., 2010). The youngest volcanic event in the Fresnillo district occurred at 31.04 ± 0.05 Ma ($^{40}Ar/^{39}Ar$ on sanidine; Velador et al., 2010), suggesting that the Au-Ag-rich mineralization is not temporally associated with local volcanism. In the Guanajuato district, the San Nicolas mid-Oligocene Au-Ag-rich deposit is also low-sulfidation in style; it is rich in Se-bearing minerals, electrum, and adularia, and practically devoid of base metal sulfides. The mineralization occurs in veins controlled by NE-trending normal faults, and crosscuts older SE-striking Ag-Pb-Zn veins. It is spatially related to coeval latite and rhyolitic dikes and domes controlled by similar NE-trending structural systems (Randall et al., 1994).

In the Zacatecas area, the Au-Ag-rich low-sulfidation El Orito system was formed in predominantly N–S-striking normal faults, cross-cutting the ESE- to SE-striking strike-slip faults that controlled the Eocene Ag-Pb-Zn intermediate-sulfidation veins. Four K-Ar ages obtained from adularia-rich samples of the El Compas veins range from 26.9 ± 0.7 to 32.7 ± 0.8 (Kapusta, 2006). However, in this study, we obtained an age of 29.19 ± 0.20 Ma ($^{40}Ar/^{39}Ar$ on adularia; see details below) from one of these veins, suggesting that they in fact belong to the Oligocene metallogenetic stage.

3. Geology of the Zacatecas District

The Zacatecas mining district is located in the central part of the state of Zacatecas in central Mexico, and comprises the mineralized zones of El Orito, El Bote, La Cantera, Mala Noche, and Veta Grande (Fig. 5). Several authors have described the geology of the Zacatecas mining district since its discovery in 1546 (Burckhardt, 1906; Maldonado-Koerdell, 1948; Perez-Martinez et al., 1961; Ponce and Clark, 1988; Caballero-Martinez, 1999). The litho-stratigraphic units that crop out in the district range from Triassic to Oligocene, with Quaternary fill in graben to the east and west of the Zacatecas horst block. All of these units (except the Quaternary cover) host epithermal vein mineralization, but the majority of veins are located in the Jurassic–Cretaceous sequence or along faulted contacts with the Zacatecas conglomerate (Fig. 5).

Figure 5.

3.1 Triassic

The Triassic Zacatecas Formation is a clastic marine sequence, and crops out in a tectonic window near the city of Zacatecas (Fig. 5). It consists of metamorphosed (greenschist facies) pelites, sandstone, and conglomerate, with minor recrystallized limestone and basaltic pillow lavas (Fig. 6a; Ranson, 1975; Ranson et al., 1982; Centeno-Garcia and Silva-Romo, 1997). Abundant fossil content indicates a Late Triassic (Carnian) age for this formation (Burckhardt, 1906; Maldonado-Koerdell, 1948). This formation has been interpreted to be the basement of the Guerrero terrane in the Mesa Central (Centeno-Garcia et al., 2008) and is unconformably overlain by Late Jurassic–Early Cretaceous marine volcano-sedimentary successions.

Figure 6.

3.2 Jurassic–Cretaceous

Late Jurassic–Early Cretaceous volcano-sedimentary rocks tectonically overlie the Zacatecas Formation (Burckhardt, 1906; Martínez-Pérez, 1961; Centeno-Garcia and Silvia Romo, 1997). These rocks consist of a sequence of andesitic to basaltic lava flows and pillow

lavas metamorphosed to greenschist facies, interstratified with marine clastic and volcaniclastic rocks, limestone lenses, and thin layers of chert (Fig. 6b,c; Centeno-Garcia and Silvia Romo, 1997). The lava flows are green in colour, and vary in texture from aphanitic to porphyritic. Porphyritic textures consist of plagioclase phenocrysts (~3 mm) in a groundmass of plagioclase microlites and accessory ferromagnesian minerals including olivine, augite, rare biotite, and traces of opaque minerals. Zeolites filling amygdales are common (Fig. 7a–c). The dominant meta-sedimentary lithology of this succession is shale that ranges in colour from grey to black. The rock consists of well-compacted and homogeneous mud-sized particles commonly with very fine-grained framboidal pyrite (Fig. 7d–f).

Figure 7.

Stratigraphic, geochemical, and age correlations between these rocks and other Jurassic–Cretaceous successions elsewhere in the State of Zacatecas (e.g., Fresnillo, La Borda, El Saucito) have established that this unit was deposited in a back-arc tectonic setting and is part of the Guerrero terrane (De Cserna, 1976; Lapierre et al., 1992; Centeno-Garcia and Silva-Romo, 1997).

3.3 Eocene Sedimentary Rocks

The Eocene Zacatecas conglomerate unconformably overlies the Mesozoic rocks in the Zacatecas district (Edwards, 1955). It is a polymictic conglomerate containing ~60% pebbles of basaltic-andesitic lava, with the remainder comprised of phyllite, schist, slate, sandstone, limestone, felsic volcanic rocks, and granite, in a reddish sandy matrix (Fig. 6d). The fragments are subrounded to subanguar and range in size from 3 to 30 cm. Blocks up to 1.5 m across have been reported at the top of this unit (Caballero-Martinez, 1999; Escalona-Alcázar et al., 2016).

The Zacatecas conglomerate has been correlated with other red bed sequences that crop out elsewhere in central and southern Mexico (Edwards, 1955; Aranda-Gomez and McDowell, 1998; Aranda-Gomez et al., 2007; Tristan-Gonzalez et al., 2009; Escalona-Alcázar et al., 2016). Although not necessarily coeval, these conglomerates are interpreted to have been deposited under similar subaerial conditions, and as a result of the same sequence of geological events: uplift, extensional faulting, erosion, and volcanism after the end of the Laramide orogeny in

central Mexico (Edwards, 1955; Aranda-Gomez and McDowell, 1998; Aranda et al., 2007; Tristan-Gonzalez et al., 2009; Escalona-Alcázar et al., 2016).

3.4 Eocene Igneous Rocks

Eocene volcanism in the Zacatecas district is part of the voluminous igneous activity of the Sierra Madre Occidental silicic province (Aguirre-Diaz and Labarthe–Hernandez 2003). Rhyolitic ignimbrites, lava domes, plugs, and dikes unconformably overlie or intrude older rocks. Magmatism spanned a ~9 m.y. time period from 50.8 to 41.7 Ma (see below).

The oldest event is a complex of rhyolitic plugs and dikes spatially associated with the Mala Noche vein system, and includes the San Gil and La Sierpe plugs and dikes (which intrude the Jurassic–Cretaceous volcano-sedimentary sequence) and the El Magistral plug (which is emplaced along the contact between the Jurassic–Cretaceous volcano-sedimentary sequence and the Zacatecas Formation). The rhyolites are pale gray to whitish in color and vary in texture from aphanitic with flow banding and aligned xenoliths, to porphyritic at deeper levels (Fig.8a–b). The main phenocrysts are 1–7% of euhedral quartz and plagioclase (~1 mm in size) and minor euhedral biotite (1–3 mm in size) set in a devitrified matrix commonly with disseminations of very fine-grained pyrite (Fig. 8b and 9b). Quartz shows rounded and embayed textures indicating partial resorption during rise of the magma. Plagioclase shows moderate sericitic alteration and biotite is oxidized (Fig. 9b).

Both magmatic and hydrothermal breccias are observed in dikes. Magmatic breccias are located close to the contact with the volcano-sedimentary succession, are barren, and show globular peperitic texture (Busby-Spera and White, 1987) consisting of rounded and lobate clasts of grey to white porphyritic rhyolite in a matrix of black fine-grained metasediment (Fig. 8c). Hydrothermal breccias consist of sharply angular fragments of white rhyolite, cemented by chalcopyrite-pyrite bearing quartz (Fig. 8d).

Three samples, one taken from La Sierpe plug and two from dikes associated with Cu-rich mineralization yielded U-Pb zircon ages of 50.73 ± 0.37 Ma, and 50.19 ± 0.53 Ma, and 50.40 ± 0.45 Ma, respectively (see below).

Figure 8.

The La Bufa rhyolite dome is structurally controlled by the La Cantera fault/vein, which down-drops the Zacatecas conglomerate against the Jurassic-Cretaceous volcano-sedimentary sequence. The dome continues to the east as a narrow dike (too narrow to show on Fig. 5) emplaced along the fault, and is followed by the La Cantera vein (Perez-Martinez et al., 1961; Ponce and Clark, 1988). The La Bufa rhyolite is pale gray to pinkish in color, and contains ~5% phenocrysts of sanidine, quartz, orthoclase, and rare biotite (1–2 mm in size) in a partially devitrified glassy matrix. Feldspars are selectively argillized, biotite is replaced by hematite, and the matrix is partially devitrified (Fig. 9a). This alteration is considered to be deuteric, caused by volatiles released during late stages of solidification. A K-Ar whole rock date for this intrusion of 49.9 ± 1.0 Ma (Tristan-Gonzales, 2008) is similar to the U-Pb zircon age of 48.64 ± 0.50 Ma obtained in this study (see below).

The El Padre intrusion is an elongated rhyolitic plug associated with NNW-oriented dikes of the same composition. It crosscuts the Zacatecas conglomerate and the Jurassic-Cretaceous volcano-sedimentary sequence on the south side of the district (Fig.8). The rock is purple to reddish in color with vertical flow banding, and locally contains xenoliths. It contains ~5% phenocrysts of orthoclase, quartz, and fine-grained biotite (up to 3 mm in size) set in a partially devitrified matrix. Orthoclase phenocrysts show a dirty texture due to partial alteration to sericite, and biotite shows minor oxidation (Fig. 9c). The El Padre rhyolitic plug has been dated in this study at 45.32 ± 0.47 Ma (U-Pb on zircon; see below).

The La Virgen ignimbrite is a voluminous pyroclastic unit, ~200 m thick, which extends from the southern part of the El Orito vein system to the south for more than 5 km (Figs. 5 and 8fIts base in the northern portion is a volcanic breccia that consists of angular, poorly sorted rock fragments that range in size from 0.5 to 50 cm (Fig. 8g. The largest blocks are exposed in a thick (~25 m) outcrop that forms a prominent hill on the northeastern flank of the La Virgen ignimbrite, suggesting that the vent is located close to this area (Fig. 8f. This breccia grades to the south and southeast into a bedded (<1 m thick) medium- to fine-grained ash flow tuff with cross bedding that has been interpreted as a pyroclastic surge deposit (Tristan-Gonzalez, 2008). The base of this ignimbrite locally exhibits argillic (kaolinite) alteration. This alteration continues neither vertically nor laterally and is interpreted to be local weathering. The upper part of the ignimbrite is welded with rare lithic fragments. The texture is pyroclastic with broken

crystals of quartz, sanidine, eutaxitic pumice, and accessory biotite. The matrix is dominantly glassy with preserved glass shards and scarce isolated spherulites denoting minor devitrification (Figs. 9d). Concentrations of eutaxitic pumice and crystals form layers up to 20 cm thick (pseudostratification) within the welded ignimbrite that dip 10–15° SW are indicative of a SW flowing direction. Tristan-Gonzalez (2008) obtained a whole rock K-Ar age of 37.1 ± 0.9 Ma for this unit, but in this study we obtained an older U-Pb zircon age of 41.72 ± 0.45 (see below).

Figure 9.

3.5 Oligocene Rocks

In the southern half of the district, latitic and rhyolitic volcanic rocks and sinters have been mapped as Oligocene, although no radiogenic ages are available. The latite is a small unit exposed only in the southern portion of the area (Fig. 5), whereas rhyolitic rocks are voluminous and widespread to the south of Zacatecas (Fig. 5), and consist mainly of pyroclastic deposits. These include ash flow tuffs, lithic and lapilli breccias, and crystal-rich and vitric ignimbrites (Ponce et al., 1988).

The youngest bedded stratigraphic unit is an unaltered rhyolite crystal ash-flow tuff, the La Capilla tuff, which unconformably overlies the Eocene La Virgen ignimbrite (Fig. 5).

Sinter deposits also occur locally within the Oligocene rocks on the western flank of the La Virgen ignimbrite, and consist of stratiform siliceous ~N–S-elongated bodies ~750 m in length, 60 m wide, and up to 24 m thick (Fig. 5; Ponce et al., 1988). These deposits consist of subhorizontal bands (0.3–10 cm thick) of alternating light grey, white, and reddish amorphous silica (Fig. 10a), and contain abundant well-preserved circular and polygonal mud-crack structures, indicating formation at or near the paleosurface (Fig. 10b–c). The deposition of these sinters was possibly controlled by the same N–S-trending structural system that controlled the low-sulfidation El Orito veins, and might represent hot-spring activity concurrent with that hydrothermal system.

Figure 11.

3.6 Wall-rock alteration

Jurassic–Cretaceous volcano-sedimentary rocks are affected by greenschist-facies regional metamorphism, leading to the formation of chlorite, epidote, and minor calcite and disseminated pyrite. Additionally, there is local evidence within the Mala Noche area for contact metamorphic alteration that includes hornfels, marble, and skarn-type minerals, although no causative pluton has been identified to date. Hornfels consists of laminations of hardened grey to black shale and fine-grained quartzite, with chlorite–epidote-rich horizons locally replaced by sphalerite or pyrite (Fig. 11a–d). Marble is rare and has been observed only in drill hole CGS198 (projected sample location E745320, N2524692; depth 267.40–269.50 m) located ~500 m west of the San Gil rhyolite plug (Fig. 5). It is white, compact with a roughly equigranular texture, and is composed primarily of recrystallized calcite and dolomite (Fig. 11e–f). Skarn-type minerals occur locally in proximity to high copper grades in the Mala Noche mine (Fig. 12). Prograde alteration minerals include wolframite associated with magnetite and remnants of anhydrous silicate minerals (garnet and hedenbergite) that have been replaced by intense retrograde skarn-type alteration and late epithermal overprints. Retrograde minerals include abundant chlorite–epidote (dominantly clinochlore) and lesser amounts of ilvaite, Fe-hydroxides, nontronite, siderite, stilpnomelane, and laumontite among others (see section 3.8).

Eocene subvolcanic and volcanic felsic rocks are affected only by hydrothermal or deuteric alteration. The dominant alteration of rhyolitic plugs and dikes spatially associated with the Mala Noche vein system is phyllic (quartz, sericite-illite, and pyrite). The La buffa dome shows local slicification around vertical fractures due to vapour phase alteration, and development of argillic alteration associated to the Cantera fault on the northern edge of the dome. This alteration appears to be supergene because it does not extend to depth. The La Virgen ignimbrite shows dominantly deuteric alteration including partial devitrification of the matrix and vapor-phase silicification indicated by euhedral quartz crystals in vesicles (Fig. 9d.

Figure 12.

Figure 13.

3.7 Mineral Deposits

Mineral deposits in the Zacatecas district have been mined since 1548 for silver, gold, lead, zinc, and copper (Ponce et al., 1988). Copper has been mined as a main product only from the Mala Noche deposit. The bulk of the silver and base metal mineralization has been mined from epithermal veins in ESE- to SE-striking structures (Fig. 5). The main ore minerals are native silver, acanthite, silver sulfosalts, galena, sphalerite, chalcopyrite, and minor bornite, with ubiquitous pyrite, and locally pyrrhotite and magnetite in skarn assemblages. Gangue minerals include amethystine quartz (characteristic of the Veta Grande system but also present in the Mala Noche vein), colourless quartz, chalcedony, calcite, ankerite, and rare adularia. These types of vein in the Zacatecas area have been classified by Camprubi and Albinson (2007) as intermediate-sulfidation Ag-(Pb-Zn-Cu-Au), with the Veta Grande system being specifically described as containing both low- and intermediate-sulfidation styles.

The highest gold grades in the district occur in the El Orito vein system, which differs in orientation and mineralogy from the intermediate-sulfidation Ag-(Pb-Zn-Cu-Au) vein systems. The El Orito vein system is located in the southwestern part of the district and has a predominantly N–S trend (Fig. 5). This vein system has been described as the auriferous southern zone (Perez-Martinez et al., 1961), the Au-Ag-(Se) system (Ponce et al., 1988), or the El Orito system (Caballero-Martinez, 1999), and is classified as low-sulfidation Au-Ag by Camprubi and Albinson (2007).

The following sections provide descriptions of three of the most important mineral deposits in the district: the Mala Noche deposit, which is Cu-rich and includes skarn-type and epithermal mineralization in WNW-striking veins; the intermediate-sulfidation Veta Grande vein, which is representative of the polymetallic, Ag-rich, WNW- to NW-striking veins; and the low-sulfidation El Compas vein which is part of the Au-rich and predominantly N–S-trending El Orito system.

3.7.1 Mala Noche

The Mala Noche deposit, located in the central part of the Zacatecas district, is the only deposit where Cu has been mined as the main commodity, with Ag, Pb, and Zn as byproducts. Although the mineralization is dominantly in epithermal veins hosted by the Jurassic–Cretaceous

volcano-sedimentary sequence, Cu-rich zones show skarn characteristics and are spatially related to felsic plugs and dikes from the sub-volcanic complex.

Skarn-type mineralization. This mineralization style contains high grades of Cu (e.g., drillhole U-39 with 8% Cu over 4 m) and is characterized by replacement and/or semi-massive textures of chalcopyrite associated with pyrrhotite, magnetite, lesser sphalerite and galena, minor wolframite and/or relicts of silicate minerals (Figs. 12–14).

Figure 14

The silicate minerals are commonly altered to Fe-hydrosilicates and replaced by pyrrhotite, chalcopyrite, and pyrite (Figs. 12 and 13). Pyrrhotite is characteristic of this stage and occurs closely associated with ilvaite and replacing chalcopyrite (Fig. 13a). Chalcopyrite is the most abundant ore mineral and occurs in different mineral associations: intergrown with pyrrhotite and ilvaite (Fig. 13a); after bladed and acicular radial crystals (possibly amphibole) in association with magnetite, pyrite, and marcasite (Figs. 13b–d); replacing silicates including hedenbergite and isometrically shaped crystals (possibly garnet) altered to Fe-hydrosilicates (Figs. 13e–i); and replacing late-stage galena along cleavage planes (Fig. 13j). Chalcopyrite is commonly rimmed and replaced by pyrrhotite. Pyrite and marcasite are found replacing radial acicular and bladed tabular crystals (Fig. 13c–d). Sphalerite and galena are both late in the mineral paragenesis. Quartz, siderite, calcite, and ankerite are the main gangue minerals (Fig. 14). Quartz is typically fine-grained with a distinct grey color in hand sample.

The association of high Cu grades with replacement textures, remnants of calc-silicate minerals, and high temperature minerals such as wolframite, as well as the presence of marble distal to the Mala Noche Cu-rich mineralization indicates skarn-type mineralization. The calc-silicate mineral assemblage that defines a skarn (Meinert et al., 2005) is not clearly observed because it has been almost completely overprinted by retrograde alteration and later epithermal overprint. However, abundant tabular or acicular crystals with radial textures, and isometric minerals replaced by sulfides may represent precursor pyroxene, amphibole, and garnet, characteristic of skarn assemblages. Some samples of this stage of mineralization show evidence of post-mineral tectonic deformation including sheared massive sulfides with distorted galena

crystals and deformed triangular cleavage pits, sigmoidal shaped segregations of pyrite and chalcopyrite, cataclastic deformation textures in pyrite, and lineaments of quartz grains with undulose extinction. These textures suggest that strike-slip faulting disturbed this mineralization, further obscuring the spatial distribution and possible zoning of alteration minerals characteristic of skarns (Figs. 14 and 15; Meinert et al., 2005).

Figure 15.

Figure 16.

Epithermal mineralization. This mineralization is dominantly Zn-Pb-Ag-rich with low Cu grades and is characterized by open space textures (crustiform and cockade banding, breccias, and vuggy cavities; Fig. 16a–c). Sulfides form discontinuous bands associated with crustiform quartz, or infill interstitial spaces between gangue minerals. The first stages in the mineral paragenesis are sulfide-rich and lack amethystine quartz, whereas late stages are similar to the Veta Grande stage II with abundant amethystine quartz and chalcedony, and sparse sulfides (Figs. 16a and b, respectively). In the cockade texture, crustiform quartz coats pre-existing fragments of mineralization, and meta-sedimentary or volcanic rocks (Fig. 16c). The main ore mineral association is sphalerite, galena, pyrite, and minor chalcopyrite, with acanthite as blebs in sphalerite or galena, or associated with sphalerite in micro-veinlets of quartz (Fig. 16d–e). This mineralization does not show evidence of penetrative deformation and clearly overprints Cu-rich skarn-type mineralization (Figs. 16e–f). The main gangue minerals are clear coarse-grained euhedral quartz, amethystine quartz, calcite, and chalcedony.

Figure 17.

3.7.2 Veta Grande

The Veta Grande vein is the most prominent single vein (2 to 30 m wide including breccia and stockwork zones, ~7,000 m long) in a system that strikes northwest and dips ~70° to

the southwest. The Veta Grande vein has two main stages of mineralization with contrasting textures and gangue mineralogy (Figs. 17–19).

Figure 18.

Stage I consists of a breccia with fragments up to 4 cm long of volcanic and metasedimentary rocks, cemented by gray microcrystalline quartz, calcite, scarce adularia, and fine-grained sulfides (~5% pyrite-sphalerite-galena; Fig. 18a–d). The breccia shows some differences along the vein length: volcanic fragments and silica gangue are dominant to the southeast (Fig. 18a), whereas to the northwest, fragments of metasedimentary rocks are more abundant, and the gangue is dominated by carbonates (calcite, ankerite, dolomite, and scarce adularia; Fig. 18b–d). The sulfide mineralogy consists of variable percentages of pyrite, sphalerite, galena, with minor acanthite as inclusions in galena or pyrite, and minor chalcopyrite and pyrrhotite as blebs within sphalerite (Fig. 18e–f). Sphalerite shows growth zoning with iron contents ranging from 0.7–0.9 mole percent FeS (from electron microprobe analyses; Appendix A). Additionally, jamesonite and pyrargyrite associated with calcite are present in the northwest breccia.

The dominant alteration assemblage related to this mineralization stage is quartz-sericite and occurs as moderate to pervasive replacement of rock fragments within the breccia (Fig. 18a), and as haloes (<1 mm) around quartz veinlets within the wall rock. Carbonatization (calcite, ankerite, and dolomite) is also important in the northwest breccia (Fig. 18b). Propylitization consisting of chlorite, epidote, and disseminated pyrite is widespread in the volcano-sedimentary host rock, although it is not clear whether this alteration is related to hydrothermal processes or greenschist facies regional metamorphism. Based on the iron content in sphalerite, the abundance of base metal sulfides, the lack of high sulfidation-state minerals (e.g., enargite, digenite, and covellite), and the quartz-sericite vein wallrock alteration, this stage of mineralization can be classified as intermediate-sulfidation according to the criteria of Hedenquist et al. (2000).

Figure 19.

Stage II consists of rhythmically banded silica, with discontinuous bands containing minor sulfides, sulfosalts, and native silver. This second stage occurs as veins crosscutting the stage I breccia, and locally contains clasts of that breccia (Fig. 19a–b). The main silver minerals are acanthite and pyrargyrite (associated with galena and sphalerite). Gangue minerals include amethyst and clear crystalline quartz with crustiform, cockade, and vuggy textures, and chalcedony. Quartz pseudomorphs after bladed calcite (indicating boiling conditions) were also observed locally. The alteration in the host rock is mainly chlorite and hematite.

Replacement of pyrite by iron oxides, galena by anglesite, chalcopyrite by bornite and covellite, and native silver in late fractures and vugs show evidence of supergene replacement in this stage of mineralization (Fig. 19c–f). This stage was preferentially oxidized with respect to stage I due to the higher permeability of the vuggy veins, whereas the lack of permeability in the highly cemented matrix of stage I breccias largely precluded oxidation by downward percolation of groundwaters. Despite supergene oxidation, the general similarity of hypogene sulfide mineralogy between stages I and II suggests a common intermediate-sulfidation state.

Figure 20.

3.7.3 El Orito System

The El Compas vein is one of the principal veins in the El Orito System. The vein is gold-rich with minor silver, and lacks significant base metal sulfides. The vein consists of a single stage of mineralization, with multiple bands of alternating calcite and green to white fine-grained quartz intergrown with adularia in varying proportions (Fig. 20). The bands with higher proportions of adularia (~90%) are creamy in color and stain yellow with sodium cobaltinitrite (Fig. 21a). Textures such as bladed calcite replaced by quartz in late substages, and colloform, flamboyant, and plumose quartz are common (Figs. 21b–d; cf. Moncada et al., 2012). Ore minerals occur as black patches intergrown with bands of adularia and fine-grained quartz (Fig. 21e–f). Electron microprobe analyses show that gold occurs in the form of native gold and electrum (68 wt.% Au, 32 wt.% Ag; Appendix A), and silver occurs as electrum and in the selenide minerals aguilarite (Ag_4SeS) and naumannite (Ag_2Se). Pyrite is present only in trace amounts and is commonly replaced by supergene iron oxides. Gangue minerals are quartz,

chalcedony, adularia, and calcite. The alteration in the host rock consist mainly of silicification and minor illite. This type of mineralization is classified as low-sulfidation according to the scheme proposed by Hedenquist et al. (2000).

Figure 21.

Figure 22.

3.8 Structural Geology

Two main fault systems that host mineralized veins in the Zacatecas district have been mapped by Ponce et al. (1988), Caballero-Martinez (1999), and Tristán-González et al. (2012) (Figs. 5 and 22). The majority of the veins occur in the oldest system, which consists of ESE- to SE-striking faults that dip between 50° and 70° SW and NE, respectively. These faults have a maximum strike length of 16 km, and associated breccia widths of up to 20 m. This fault system is considered to have first formed in the Eocene because it crosscuts the Jurassic-Cretaceous volcano-sedimentary sequence and the La Sierpe and La Bufa domes, but does not affect the La Virgen ignimbrite (Fig. 5). Two different stages of activity have been identified based on kinematic indicators on the Veta Grande, Mala Noche, and La Cantera fault planes. Fault arrangements, horizontal slickenlines, and grooves on fault planes indicate that the first and principal stage of activity was dextral strike-slip, overprinted by a second stage of oblique sinistral and normal movement (Tristán-González et al., 2012). A breccia containing fragments of vein in the hanging-wall of the La Cantera fault/vein indicates that this normal fault reactivation occurred after the initial mineralizing event. Pyroclastic breccias at the base of the mid-Eocene La Virgen ignimbrite also contain vein fragments indicating that pyroclastic volcanism continued after mineralization, which is consistent with the dates obtained in this study.

Figure 23.

The younger of the two main fault systems, El Orito, strikes N–S with vertical to steep westerly dips (Fig. 23b). This system cuts both the Jurassic–Cretaceous volcano-sedimentary sequence and the La Virgen ignimbrite (Fig. 5). Veins filling this fault system show anastomosing arrangements where hosted by the Jurassic-Cretaceous volcano-sedimentary sequence. Here, individual veins range in thickness from 1 to 4 m, and multiple parallel vein sets occur over widths of up to 22 m in the El Compas mine, separated by ~2 m-wide panels of wall rock. Conversely, where the veins occur within the La Virgen Ignimbrite, they are typically planar, less than 1 m thick, and less mineralized relative to within the Jurassic-Cretaceous volcano-sedimentary sequence.

Kinematic indicators, structural data collected from the El Compas underground mine, and surface mapping of vein arrangements show that these veins formed in dominantly extensional normal faults with a sinistral component. Steeply dipping to vertical extensional faults and dilatational fault jogs with vertical principal stress direction and horizontal least principal stress direction are typical features in the El Compas vein. A sinistral strike-slip component is interpreted from NW-striking horsetail splays (Fig. 23; Nelson, 2005). The age of these faults and related veins is considered to be early Oligocene, based on an age obtained for adularia from a vein in this structural system (29.19 ± 0.20 Ma; see below).

4. Results

4.1 Whole-Rock Geochemistry

The results of whole-rock geochemical analyses are reported in Appendix C. Major-element compositions were recalculated to 100% on a volatile-free basis for plotting on geochemical classification diagrams (loss-on-ignition values range from 3.43–5.91 wt.% for Jurassic-Cretaceous rocks and 0.34 to 1.87 wt. % for Eocene rocks).

4.1.1 Jurassic–Cretaceous volcanic rocks

Jurassic–Cretaceous volcanic rocks show evidence for propylitic alteration and contain varying amounts of chlorite, epidote, calcite, and disseminated pyrite. This is reflected in high LOI values (3.4–5.9 wt. %). Despite this alteration and low grades of regional metamorphism

(greenschist facies), the samples plot in the basalt field in a TAS diagram (Fig. 24a). This is consistent with the immobile element (Zr/TiO2 vs Nb/Y) classification diagram of Winchester and Floyd (1977), where the samples fall within the range andesite/basalt (Fig. 24b).

Chondrite-normalized rare earth element (REE) patterns for the Jurassic–Cretaceous basalts are flat, at between 10 and 30 times chondritic values (Fig. 25a; normalization values of Sun and McDonough, 1989). These patterns are characteristic of back-arc basalts, which is the tectonic setting proposed for these rocks by various authors (Tardy et al., 1991; Yta, 1992; Lapierre et al., 1992; Centeno-Garcia and Silva-Romo, 1997). The samples show low primitive mantle-normalized abundances on an extended trace-element diagram (Fig. 25b) with flat patterns for Zr, Ti, and Y (~5 times primitive mantle values), small negative Nb-Ta and Th anomalies, and minor enrichments of the large ion lithophile elements (Cs, Rb, Ba, K, U, and Sr; between 10 and 100 times primitive mantle values).

Figure 24.

Figure 25.

4.1.2 Eocene Igneous Rocks

Samples of Eocene felsic volcanic rocks and domes plot in the rhyolite field on TAS and immobile trace-element diagrams (Fig. 24). The anomalously high silica content of sample ZAVI-04 (81.9 wt. % SiO_2) is likely due to deuteric silicification, as indicated by euhedral quartz crystals growing in vesicles within its partially devitrified matrix (Fig. 9d). All samples show high K (6.86–8.28 wt. % K_2O) and low Na contents (0.21–1.45 wt.% Na_2O), which are thought to broadly reflect their primary magmatic compositions, despite evidence for minor sericitic and argillic alteration of feldspars. A high-K calc-alkaline rhyolite composition is therefore proposed for these felsic volcanic rocks.

When plotted on a chondrite-normalized REE diagram (Fig. 25a) the suite shows strong enrichment of LREE with respect to heavy rare earth elements (HREE), and pronounced negative Eu anomalies that increase with SiO_2 content, indicating higher degrees of plagioclase fractionation from more evolved rhyolites. On a primitive mantle-normalized extended trace-element diagram (Fig. 25b) the suite shows strong enrichments in large ion lithophile elements,

and negative anomalies for Nb, Ta, and Ti, which are characteristic of subduction-related magmas (Gill, 1981; Brenan et al., 1994; Stolz et al., 1996). Strong negative anomalies for Sr and Eu suggest extensive fractionation of plagioclase (as noted above), and large negative anomalies for P and Ti are likely due to fractionation of apatite and Fe-Ti oxide minerals, respectively.

4.2 $^{40}Ar/^{39}Ar$ Geochronology

Apparent age spectra and inverse isochron plots are presented in Figure 26, and full analytical data are reported in Appendix D. Errors for ages are reported at the ±2σ level in the text and ±1σ in the plots.

Sample VG1B-S8 from an early-stage intermediate-sulfidation vein at Veta Grande produced a spectrum with high initial apparent ages that decrease to a plateau (steps 3–9: 94% of the ^{39}Ar released; Fig. 27a) with an age of 46.49 ± 0.44 Ma (slightly younger than the total gas age of 47.80 ± 0.42 Ma). Both plateau and total gas ages are considered to be anomalously old due to the presence of minor excess ^{40}Ar, as indicated by the high apparent ages of the initial steps, and the slightly upward-stepping "plateau" section. The inverse isochron age of 42.36 ± 0.18 Ma (MSWD = 0.76) provides a better estimate of the sample's true age because it accounts for the presence of excess ^{40}Ar, which is indicated by a slightly elevated initial $^{40}Ar/^{36}Ar$ ratio of 297.7 ± 1.2 (expected atmospheric ratio is 295.5). Low and uniform Ca/K ratios (see Appendix B) indicate outgassing of a pure, unaltered adularia mineral separate.

The apparent age spectrum for sample COM-L7 from the El Compas vein (El Orito system; Fig. 26b) shows a characteristic saddle shape indicating the presence of significant amounts of excess ^{40}Ar. The early steps show high apparent ages that decrease progressively until step 5, and from there apparent ages increase again. Steps 3 through 6 (53% of the ^{39}Ar released) define an approximate plateau with an age of 32.63 ± 0.40 Ma, but this age likely represents a maximum age for the sample due to excess ^{40}Ar. In contrast, a well-constrained inverse isochron (steps 1–11: 99.8% of the ^{39}Ar released) defines a distinctly younger age of 29.19 ± 0.20 Ma (MSWD = 1.8). The initial $^{40}Ar/^{36}Ar$ ratio of 302.5 ± 2.8 calculated from this isochron is significantly higher than the atmospheric value (295.5), and confirms the presence of excess ^{40}Ar. The inverse isochron age therefore provides the most reliable date for this sample.

The excess ^{40}Ar likely comes from fluid inclusions present in contaminant quartz that could not be separated from the fine-grained adularia. Fluid inclusions tend to decrepitate at relatively low temperatures, and can yield high apparent ages for early steps if some ^{40}Ar is present in the fluid at the time of trapping (Rama et al., 1965; Harrison and McDougall, 1980; Heizler and Harrison, 1988; Richards and McDougall, 1990). Uniform Ca/K ratios (see Appendix B) indicate outgassing of a homogeneous, unaltered, adularia mineral separate; therefore, these anomalies are not caused by other K- or Ca-bearing contaminant minerals.

Figure 26.

4.3 U/Pb Geochronology

Zircon U-Pb geochronological results are illustrated on Tera-Wasserburg Concordia plots in Figure 28, and the full analytical data are reported in Appendix E; errors are reported at the ±2σ level. The $^{207}Pb/^{206}Pb$ ratios are not corrected for common Pb, but the Concordia intercept is the common Pb-corrected age. A brief discussion of each result is provided below.

Thirty grains of zircon from sample ZABU-01 from the La Bufa rhyolite dome produced a weighted mean $^{238}U/^{206}Pb$ age of 48.54 ± 0.49 Ma (MSWD = 0.62), and a Tera-Wasserburg Concordia intercept age of 48.64 ± 0.50 Ma (MSWD = 0.59; Fig. 27a). Both results are very similar, but we adopt the Concordia intercept ages for all samples below.

Thirty-seven zircons from sample ZASI-02 from the La Sierpe rhyolite plug yielded a weighted mean $^{238}U/^{206}Pb$ age of 50.73 ± 0.37 Ma (MSDW = 1.03), and a Tera-Wasserburg Concordia intercept age of 50.81 ± 0.50 Ma (MSDW = 0.66; Fig. 27b).

Twenty-eight zircons from sample ZAPA-03 from the El Padre rhyolitic plug yielded two populations of zircons (Fig. 27c–e). Four grains gave a Tera-Wasserburg Concordia intercept age of 136 ± 13 Ma (MSWD = 4.4; Fig. 27d); this age is interpreted to record the age of andesitic xenoliths that are relatively abundant in this rhyolite. The other 24 grains yielded a Tera-Wasserburg Concordia intercept age of 45.32 ± 0.47 Ma (MSWD = 1.3; Fig. 27e), which is interpreted to represent the crystallization age of the El Padre plug.

Sample ZAVI-04 from the La Virgen ignimbrite yielded a weighted mean $^{238}U/^{206}Pb$ age for 25 grains of 42.04 ± 0.51 Ma (MSWD = 1.18), and a Tera-Wasserburg Concordia intercept age of 41.72 ± 0.45 Ma (MSWD = 1.08; Fig. 27f).

Sample 139-210 is from a felsic dike that runs parallel to a Cu-rich zone in the Mala Noche vein, and yielded a Tera-Wasserburg Concordia intercept age of 50.19 ± 0.53 Ma (MSDW = 1.4; Fig. 27g) with 23 out of 25 analyzed zircons. This age reflects the crystallization age of the sampled dike. The other two zircons are much older (~150–200 Ma) and were likely entrained as xenocrysts from the Jurassic–Cretaceous volcano-sedimentary country rocks.

Sample 139-288 is also from a felsic dike parallel to the Mala Noche vein, and has a similar age to samples S139-210 and ZASI-02. Twenty-five out of 28 analyzed zircons yielded a Tera-Wasserburg intercept age of 50.40 ± 0.45 Ma (MSDW = 1.1; Fig. 27h), whereas the other three zircons are inherited from Mesozoic basement rocks.

Figure 27.

5. Discussion

5.1 Geochemical comparison between the Zacatecas district and the southern Mesa Central magmatic rocks

The geochemical and radiogenic isotopic compositions of the Zacatecas Eocene volcanic rocks are compared to those of the upper and lower volcanic sequence rhyolites of the southern Mesa Central (from Orozco-Esquivel et al., 2002) in Figures 24, 25, and 28.

Most of the Zacatecas rhyolites show trace-element patterns more similar to rhyolites from the early Oligocene lower volcanic sequence than to the upper volcanic sequence of Orozco-Esquivel et al. (2002; Figs. 24 and 25). Both, the Zacatecas rhyolites and the lower volcanic sequence rocks have distinctive negative anomalies for Nb, Ta, and Ti that are characteristic of subduction-related magmas (Gill, 1981; Brenan et al., 1994; Stolz et al., 1996). However, the Zacatecas rhyolites are slightly more depleted in REE (especially middle-REE; MREE), Sr, P, Eu, and Ti than the lower volcanic sequence, reflecting their more fractionated (SiO_2-rich) compositions.

Figure 28.

In contrast, the Oligocene upper volcanic sequence rhyolites (Orozco-Esquivel et al., 2002) show flatter REE patterns with higher MREE and heavy-REE (HREE) abundances and large negative Eu anomalies, smaller depletions in Ta and Nb, and prominent depletions in Ba, Sr, and Eu relative to the lower sequence and Zacatecas rhyolites (Fig. 25; Orozco-Esquivel et al., 2002).

The similarity between the Zacatecas rhyolites and the regional lower volcanic rhyolite sequence, and the distinction from the upper volcanic sequence rhyolites, is also shown in the Th contents and Sr isotopic compositions of these rocks (Fig. 28; Sr isotopic data from Verma, 1984). The high Th contents and radiogenic Sr isotopic compositions of the upper sequence rocks indicates higher degrees of crustal interactions and contamination in these younger volcanic rocks (Verma, 1984; Christiansen et al., 1986; Orozco-Esquivel et al., 2002).

These contrasting geochemical and isotopic characteristics are interpreted to reflect a switch from subduction-related magmatism to magmas generated by partial melting of lower-crustal rocks during Oligocene Basin and Range-type extension. This transition took place over a short period of ~1 m.y. in the early Oligocene at ~30 Ma (Orozco-Esquivel et al., 2002; Rodriguez-Rios et al., 2007). The Eocene Zacatecas rhyolites are clearly related to the earlier phase of arc magmatism.

5.3 Timing, style, and tectonomagmatic setting of mineralization in the Zacatecas district

5.3.1 Eocene magmatism and Cu- and Zn-Pb-Ag-rich mineralization

Figure 29 summarizes the U-Pb and $^{40}Ar/^{39}Ar$ geochronology of igneous rocks and hydrothermal mineralization in the Zacatecas district.

Figure 29.

The U-Pb ages for felsic intrusive and volcanic rocks reported in this study constrain continental arc volcanism in the district to between ~50 to 41 Ma. The La Sierpe plug and dike

spatially associated with Cu-rich mineralization in the Mala Noche vein record the oldest Cenozoic magmatic event reported to date in the district. Their ages (50.81 ± 0.50 Ma, and 50.19 ± 0.53 Ma, respectively) are similar to that of the El Peñón Blanco granite located ~100 km SE of the Zacatecas district (50.94 ± 0.47 Ma; Aranda-Gomez et al., 2007). Both the granite stock and the rhyolitic hypabyssal rocks intrude marine sedimentary sequences deformed by Laramide shortening, but they show no field or petrographic evidence of deformation. This indicates that they were emplaced after the end of the main compressional phase of the Laramide orogeny. The similar ages of these rocks suggest that the La Sierpe rhyolitic plug and dikes may represent a local hypabyssal expression of deep, regional plutonism.

The Cu-rich mineralization in the Mala Noche vein was likely emplaced during late stages of crystallization of the La Sierpe plug and dikes (~50 Ma). This is suggested by local evidence of contact metamorphism associated with these rocks, and evidence of brecciation during or shortly after emplacement that includes hydraulic hydrothermal breccias, and peperitic magmatic breccias with amoeboid shaped fragments (indicating that the fragments were still hot at time of brecciation; Fig. 8c). This mineralization was sheared by ESE- to SE-trending strike-slip faults, which acted as pathways for later epithermal fluids. Deformation textures in sulfides have been reported also in the San Martin skarn deposit (Rubin and Kyle, 1988), which is located along a SE regional trend of deposits that contain both skarn-type and epithermal mineralization including San Martin, La Colorada, Francisco I. Madero, Zacatecas, and Guanajuato (Fig. 2; Rubin and Kyle, 1988; Randall et al., 1994; Moller et al., 2001; Cannet et al., 2009).

In the Zacatecas district, magma was extruded along ESE- to SE-trending strike-slip faults after the emplacement of the La Sierpe plug and dikes. The La Bufa dome was emplaced at 48.64 ± 0.50 Ma along the ESE-trending La Cantera fault system, which is roughly parallel and relatively close to the suture zone of the oceanic Guerrero terrane with the North American continent (Figs. 2 and 5). The fact that felsic calc-alkaline magma was emplaced along a normal fault, synchronous with sedimentary basin formation (deposition of the Zacatecas red conglomerate), indicates that the volcanic arc was under a mild extensional or transtensional stress regime at this time (Tristan-Gonzalez et al., 2009; 2012). The La Virgen ignimbrite (41.72 ± 0.45 Ma) overlies the Zacatecas red conglomerate and represents the youngest volcanic event recorded in the district.

Because the La Sierpe plug and La Bufa dome are both cut by intermediate-sulfidation polymetallic epithermal veins, they provide a maximum age for hydrothermal activity (≤48.7 Ma). Similarly, the La Virgen ignimbrite is not cut by the ESE- to SE-striking Ag-Pb-Zn veins, and therefore provides a minimum age for this mineralization stage (≥41.7 Ma).

A direct age for the Ag-rich mineralizing event is provided by a $^{40}Ar/^{39}Ar$ age for adularia from stage I of the Veta Grande intermediate-sulfidation vein (42.36 ± 0.18 Ma), consistent with the constraints noted above. This mid-Eocene age suggests that the mineralizing event occurred towards the end of the volcanic cycle, shortly prior to emplacement of the La Virgen ignimbrite. This, together with the fact that dikes share the same structures as veins, suggests an intimate relationship between intermediate-sulfidation mineralization and the last stages of subduction-related magmatism in the area, consistent with the model proposed by Sillitoe and Hedenquist (2003). Silver-rich mineralization in other districts within the Mesa Central has also been linked to subduction-related magmatism between 55–32 Ma (e.g., at the Guanajuato, Sombrerete, La Colorada, and Fresnillo-Fortuna area deposits; Albinson, 1988; Lang et al., 1988; Randall et al., 1994).

The age of the stage II intermediate-sulfidation mineralization in the Veta Grande vein has not been constrained, but we consider that the two stages were essentially coeval because they share the same structures and structural orientation.

5.3.2 Oligocene Au mineralization

Unlike the earlier Eocene Ag-Pb-Zn mineralization, the low-sulfidation El Orito vein system is not clearly related to magmatism, and occurs in a structurally distinct set of N–S-trending veins. It thus appears to have no temporal or genetic relationship to the intermediate-sulfidation Ag-Pb-Zn veins, contrary to the proposal of Camprubi and Albinson (2007). The El Orito vein system cuts the La Virgen ignimbrite (42.36 ± 0.18 Ma), and our 29.19 ± 0.20 Ma $^{40}Ar/^{39}Ar$ age for adularia from the El Compas vein confirms that the low-sulfidation Au mineralization was formed during a distinct younger event in the late Oligocene.

This mineralization was emplaced in dominantly normal faults with a sinistral strike-slip component. Previous studies have used different interpretations to explain the structural contrast between this and the ESE- to SE-striking system. Nelson (2005) suggested that both systems

were formed as a result of the same stress field (Fig. 30a), whereby the El Orito faults would represent second-order antithetic structures (R') with a sense of displacement opposite to the bulk movement, and oriented at a high angle (~75°) to the main dextral strike-slip fault plane (La Centera vein; M).

Figure 30.

In contrast, other authors (Tristan-Gonzalez et al., 2009; 2012) have suggested that the NNW-striking El Orito faults might have been formed after the Zacatecas fault system, and in response to a change from a transtensional stress regime in the Eocene to dominantly extensional in the Oligocene related to Basin and Range deformation, with a local sinistral strike-slip component (Fig. 30b). This model implies a rotation of the regional extension direction from NNE in the Eocene to ENE in the Oligocene (Fig. 30c), which is consistent with the ages obtained in this study, and with regional structural interpretations (Tristan-Gonzalez et al., 2009; 2012); we therefore favor this model.

The occurrence of selenide minerals in the El Orito system suggests a similarity to the selenide-rich suite of Au-Ag low-sulfidation deposits in the northern Nevada rift (John, 2001). These deposits include Midas, Sleeper, and Mule Canyon, and have been related to the Yellowstone hotspot and Basin and Range extensional tectonics. A detailed $^{40}Ar/^{39}Ar$ study from Midas shows that Au-Ag mineralization was coeval with felsic volcanism and NNW–NW-striking normal faults at 15.4 ± 0.10 Ma ($^{40}Ar/^{39}Ar$ on adularia; Leavitt et al., 2004), although isotopic and other data suggest a source of gold from mantle-derived magmas (Kameov et al., 2007; Saunders and Brueseke, 2012; Saunders et al., 2016). The low-sulfidation El Orito system is not clearly related to magmatism in the Zacatecas area and is older than the Nevada deposits, but its age coincides with the time of change in magma composition across the Mesa Central in response to the onset of Basin and Range tectonics (Orozco-Esquivel et al., 2002; Rodriguez-Rios et al., 2007). The regional effusion of felsic magma (upper volcanic sequence) related to this event was controlled by graben and half-graben structures with similar N–S orientations to the El Orito vein system and other Au-Ag-rich low-sulfidation deposits in the Mesa Central (e.g., Bolañitos in Guanajuato, and Pinos in Zacatecas; Figs. 4 and 5; Labarthe-Hernandez et al., 1982; Tristan-Gonzalez et al., 2009; Steel, 2012; Munroe, 2014). Sinter deposits, characteristic of low-

sulfidation mineralization (Sillitoe and Hedenquist, 2003), were deposited in the Oligocene and proximal to N–S graben-bounding normal faults. Thus, we suggest that Oligocene low-sulfidation mineralization in the Zacatecas district was related to the onset of this extensional tectonic regime.

The similar age of Au-Ag-rich mineralization in the Fresnillo SW district (29.75 ± 0.12 and 29.68 ± 0.10 Ma; Velador, 2010; Velador et al., 2010) to the El Orito system (29.19 ± 0.20 Ma), and the similar mineralogy to the Au-rich low-sulfidation mineralization of the Guanajuato district (30–27 Ma; Gross 1975), which is controlled by similar structural systems, suggests that these low-sulfidation hydrothermal systems were related to the onset of Basin and Range extensional tectonics across the Mesa Central in the Oligocene. These observations are consistent with the model proposed by Sillitoe and Hedenquist (2003) for low-sulfidation deposits.

6. Conclusions

Polymetallic mineral deposits in central Mexico commonly show combined characteristics of different styles of mineralization including skarn-type, intermediate- and low-sulfidation (e.g., The San Martin, Zacatecas, Fresnillo, and Guanajuato mining districts). Most researchers have attributed this combination of mineralization styles to the evolution of protracted hydrothermal systems related to the emplacement of plutons that have not been identified. However, this study indicates that these different styles of mineralization are related to distinct tectonic events, which are summarized in Figure 31.

The Guerrero terrane accretion to the continent in the Late Cretaceous produced deep-seated structurally week planes that may have served as channels for Eocene magma ascent and the flow of hydrothermal fluids (Fig. 31a). In the Zacatecas district at ~51 Ma, felsic magma and hydrothermal fluids were channelled along NW-trending structures forming localized high-grade Cu skarn mineralization and related veins (Fig. 31b). Strike-slip reactivation of these structures sheared the mineralization and allowed the emplacement of a subsequent set of Ag-Pb-Zn-rich epithermal intermediate-sulfidation veins at ~42 Ma, apparently associated with the last stages of subduction-related magmatism in the Mesa Central (Fig. 31c–d). During the onset of Basin and Range crustal extensional deformation in the Mesa Central at ~29 Ma, these deposits were overprinted by Au-rich epithermal low-sulfidation veins along N–S-oriented structures (Fig.

31e). This model explains the juxtaposition of skarn-type, intermediate- and low-sulfidation deposits in the Mesa Central, deposit types that are normally found in different tectonic settings and therefore, different locations (Hedenquist et al., 2000; Sillitoe and Hedenquist, 2003). Similarly, the metallic distribution in northwestern Mexico has been attributed to the superimposition of different tectonomagmatic events over a period of ~150 m.y. (Staude and Barton 2001).

The distribution of world class mining districts that include combined styles of mineralization aligned along the Guerrero Terrane boundary, suggests that the richness of the Mexican Silver Belt can be explained in terms of the tectonic history of Mexico.

Figure 31.

Acknowledgments

The authors would like to thank North Country Gold, now a wholly-owned subsidiary of Auryn Resources Inc., for financing this research project. The Society of Economic Geologist Canada Foundation also provided partial financial support for fieldwork through a student research grant. Thanks to Consejo Nacional de Ciencia y Tecnologia for the scholarship No. 305391 granted to Osbaldo Zamora Vega. We would like to thank Capstone Gold, Oro Silver Resources, and Mr. Jose Parga for access to drillcore and underground sampling. Mineral separation was done with the help of Mark Labbe at the University of Alberta facilities.

References

Aguirre-Diaz GJ, McDowell FW (1991) The volcanic section at Nazas, Durango, Mexico, and the possibility of widespread Eocene volcanism within the Sierra Madre Occidental; Mid–Tertiary Cordilleran magmatism; plate convergence versus intraplate processes. Journal of Geophysical Research 96:13373–13388

Aguirre-Diaz GJ, McDowell FW (1993) Nature and timing of faulting and synextensional magmatism in the southern Basin and Range, central–eastern Durango, Mexico. Geological Society of America Bulletin 105:1435–1444

Aguirre-Diaz GJ, Labarthe-Hernandez G (2003) Fissure ignimbrites; fissure–source origin for voluminous ignimbrites of the Sierra Madre Occidental and its relationship with basin and range faulting. Geology (Boulder) 31:773–776

Albinson T (1988) Geologic reconstruction of paleosurfaces in the Sombrerete, Colorada, and Fresnillo districts, Zacatecas state, Mexico. Economic Geology 83:1647–1667

Albinson T (1995) Bosquejo de la evolución estructural e hidrotermal del distrito de Zacatecas, *in* Trabajos Técnicos XXI Convención Nacional Asociación de Ingenieros de Minas, Metalurgistas y Geólogos de México, Acapulco, Guerrero: México D.F., Asociación de Ingenieros de Minas, Metalurgistas y Geólogos de México (AIMMGM), p. 143–170.

Albinson T, Norman DI, Cole D, Chomiak B (2001) Controls on formation of low–sulfidation epithermal deposits in Mexico; constraints from fluid inclusion and stable isotope data; New mines and discoveries in Mexico and Central America. Special Publication (Society of Economic Geologists (U.S.)) 8:1–32

Amador MG (1908) Las capas Carnicas de Zacatecas Triassic deposits. Boletin de la Sociedad Geologica Mexicana 29–35

Aranda-Gomez JJ, McDowell FW (1998) Paleogene extension in the southern Basin and Range Province of Mexico; syndepositional tilting of Eocene red beds and Oligocene volcanic rocks in the Guanajuato mining district. International Geology Review 40:116–134

Aranda-Gomez JJ, Henry CD, Luhr JF (2000) Post–Paleocene tectono–magmatic evolution of the Sierra Madre Occidental and the southern part of the Basin and Range tectonic province, Mexico. Boletin de la Sociedad Geologica Mexicana 53:59–71

Aranda-Gomez JJ, Molina-Garza R, McDowell FW, Vassallo Morales LF, Ortega-Rivera MA, Solorio-Munguia JG, Aguillon-Robles A (2007) The relationships between volcanism and

extension in the Mesa Central; the case of Pinos, Zacatecas, Mexico. Revista Mexicana de Ciencias Geologicas 24:216–233

Atwater TM (1989) Plate tectonic history of the northeast Pacific and Western North America. In Winterer EL (ed) The Geology of North America, The northeastern Pacific Ocean and Hawaii 21–72

Barboza-Gudiño JR, Tristan-Gonzalez M, Torres-Hernandez JR, (1998) The Late Triassic–Early Jurassic active continental margin of western North America in northeastern Mexico. Geofisica Internacional 37:283–292

Barton, PB, Jr., (1985) High Temperature Calculations Applied to Ore Deposits in: Fluid–Mineral Equilibria in Hydrothermal Systems: Reviews in Economic Geology, v1.

Brenan JM, Shaw HF, Phinney DL, Ryerson FJ, (1994) Rutile–aqueous fluid partitioning of Nb, Ta, Hf, Zr, U and Th: implications for high field strength element depletions in island–arc basalts. Earth and Planetary Science Letters 128:327–339

Burckhardt C (1906) Sobre el descubrimiento del Triasico marino en Zacatecas. Boletin de la Sociedad Geologica Mexicana 43–45

Busby-Spera CJ, White JDL, (1987) Variation in peperite textures associated with differing host-sediment properties. Bulletin of Volcanology 49 (6): 765–776

Caballero-Martinez JA (1999) Carta Geologico–Minera, Zacatecas F13–B58. Servicio Geologico Mexicano–Secretaria de Economia 1:50,000 scale

Camprubi A (2009) Major metallogenic provinces and epochs of Mexico. Society for Geology Applied to Mineral Deposits News 25:6–20

Camprubi A, Ferrari L, Cosca MA, Cardellach E, Canals A (2003) Ages of epithermal deposits in Mexico; regional significance and links with the evolution of Tertiary volcanism. Economic Geology and the Bulletin of the Society of Economic Geologists 98:1029–1037

Camprubi A, Albinson T (2007) Epithermal deposits in Mexico; update of current knowledge, and an empirical reclassification; Geology of Mexico; celebrating the centenary of the Geological Society of Mexico. Special Paper – Geological Society of America 422:377–415

Cannet C, Camprubi A, Gonzalez-Partida E, Linares C, Alfonso P, Piñeiro-Fernandez F, Prol-Ledesma RM (2009) Mineral assemblages of the Francisco I. Madero Zn-Cu-Pb-(Ag) deposit, Zacatecas, Mexico: Implications for ore deposit genesis. Ore Geology Reviews 35:423–435

Centeno-Garcia E (2005) Review of upper Paleozoic and lower Mesozoic stratigraphy and depositional environments of central and west Mexico; constraints on terrane analysis and paleogeography; The Mojave–Sonora Megashear hypothesis; development, assessment, and alternatives. Special Paper – Geological Society of America 393:233–258

Centeno-Garcia E, Ruiz J, Coney PJ, Patchett PJ, Ortega–Gutierrez F (1993) Guerrero Terrane of Mexico; its role in the Southern Cordillera from new geochemical data: Geology (Boulder) 21:419–422

Centeno-Garcia E, Silva-Romo G (1997) Petrogenesis and tectonic evolution of central Mexico during Triassic–Jurassic time; Special issue dedicated to the International workshop on The geology of northwestern Sonora. Revista Mexicana de Ciencias Geologicas 14:244–260

Centeno-Garcia E, Guerrero-Suastegui M, Talavera-Mendoza O (2008) The Guerrero composite terrane of western Mexico; collision and subsequent rifting in a supra–subduction zone; Formation and applications of the sedimentary record in arc collision zones. Special Paper – Geological Society of America 436:279–308

Centeno-Garcia E, Busby C, Busby M, Gehrels GE (2011) Evolution of the Guerrero composite terrane along the Mexican margin, from extensional fringing arc to contractional continental arc. Geological Society of America Bulletin 123:1776–1797

Christiansen EH, Sheridan MF, Burt DM (1986) The geology and geochemistry of Cenozoic topaz rhyolites from the Western United States. Special Paper – Geological Society of America 205:01–82

Clark KF, Foster CT, Damon PE (1982) Cenozoic mineral deposits and subduction–related magmatic arcs in Mexico; Symposium on subduction of oceanic plates. Geological Society of America Bulletin 93:533–544

Clark KF, Fitch DC (2009) Evolucion de depositos metalicos en tiempo y espacio en Mexico. In: Clark KF, Salas–Pizá G, Cubillas–Estrada R (ed) Geología Económica de México, II Edición. Servicio Geológico Mexicano 43

Coney PJ, Reynolds SJ, (1977) Cordilleran Benioff zones. Nature (London) 270:403–406

Damon PE, Shafiqullah M, Clark KF (1981) Age trends of igneous activity in relation to metallogenesis in the southern Cordillera; Relations of tectonics to ore deposits in the southern Cordillera. Arizona Geological Society Digest 14:137–154

De Cserna Z (1976) Geology of the Fresnillo area, Zacatecas, Mexico. Geological Society of America Bulletin 87:1191–1199

De Cserna Z (1981) Active continental margin collision in the southwestern part of the Gulf of Mexico. Revista – Instituto de Geologia 5:255–261

Dickinson WR, Snyder WS (1978) Plate tectonics of the Laramide Orogeny. In: Matthews V (ed) Lara– mide folding associated with basement block faulting in the western United States. Geological Society of America Memoir 151:355–366

Dickinson WR (2006) Geotectonic evolution of the Great Basin. Geosphere 2:353–368

Edwards JD (1955) Studies of some early Tertiary red conglomerates of central Mexico. 0264–H:01–153

Einaudi MT, Hedenquist JW, Inan EE (2003) Sulfidation state of fluids in active and extinct hydrothermal systems; transitions from porphyry to epithermal environments; Volcanic, geothermal, and ore–forming fluids; rulers and witnesses of processes within the Earth. Special Publication (Society of Economic Geologists (U.S.)) 10:285–313

Escalona-Alcázar FJ, Solari L, Garcia JC, Carrillo-Castillo C, Bluhm-Gutierrez J, Garcia-Sandoval P, Nieto-Samaniego A, Nunez-Pena P (2016) The Palaeocene-early Oligocene

Zacatecas conglomerate, Mexico: sedimentology, detrital zircon U–Pb ages, and sandstone provenance. International Geology Review V. 58 No. 7: 826–848.

Ferrari L, Lopez-Martinez M, Rosas-Elguera J (2002) Ignimbrite flare up and deformation in the southern Sierra Madre Occidental, western Mexico: implications for the late subduction history of the Farallon plate. Tectonics 21:1–24

Ferrari L, Valencia-Moreno M, Bryan S (2007) Magmatism and tectonics of the Sierra Madre Occidental and its relation with the evolution of the western margin of North America; Geology of Mexico; celebrating the centenary of the Geological Society of Mexico. Special Paper – Geological Society of America 422:1–39

Gill JB (1981) Orogenic Andesites and Plate Tectonics. Minerals and Rocks, Springer-Verlag 16:1–390

Goldstein RH and Reynolds TJ (1994) Systematics of fluid inclusions in diagenetic minerals: Society of Economic Paleontologists and Mineralogists, Short Course Handbook, v. 31, 199 p.

Götze J, Plötze M, and Habermann D (2001) Origin, spectral characteristics and practical applica- tions of the cathodoluminescence of quartz— A review: Mineralogy and Petrology, v. 71, p. 225–250.

Gross WH (1975) New ore discovery and source of silver-gold veins, Guanajuato, Mexico. Economic Geology 70:1175–1189

Günther D, Aude´tat A, Frischknecht R, and Heinrich CA (1998) Quantitative analysis of major, minor and trace elements in fluid inclusions using laser ablation inductively coupled plasma mass spectrometry. *J. Anal. At. Spectrom.* 13(4), 263–270

Harrison TM, McDougall I (1980) Investigations of an intrusive contact, Northwest Nelson, New Zealand; II, Diffusion of radiogenic and excess ^{40}Ar in hornblende revealed by $^{40}Ar/^{39}Ar$ age spectrum analysis. Geochimica et Cosmochimica Acta 44:2005–2020

Hedenquist JW, Arribas RA, Gonzalez-Urien E (2000) Exploration for epithermal gold deposits; Gold in 2000. Reviews in Economic Geology 13:245–277

Heizler MT, Harrison TM (1988) Multiple trapped argon isotope components revealed by $^{40}Ar/^{39}Ar$ isochron analysis. Geochimica et Cosmochimica Acta 52:1295–1303

Heinrich CA, Pettke T, Halter W, Aigner M, Aude´tat A, Günther D, Hattendorf B, Bleiner D, Guillong M, Horn I (2003) Quantitative multi-element analysis of minerals, fluids, and melt inclusions by Laser Ablation Inductively-Coupled-Plasma Mass-Spectrometry. Geochim. Cosmochim. Acta. 67, 3473–3497.

Henry CD, Price JG, James EW (1991) Mid–Cenozoic stress evolution and magmatism in the southern Cordillera, Texas and Mexico; transition from continental arc to intraplate extension. Journal of Geophysical Research 96:545–560

Henry CD, Aranda-Gomez JJ (1992) The real southern Basin and Range; mid– to late Cenozoic extension in Mexico: Geology (Boulder) 20:701–704

Henry CD, Aranda-Gomez JJ, (2000) Plate interactions control middle–late Miocene, proto–Gulf and Basin and Range extension in the southern Basin and Range; The influence of plate interaction on post–Laramide magmatism and tectonics in Mexico. Tectonophysics 318:1–26

Humphreys E, Hessler E, Dueker K, Farmer GL, Erslev E, Atwater T (2003) How Laramide–age hydration of North American lithosphere by the Farallon Slab controlled subsequent activity in the Western United States. International Geology Review 45:575–595

Irvine TN, Baragar WRA (1971) A guide to the chemical classification of the common volcanic rocks. Canadian Journal of Earth Sciences = Revue Canadienne des Sciences de la Terre 8:523–548

John DA (2001) Miocene and early Pliocene epithermal gold–silver deposits in the northern Great Basin, Western United States; characteristics, distribution, and relationship to magmatism. Economic Geology and the Bulletin of the Society of Economic Geologists 96:1827–1853

Jones NW, McKee JW, Anderson TH, Silver LT (1995) Jurassic volcanic rocks in northeastern Mexico; a possible remnant of a Cordilleran magmatic arc; Studies on the Mesozoic of Sonora and adjacent areas. Special Paper – Geological Society of America 301:179–190.

Kamenov GD, Saunders JA, Hames WE, Unger DL. Mafic magmas as sources for gold in middle Miocene epithermal deposits of the Northern Great Basin, United States: Evidence from Pb isotope compositions of native gold. Econ. Geol. 2007, 102, 1191–1195

Kapusta,Y (2006) K/Ar age dating of whole rocks from El Compas samples, Zacatecas District, Mexico: Geochronology and Isotopic Geotchemistry: Ancaster, Activation Labs, Private Report for Minera Hochschild Mexico, S.A. de C.V., 2 p.

Keppie, J.D., Dostal, J., Cameron, K.L., Solari, L.A., Ortega-Gutiérrez, F., and Lopez, R., 2003, Geochronology and geochemistry of Grenvillian igneous suites in the northern Oaxacan Complex, southern Mexico: Tectonic implications: Precambrian Research, v. 120, p. 365–389.

Labarthe-Hernandez G, Tristan-Gonzalez M, Aranda-Gomez J, (1982) Revision estratigrafica del Cenozoico de la parte central del Edo de San Luis Potosi. Instituto de Geologia, Universidad Autonoma de San Luis Potosi 85:1–208

Lang B, Steintz G, Sawkins FJ, Simmons SF (1988) K/Ar age studies in the Fresnillo silver district, Zacatecas, Mexico. Economic Geology 83:1642–1646

Lapierre H, Tardy M, Coulon C, Ortiz-Hernandez E, Bourdier JL, Martinez-Reyes J, Freydier C (1992) Caracterisation, genese et evolution geodynamique du terrain de Guerrero; Mexique occidental. Characterization, genesis, and geodynamic evolution of the Guerrero Terrane, western Mexico. Canadian Journal of Earth Sciences = Revue Canadienne des Sciences de la Terre 29:2478–2489

Leavitt ED, Spell TL, Goldstrand PM, Arehart PM (2004) Geochronology of the Midas low-sulfidation epithermal gold-silver deposit Elko County, Nevada. Economic Geology 99:1665–1686

Le Bas MJ, Le Maitre RW, Streckeisen A, Zanettin BA (1986) Chemical classification of volcanic rocks based on the total alkali–silica diagram. Journal of Petrology 27:745–750.

Maldonado-Koerdell M (1948) Nuevos datos geologicos y paleontologicos sobre el Triasico de Zacatecas Mexico. Anales Esc.Nac.Cien.Biol 5:291–306

Mapes VE (1949) Los Criaderos Minerales de "El Bote,"Zacatecas, Zacatecas, Mexico. Instituto Nacional de Investigacion en Recursos Minerales 24:1–39

McDowell FW, and Keizer RP, (1977) Timing of mid-Tertiary volcanism in the Sierra Madre Occidental between Durango City and Mazatlán, Mexico: Geological Society of America Bulletin, v. 88, p. 1479–1487

Meinert LD, Dipple GM, and Nicolescu S (2005) World skarn deposits: ECONOMIC GEOLOGY 100TH ANNIVERSARY VOLUME, p. 299−336.

Moller, SA, Islas JE, and Davila RT (2001) New discoveries in the La Colorada district, Zacatecas State, Mexico: Society of Economic Geologists Special Publication Series, v. 8, p. 95–104.

Moncada D, Mutchler S, Nieto A, Reynolds TJ, Rimstidt JD, Bodnar RJ (2012) Mineral textures and fluid inclusion petrography of the epithermal Ag–Au deposits at Guanajuato, Mexico: application to exploration. Jour Geochem Explor 114:20–35

Mortensen JK, Hall BV, Bissig T, Friedman RM, Danielson T, Oliver J, Rhys DA, Ross KV, Gabites JE (2008) Age and paleotectonic setting of volcanogenic massive sulfide deposits in the Guerrero terrane of central Mexico: Constraints from U–Pb age and Pb isotope studies. Economic Geology and the Bulletin of the Society of Economic Geologists 103:117–140

Mújica-Mondragón R, Jacobo-Albarrán J, (1983) Estudio petrogenético de las rocas ígneas y metamórficas del Altiplano Mexicano, México: Instituto Mexicano del Petróleo, Proyecto C-1156, 78 p.

Munroe MJ (2014) Technical Report on the Resource and reserve estimates for the Bolañitos mines project, Guanajuato state, Mexico. NI 43-101 technical report prepared for Endeavour Silver Corp., effective date December 31, 2013.

Nelson, E P (2005) Structural Analysis of the El Orito District, Zacatecas, Mexico. Technical report for Minera Hochschild Mexico S.A. de C. V. September 13, 2005. 16p.

Nieto-Samaniego AF, Alaniz-Alvarez SA, Labarthe-Hernandez G (1997) The post–Laramide Cenozoic deformation in the southern Mesa Central, Mexico. Revista Mexicana de Ciencias Geologicas 14:13–25

Nieto-Samaniego AF, Alaniz-Alvarez SA, Camprubi, A (2005) La Mesa Central de México: estratigrafía, estructura y evolución tectónica cenozoica. Boletín de la Sociedad Geológica Mexicana. Tomo LVII 3:285–318

Nieto-Samaniego AF, Alaniz-Alvarez SA, Camprubi A (2007) Mesa Central of Mexico; stratigraphy, structure, and Cenozoic tectonic evolution; Geology of Mexico; celebrating the centenary of the Geological Society of Mexico. Special Paper – Geological Society of America 422:41–70

Orozco-Esquivel MT, Nieto-Samaniego AF, Alaniz-Alvarez SA (2002) Origin of rhyolitic lavas in the Mesa Central, Mexico, by crustal melting related to extension; Volcanism and associated regimes; the complexity of volcanic systems. Journal of Volcanology and Geothermal Research 118:37–56

Ortega-Gutiérrez F, Ruiz J, Centeno-Garcia E (1995) Oaxaquia, a Proterozoic microcontinent accreted to North America during the late Paleozoic. Geology (Boulder) 23:1127–1130

Pearce, J. A., and J. R. Cann (1973) Tectonic setting of basic volcanic rocks determined using trace element analyses, Earth Planet. Sci. Lett., 19, 290–300

Peccerillo A, Taylor SR (1976) Geochemistry of Eocene calc–alkaline volcanic rocks from the Kastamonu area, northern Turkey. Contributions to Mineralogy and Petrology 58:63–81

Perez-Martinez JJ, Mapes-Vazquez E, Pesquera-Velazquez R (1961) Bosquejo geologico del distrito minero de Zacatecas. Boletin – Consejo de Recursos Naturales no Renovables 1–38

Ponce S BF, Clark KF, Salas P (1988) The Zacatecas mining district; a Tertiary caldera complex associated with precious and base metal mineralization; A special issue devoted to the

geology and mineral deposits of Mexico. Economic Geology and the Bulletin of the Society of Economic Geologists 83:1668–1682

Rama SNI, Hart SR, Roedder E (1965) Excess radiogenic argon in fluid inclusions. Journal of Geophysical Research 70:509–511

Randall JA, Saldaña E, Clark KF (1994) Exploration in a volcano-plutonic center at Guanajuato, Mexico. Economic Geology 89:1722–1751

Ranson WA, Fernandez LA, Simmons WB (1975) Geology and petrology of the Zacatecas mining district, Zacatecas, Mexico. Abstracts with Programs – Geological Society of America 7:228

Ranson WA, Fernandez LA, Simmons WBJr, de la Vega SE (1982) Petrology of the metamorphic rocks of Zacatecas, Zac., Mexico. Boletin de la Sociedad Geologica Mexicana 43:37–59

Richards JP, McDougall I (1990) Geochronology of the Porgera gold deposit, Papua New Guinea; resolving the effects of excess argon on K–Ar and $^{40}Ar/^{39}Ar$ age estimates for magmatism and mineralization. Geochimica et Cosmochimica Acta 54:1397–1415

Richards JP, Noble SR (1998) Application of radiogenic isotope systems to the timing and origin of hydrothermal processes; Techniques in hydrothermal ore deposits geology. Reviews in Economic Geology 10:195–233

Rodriguez-Rios R, Aguillon-Robles A, Leroy JL (2007) Evolucion petrologica y geoquimica de un complejo de domos topaciferos en el campo volcannico de San Luis Potosi (Mexico). Petrologic and geochemical evolution of a topaz–bearing dome complex in the San Luis Potosi volcanic field (Mexico). Revista Mexicana de Ciencias Geologicas 24:328–343

Roedder, E., 1984, Fluid inclusions: Mineral. Soc. Am., Reviews in Mineralogy, v. 12, 644 p.

Rubin JN, Kyle JR (1988) Mineralogy and geochemistry of the San Martin skarn deposits, Zacatecas, Mexico. Economic Geology 83:1782–1801

Saunders JA, Brueseke ME (2012) Volatility of Se and Te during subduction-related distillation and the geochemistry of epithermal ores of the western United States: Economic Geology, v. 107, p. 165–172.

Saunders, J.A., Mathur, R., Kamenov, G.D., Shimizu, T., and Brueseke, M.E., 2016, New isotopic evidence bearing on bonanza (Au-Ag) epithermal ore-forming processes: Mineralium Deposita, v. 51, p. 1–11.

Seedorff E, Dilles JH, Proffett JM Jr., Einaudi MT, Zurcher L, Stavast WJA, Johnson DA, and Barton MD (2005) Porphyry deposits: Characteristics and origin of hypogene features: ECONOMIC GEOLOGY 100TH ANNIVERSARY VOLUME, p. 251−298.

Sillitoe RH, (1999) Styles of high–sulphidation gold, silver and copper mineralisation in porphyry and epithermal environments; PACRIM '99 congress; proceedings [modified]. Publication Series – Australasian Institute of Mining and Metallurgy 4:29–44

Sillitoe RH, Hedenquist JW (2003) Linkages between volcanotectonic settings, ore–fluid compositions, and epithermal precious metal deposits; Volcanic, geothermal, and ore–forming fluids; rulers and witnesses of processes within the Earth. Special Publication (Society of Economic Geologists (U.S.)) 10:315–343

Simmons SF (1991) Hydrologic implications of alteration and fluid inclusion studies in the Fresnillo District, Mexico; evidence for a brine reservoir and a descending water table during the formation of hydrothermal Ag–Pb–Zn orebodies. Economic Geology and the Bulletin of the Society of Economic Geologists 86:1579–1601

Simmons, S.F., White, N.C., John, D.A., 2005, Geological characteristics of epithermal precious and base metal deposits: Economic Geology 100th Anniversary Volume, p. 485–522.

Simonetti A, Heaman LM, MacHattie TG, Chacko T, Hartlaub RP, Eccles DR (2005) In–situ petrographic thin section U–Pb dating of zircon and titanite by laser ablation–MC–ICP–MS; Abstracts of the 15th annual V. M. Goldschmidt conference. Geochimica et Cosmochimica Acta 69:381

Smith LD, Jones RL (1979) Thermal Anomaly in Northern Mexico: An extension of the Río Grande Rift (?). In Río Grande Rift: Tectonics and Magmatism RE Rieckers (ed) American Geophysic Union 269–278

Solé J, Salinas JC, González-Torres E, Cendejas-Cruz JE, (2007) Edades K/Ar de 54 rocas ígneas y metamórficas del occidente, Centro y Sur de México: Revistas Mexicana de Ciencias Geológicas, v. 24, no. 1, p. 104-119

Shore M, Fowler AD (1996) Oscillatory zoning in minerals: a common phenomenon. The Canadian Mineralogist, vol 34: 1111–1126

Staude JM and Barton MD (2001) Jurassic to Holocene tectonics, magmatism, and metallogeny of northwestern Mexico: Geological Society of America Bulletin, v. 113, 1357–1374

Stein G, Lapierre H, Monod O, Zimmermann JL, Vidal R (1993) Petrology and some Mexican Mesozoic plutons–sources and tectonic environments. Journal of South American Earth Sciences 7:1–7

Steel JS (2012) Technical Report on the Catanava Gold Property, Pinos, Zacatecas State, Mexico. NI 43-101 technical report prepared by Mining Insights Inc. for Excalibur Resources Ltd., effective date April 20, 2012

Stewart JH (1998) Regional characteristics, tilt domains, and extensional history of the later Cenozoic Basin and Range Province, western North America; Accommodation zones and transfer zones; the regional segmentation of the Basin and Range Province: Special Paper – Geological Society of America 323:47–74

Stolz AJ, Jochum KP, Spettel B, Hofmann AW (1996) Fluid– and melt–related enrichment in the subarc mantle Evidence from Nb/Ta variations in island–arc basalts. Geology 24:587–590

Sun S, McDonough WF (1989) Chemical and isotopic systematics of oceanic basalts: Implications for mantle composition and processes. In: Saunders AD, Norry MJ (eds) Magmatism in the Ocean Basins. Geological Society of London Special Publication 42:313–345.

Talavera-Mendoza, O., Ramirez-Espinosa, J., and Guerrero-Suástegui, M., 1995, Petrology and geochemistry of the Teloloapan subterrane, a Lower Cretaceous evolved intra-oceanic island-arc: Geofísica Internacional, v. 34, p. 3–22.

Tardy M, Lapierre H, Boudier JL, Yta M, Coulon C (1991) The Late Jurassic-Early Cretaceous of western Mexico (Guerrero Terrane) origin and geodynamic evolution: Universidad Nacional Autónoma de México, Instituto de Geología Universidad Autónoma de Hidalgo, Instituto de Investigación de Ciencias de la Tierra; Sociedad Mexicana d Mineralogía; Secretaría de Educación Pública. Subsecretaría de Educación Superior e Investigación Científica, Convención sobre la Evolución Geológica de México y Primer Congreso Mexicano de Mineralogía, Pachuca, Hidalgo., p. 213-215.

Tristan-Gonzalez M (1986) Estratigrafia y tectonica del Graben de Villa de Reyes, en los estados de San Luis Potosi y Guanajuato, Mexico. Universidad Autonoma de San Luis Potosi, Instituto de Geologia 107: 1–91

Tristan-Gonzalez M (2008) Evolucion tectono-volcanica durante el Paleogeno en la porcion sur-oriental de la Mesa Central. Universidad Nacional Autonoma de Mexico

Tristan-Gonzalez M, Aguirre-Diaz GJ, Labarthe-Hernandez G, Torres-Hernandez JR, Bellon H (2009) Post–Laramide and pre–Basin and Range deformation and implications for Paleogene (55–25 Ma) volcanism in central Mexico; a geological basis for a volcano–tectonic stress model; Understanding stress and deformation in active volcanoes. Tectonophysics 471:136–152

Tristan-Gonzalez M, Torres-Hernandez JR, Labarthe-Hernandez G, Aguillon-Robles A, Yza-Guzman R (2012) Control estructural para el emplazamiento de vetas y domos félsicos en el distrito minero de Zacatecas, Mexico. Boletin de la Sociedad Geologica Mexicana. V 64, 3:353–367

Velador JM (2010) Timing and origing of intermediate sulfidation epithermal veins and geochemical zoning in the Fresnillo district, Mexico: constrained by $^{40}Ar/^{39}Ar$ geochronology, fluid inclusions, gas analysis, stable isotopes, and metal ratios. The New Mexico Institute of Mining and Technology

Velador JM, Heizler MT, Campbell AR (2010) Timing of magmatic activity and mineralization and evidence of a long–lived hydrothermal system in the Fresnillo silver district, Mexico; constraints from $^{40}Ar/^{39}Ar$ geochronology. Economic Geology and the Bulletin of the Society of Economic Geologists 105:1335–1349

Verma SP (1984) Sr and Nd isotopic evidence for petrogenesis of mid–Tertiary felsic volcanism in the mineral district of Zacatecas, Zac. (Sierra Madre Occidental), Mexico. Chemical Geology – Isotope Geoscience 46:37–53

Wincester JA, Floyd PA (1977) Geochemical discrimination of different magma series and their differentiation products using immobile elements. Chemical Geology, 20:325–343

Yta, M., 1992, Etude geodynamique et metallogenique d' un secteur de la "Faja de Plata", Mexique La zone de Zacatecas-Francisco I Madero-Saucito: L' Orleáns, [Doctorate dissertation], p. 1-48

Figure Captions

Figure 1. Geology of northern Mexico showing epithermal deposits of the Mexican Silver Belt, key terrane boundaries, and areas of Basin and Range extension with associated mid-Cenozoic rhyolites of the Sierra Madre Occidental (based on maps from Ortega-Gutiérrez et al., 1995; Albinson et al., 2001; Ferrari et al., 2002, 2007; Aguirre-Diaz and Labarthe-Hernandez, 2003; Nieto-Samaniego et al., 2007).

Figure 2. Map of central Mexico showing the distribution of Eocene red-bed conglomerates, combined mesothermal - epithermal deposits, topaz-bearing rhyolites (32–27 Ma), grabens (Aguacalientes (GA), Villa de Reyes (GV), Juchipila (GJ), Tlatenango (GT), and Bolaños (BG)), and NNE- and NNW-trending normal faults related to Basin and Range extension. Mesothermal deposits include skarn-, chimney-, and manto-type deposits (based on maps from the Mexican Geological Service)

Figure 3. Relative metal contents and fluid inclusion salinities of various Mexican epithermal deposits (compositional data from Albinson et al., 2001; ages compiled by Camprubí et al., 2003, and references therein; * this study).

Figure 4. Maps showing veins infilling NNE- and NNW-striking normal faults in the Bolañitos (Guanajuato) and Pinos (Zacatecas) low-sulfidation deposits (modified from: Steel, 2012, and Munroe, 2014). Coordinates are in UTM, ITRF92 datum, zone 13.

Figure 5. Geological map of the Zacatecas district showing the main vein systems and geochronological sample locations (modified from Perez-Martinez et al., 1961; Ponce et al., 1988; Mexican Geological Service maps Zacatecas F13-B58_GM, Guadalupe F13-B68_GM, and Jerez F13-B67_GM). UTM, ITRF92 datum, zone 13.

Figure 6. Photographs of Zacatecas district rocks: (a) Metamorphosed clastic sediments of the Triassic Zacatecas Formation (746689E, 2523038N); (b) Late Jurassic–Early Cretaceous impure limestone (747365E, 2523876N), and (c) andesitic to basaltic pillow lavas (746787E, 2523891N); (d) Eocene Zacatecas red conglomerate showing clasts of andesitic rocks, phyllite, and schist in a reddish sandy matrix (748466E, 2518169N). All coordinates are in UTM, ITRF92 datum, zone 13.

Figure 7. Hand samples and photomicrographs of representative Late Jurassic–Early Cretaceous volcano-sedimentary lithologies. (a–c) Sample of basaltic andesite (S41-683; 747355E, 2524201N) showing porphyritic texture in hand sample (a) and phenocrysts of plagioclase (b) and olivine (c) in a groundmass of plagioclase microlites. (d) Sample of shale (S179-402; 747225E, 25242350N) showing grey and black laminations crosscut by a vein; (e) fine-grained disseminated and (f) framboidal pyrite in shale.

Figure 8. Photographs showing Eocene igneous rocks. (a) Surface outcrop of the La Sierpe plug showing vertical flow-banded texture (vertical face; 746966E, 2523906N). (b) Sample of drillcore of the La Sierpe plug at depth showing porphyritic texture (drillhole COS-41 at 896 m depth; 747372E, 2524200N). (c) Magmatic breccia with globular peperitic texture of grey rounded and white lobate clasts of porphyritic rhyolite in a matrix of black fine-grained metasediment (DDH S-179 from 633–636m). (d) Breccia with angular fragments of rhyolite cemented by chalcopyrite-pyrite-bearing quartz (DDH U-375 from 378–379m). (e)

Panoramic view looking northwest showing the eastern end of the la Bufa dome and its continuation to the east as the La Cantera dike (photograph taken from 751947E, 2520682N). (f) Panoramic view to the southeast sowing the El Padre plug intruding the Zacatecas red conglomerate, the La Virgen ignimbrite lying discordantly on top of the Zacatecas red conglomerate, and the volcanic breccia at the base of the La Virgen ignimbrite (photograph taken from 748328E, 2518097N). (g) Close up of the volcanic breccia outcrop in d showing blocks up to 40 cm wide (748887E, 2517362N). All coordinates are in UTM, ITRF92 datum, zone 13.

Figure 91. Photomicrographs of the Eocene igneous rocks. (a) Sample from the La Bufa rhyolitic dome showing cavities after argillized feldspars and oxidized biotite in a glassy matrix (ZABU-01; 750195E, 2520755N). (b) Sample from the La Sierpe rhyolitic plug showing sericitized plagioclase, oxidized biotite, and partially reabsorbed quartz phenocrysts set in a cryptocrystalline matrix (ZASI-02; DDH S-41 at 896 m: 747327E, 2524177N). (c) Sample of the El Padre rhyolitic plug showing fine-grained oxidized biotite and dusty aspect of altered orthoclase in a partially devitrified matrix (ZAPA-03; 748383E, 2517921N). (d) Sample from the La Virgen ignimbrite showing preserved glass shards in a partially devitrified matrix and euhedral quartz crystals growing in vesicles (ZAVI-04; 746915E, 2515212N).

Figure 10. Photographs showing macroscopic textures of sinter deposits. (a) Vertical section of a sample of sinter showing subhorizontal bands of amorphous silica. (b, c) Plan views showing circular and polygonal mud-crack structures, respectively (E742718, N2512882).

Figure 11. Hand sample photographs and photomicrographs from Mala Noche drill core showing alteration of Jurassic–Cretaceous volcano-sedimentary rocks. (a) Hornfels consist of laminations of hardened grey to black shale and fine-grained quartzite interbanded with chlorite-epidote layers. (b) Pyrite and sphalerite replacing chlorite-epidote laminations (DDH S-41 at 754 m; projected sample location 747355E, 2524201N). (c) Polished section of b showing chlorite-epidote and pyrite in plane polarized reflected light (RL). (d) Close up of c showing pyrite replacing epidote crystals in reflected light. (e) Sample of marble (DDH S198 at 267m; projected sample location E745320, N2524,692). (f) Photomicrograph of e showing a roughly equigranular mosaic of calcite and dolomite

Figure 12. Back scattered electron (BSE) images and photomicrographs showing skarn-type alteration minerals from the Mala Noche mine and drill core samples: (a) BSE image of wolframite associated with magnetite; sample from underground mine level 9-W (747445E, 2523630N at 2205 masl). (b) BSE image of sample Cos-37 (DDH U-37 at 164 m; 747779E, 2523876N) showing hedenbergite altered to Fe-Mg hydrosilicates (grunerite–cummingtonite). (c) Photomicrograph of sample S-64 (DDH S-64 at 64 m; projected sample location 747172E, 2523732N) showing isotropic subhedral garnet crystals under crossed nicols. (d) Rounded crystals altered to Fe-hydrosilicates and replaced by chalcopyrite (sample Cos-37). (e) Photomicrograph of sample from underground level 10 (748139E, 2523400N at 2154 masl) showing hedenbergite retrograded to nontronite and replaced by chalcopyrite, and (f) back scattered electron image of stilpnomelane replacing chalcopyrite.

Figure 13. Photographs and reflected light photomicrographs of the Mala Noche skarn-type high Cu grade samples showing mineral associations and textures: (a) Sample from DDH U-39 (projected sample location E748097, N2523786 at 173.5 m) showing pyrrhotite replacing chalcopyrite and intergrown with ilvaite crystals. (b) Photo from underground wall level 9.3–W, showing semi-massive chalcopyrite replacing tabular bladed crystals (probably amphiboles). (c) Mineral association of pyrite, magnetite, and chalcopyrite in a groundmass of grey quartz (sample from underground level 9 west). (d) Close-up of c showing texture of marcasite and pyrite replacing radially elongated crystals of possible amphibole precursors. (e–f) Photomicrographs showing alteration and remnants of hedenbergite replaced by chalcopyrite and rimmed by pyrrhotite (e, transmitted light; f, reflected light; sample from DDH U-39; projected sample location E748097, N2523786 at 171 m). (g–h) Photomicrographs in transmitted and reflected light, respectively, showing isometric crystals (possible garnet) replaced by chalcopyrite and pyrrhotite surrounded by Fe-hydrosilcates (from DDH U-37; projected sample location E747779, N2523876 at 162 m). (i) Euhedral isometrically shaped crystal (probably garnet) replaced by chalcopyrite, pyrrhotite, and minor sphalerite (DDH U-37; projected sample location E747779, N2523876 at 162 m). (j) Sample from DDH U-202 (projected sample location E747827, N2523550) showing pyrrhotite and chalcopyrite replacing galena along cleavage planes.

Figure 14. Mineral paragenesis of the Mala Noche skarn and intermediate-sulfidation epithermal mineralization.

Figure 15. Mala Noche skarn-type mineralization showing post-mineral deformational textures in massive sulfides. (a) Hand specimen photograph of sheared galena with a folded band of sphalerite, and sigmoidal shaped lens of chalcopyrite and pyrite. Reflected light photomicrographs of: (b) sigmoidal shaped aggregate of chalcopyrite and pyrite; (c) cataclastic texture in pyrite and chalcopyrite; (d) fractured crystals of galena; (e) deformed triangular cleavage pits in galena; (f) lineaments of rounded quartz grains in galena that exhibit undulose extinction in transmitted light.

Figure 16. Photographs and photomicrographs of the Mala Noche Zn-Pb-Ag-rich intermediate-sulfidation epithermal mineralization showing textures and ore mineral associations: (a) Early sulfide-rich vein showing discontinuous bands of sphalerite, galena, pyrite, and crustiform quartz with vuggy cavities at the center. (b) Later sulfide-poor vein showing crustiform amethystine quartz. (c) Cockade texture formed by crustiform quartz that coats pre-existing fragments of galena. (d) Mineral association of galena, sphalerite, and blebs of chalcopyrite. (e) Micro-veinlet of quartz with sphalerite and acanthite crosscutting skarn-type stage chalcopyrite and associated alteration minerals. (f) Photomicrograph showing undeformed triangular cleavage pits in galena.

Figure 17. Mineral paragenesis of the Veta Grande Vein.

Figure 18. Hand samples and photomicrographs showing representative features of the Veta Grande stage I mineralization. (a) Southeast breccia showing fragments of volcanic rocks and a quartz-sulfide matrix (sample SA-1 from the El Refugio level; 752468E, 2526042N). (b) Northwest breccia showing fragments of sedimentary rocks and carbonate-sulfide matrix (sample OSDH6-S14 from drillhole 08VGX006; projected sample location 750090E, 2527129). (c) Vein sample showing the dated adularia associated with sulfides, ankerite, and calcite (sample VG1B-S8 from drillhole 08VGX001B; projected sample location 750738E, 2526639). (d) Reflected light microphotograph of sample shown in c showing euhedral quartz and adularia crystals associated with pyrite, sphalerite, and galena. (e, f) Reflected light microphotographs showing the association of Ag-bearing minerals with

base-metal sulfides (e: sample OSDH1B-S4 from drillhole 08VGX001B projected sample location 750738E, 2526639; f: sample DP-04 from the Santa Rita level, 749815E, 2527748N).

Figure 19. Hand samples and microphotographs showing representative features of the Veta Grande stage II mineralization. (a) Crustiform banding and prismatic crystalline quartz, amethyst, and chalcedony, with discontinuous bands containing sulfides and sulfosalts (dark bands; sample SA-3; surface sample location 751685E, 2526286N). (b) Stage II quartz enclosing fragments of stage I breccia (sample from drillhole SAD9536; projected sample location 751678E, 2526252N). Reflected light microphotographs: (c) supergene replacement of galena by anglesite; (d) supergene oxidation of pyrite to goethite associated with a halo of supergene anglesite replacing galena; (e) supergene replacement of chalcopyrite by bornite, and bornite by covellite; (f) native silver in a fracture associated with oxidized sulfides.

Figure 20. Mineral paragenesis of the El Compas Vein.

Figure 21. Hand samples and microphotographs showing representative features of the El Compas vein (El Orito System). (a) Hand sample stained with sodium cobaltinitrite showing alternating bands of greenish to white quartz, calcite, and adularia (stained yellow; sample from the El Compas underground mine, level 7). (b) Hand specimen showing bladed calcite texture with interstitial microcrystalline quartz and pinacoids of calcite (sample from the El Compas mine dump; 747259E, 2515568N). (c, d) Thick section of a sample from the El Compas underground mine stock pile showing flamboyant and plumose textures, in plane- and cross-polarized light. (e) Scanned thick section showing electrum, aguilarite, and naumannite related to bands of microcrystalline quartz and adularia (sample from drillhole 09COM043 at 63 m). (f) Close up of e in reflected light showing aguilarite and electrum grains set in a matrix of quartz and adularia.

Figure 22. Structural maps of the (a) Veta Grande, and (b) La Cantera ENE-striking dextral strike-slip fault systems, and (b) El Orito N–S-striking normal fault system (modified from Perez-Martinez et al., 1961).

Figure 23. Surface map of the El Compas veins showing second-order NW-striking vein patterns.

Figure 24. (a) Total alkali vs. silica diagram (LeBas et al., 1986); alkaline-subalkaline boundary from Irvine and Baragar (1971) showing the major element classification of the Jurassic–Cretaceous lava flows and Eocene volcanic and hypabyssal rocks from the Zacatecas district; and (b) Zr/TiO_2 vs. Nb/Y diagram (Winchester and Floyd 1977) showing their corresponding trace element classification.

Figure 25. (a) Chondrite-normalized REE diagram, and (b) primitive mantle-normalized extended trace element diagram for samples from the Zacatecas district (normalization values of Sun and McDonough, 1989). The compositional ranges of the lower and upper volcanic sequences of the southern Mesa Central are shown in dark and light gray, respectively (data from Orozco-Esquivel et al., 2002).

Figure 26. Apparent $^{40}Ar/^{39}Ar$ age spectra and inverse isochron diagrams for adularia samples from (a) the Veta Grande vein (VG1B-08), and (b) the El Compas vein (COM-L7). All errors are drawn at 1σ error, but calculated ages are reported to 2σ.

Figure 27. Tera-Wasserburg concordia diagrams for volcanic and hypabyssal rocks of the Zacatecas district. See text for details.

Figure 28. (a) Plot of Th versus SiO_2 for Eocene volcanic and hypabyssal rocks from the Zacatecas district and the southern Mesa Central (upper and lower volcanic sequences; Orozco-Esquivel et al., 2002). (b) Initial strontium isotope ratios versus silica contents for the Zacatecas district felsic volcanic and subvolcanic intrusive rocks (Verma, 1984) and for the southern Mesa Central (upper and lower sequences; Orozco-Esquivel et al., 2002).

Figure 29. Summary of U-Pb and $^{39}Ar/^{40}Ar$ geochronology from this study; tectonic setting and type of volcanism from Tristan-Gonzalez et al. (2009).

Figure 30. Possible models of fault kinematics and stress field for the Zacatecas fault systems. (a) Transtensional stress regime prevalent in the Eocene-Oligocene, proposed by Nelson (2005): here, the El Orito vein is interpreted to represent a secondary fault (R') related to the La Cantera main fault. The inset shows a Riedel model for a dextral strike-slip system (Petit,

1987). Model proposed here and by Tristan-Gonzalez et al. (2012) for a transtensional stress regime in the Eocene (b), overprinted by Basin and Range extension in the Oligocene (c). Abbreviations: M = main fault plane; R = synthetic secondary shears; R' = antithetic secondary shears.

Figure 31. Cartoons showing a model for the multiple mineralization events in the Zacatecas district (see text for explanation).

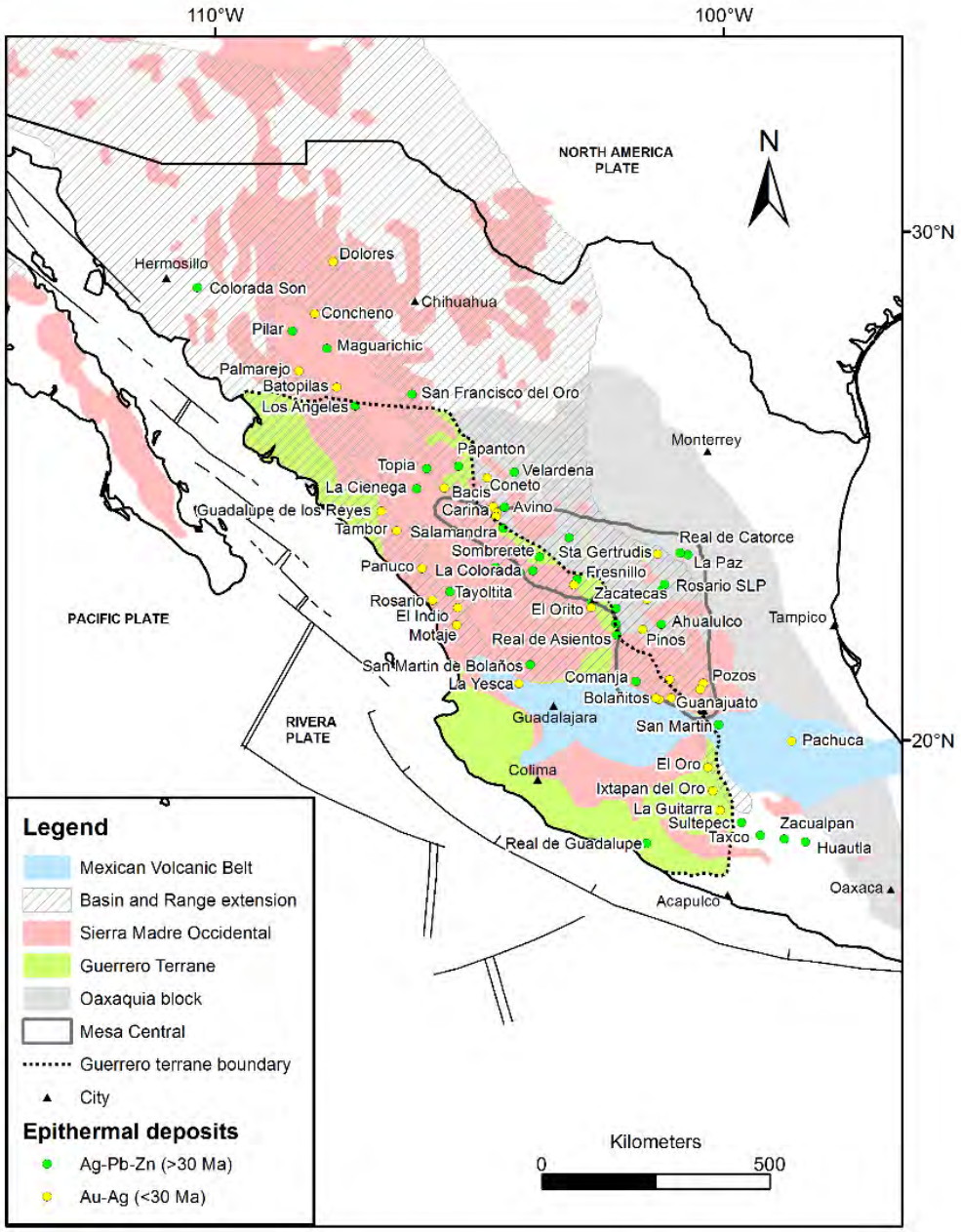

Figure 1. Geology of northern Mexico showing epithermal deposits of the Mexican Silver Belt, key terrane boundaries, and areas of Basin and Range extension with associated mid-Cenozoic rhyolites of the Sierra Madre Occidental (based on maps from Ortega-Gutiérrez et al., 1995; Albinson et al., 2001; Ferrari et al., 2002, 2007; Aguirre-Diaz and Labarthe- Hernandez, 2003; Nieto-Samaniego et al., 2007).

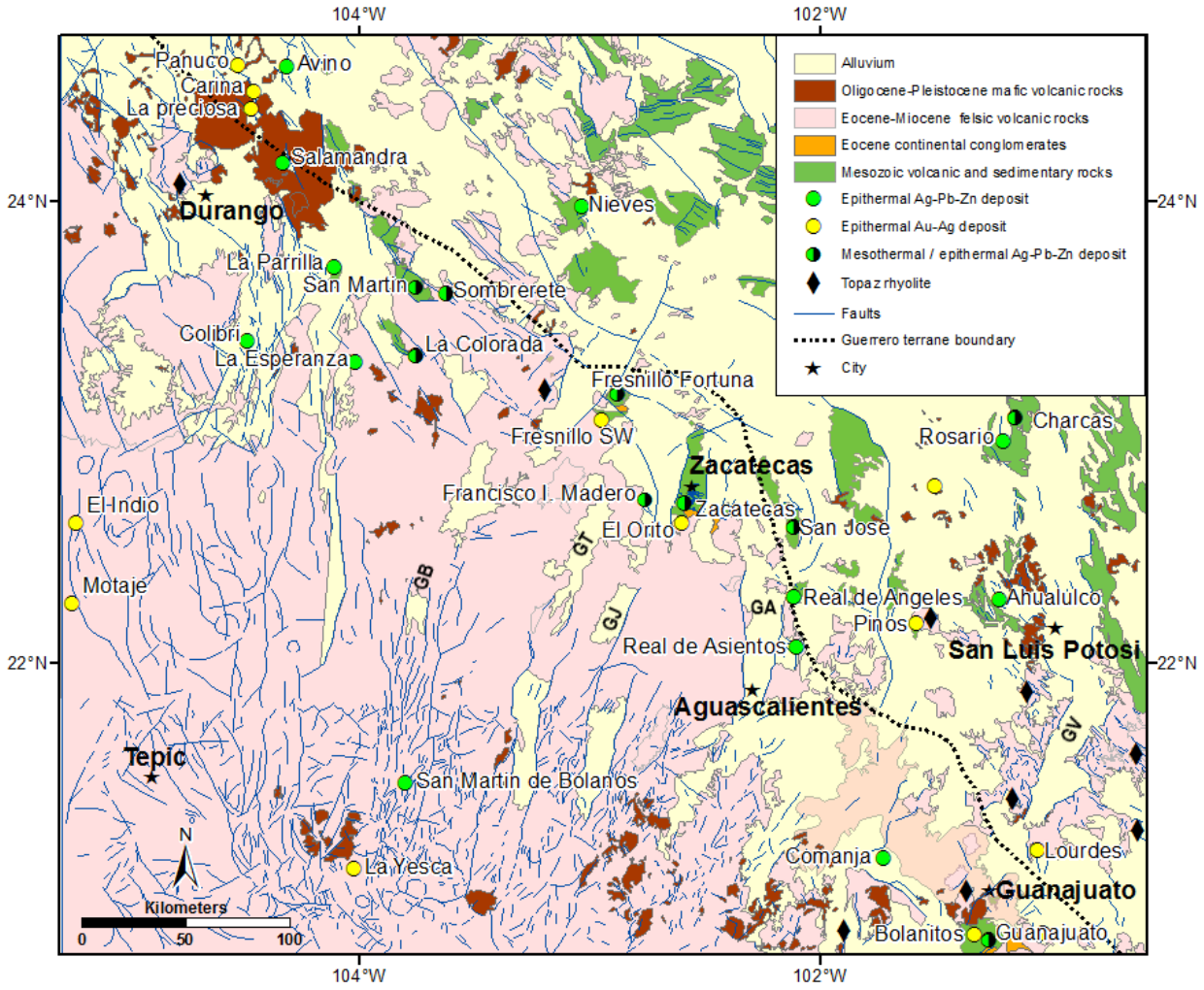

Figure 2. Map of central Mexico showing the distribution of Eocene red-bed conglomerates, combined mesothermal - epithermal deposits, topaz-bearing rhyolites (32–27 Ma), grabens (Aguacalientes (GA), Villa de Reyes (GV), Juchipila (GJ), Tlatenango (GT), and Bolaños (BG)), and NNE- and NNW-trending normal faults related to Basin and Range extension. Mesothermal deposits include skarn-, chimney-, and manto-type deposits (based on the Mexican Geological Service maps).

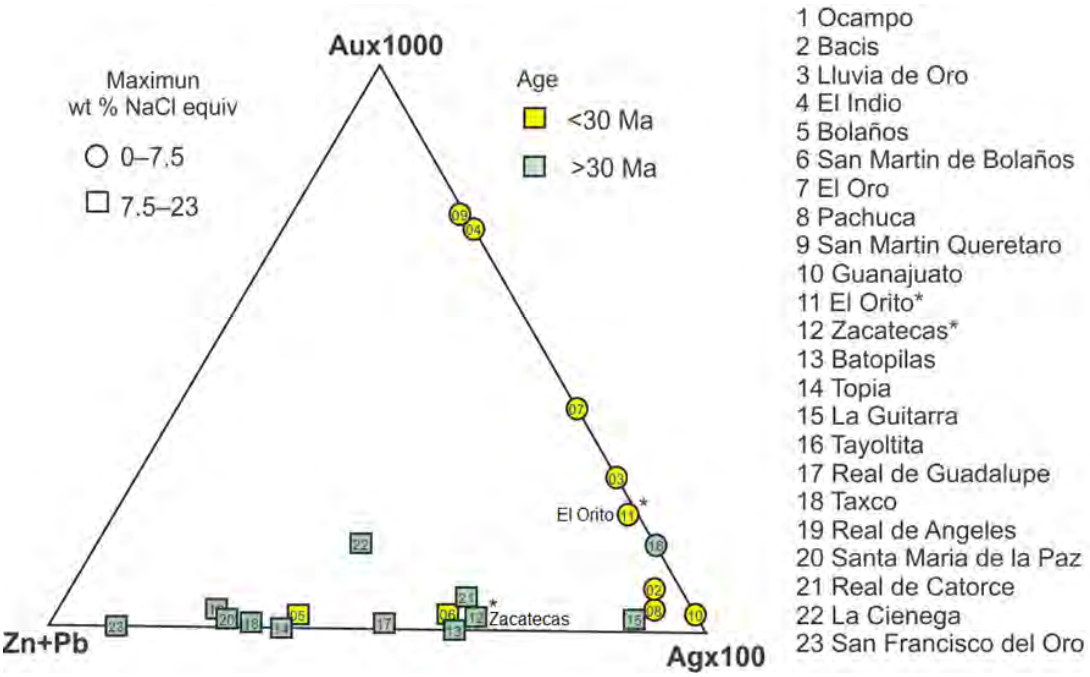

Figure 3. Relative metal contents and fluid inclusion salinities of various Mexican epithermal deposits (compositional data from Albinson et al., 2001; ages compiled by Camprubí et al., 2003, and references therein; * this study).

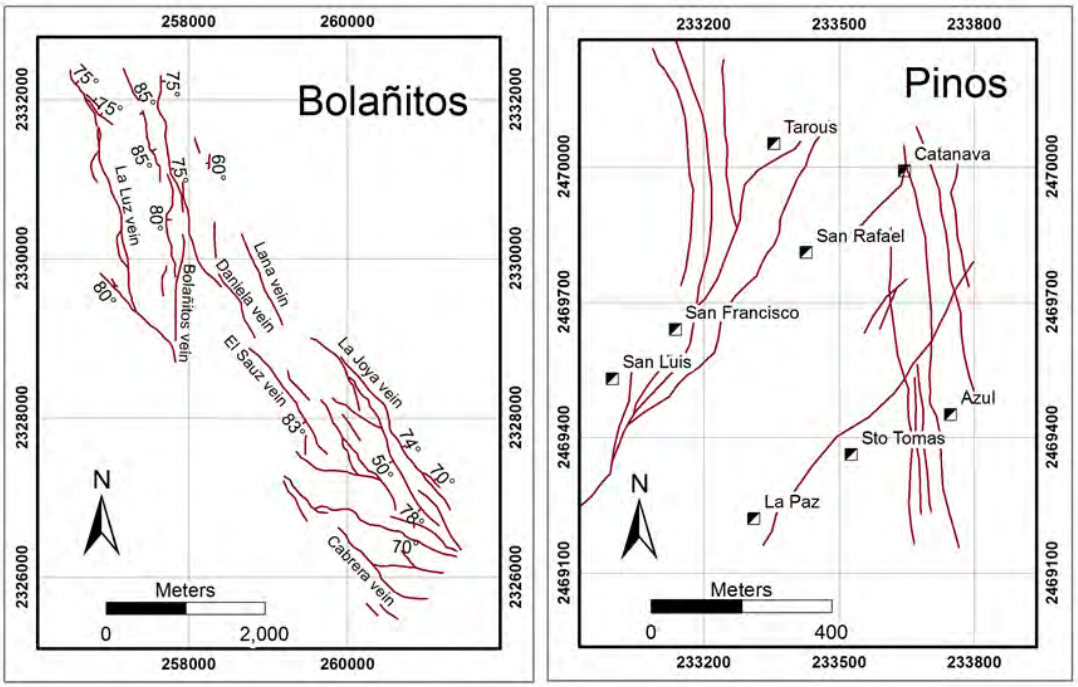

Figure 4. Maps showing veins infilling NNE- and NNW-striking normal faults in the Bolañitos (Guanajuato) and Pinos (Zacatecas) low-sulfidation deposits (modified from: Steel, 2012, and Munroe, 2014). Coordinates are in UTM, ITRF92 datum, zone 13.

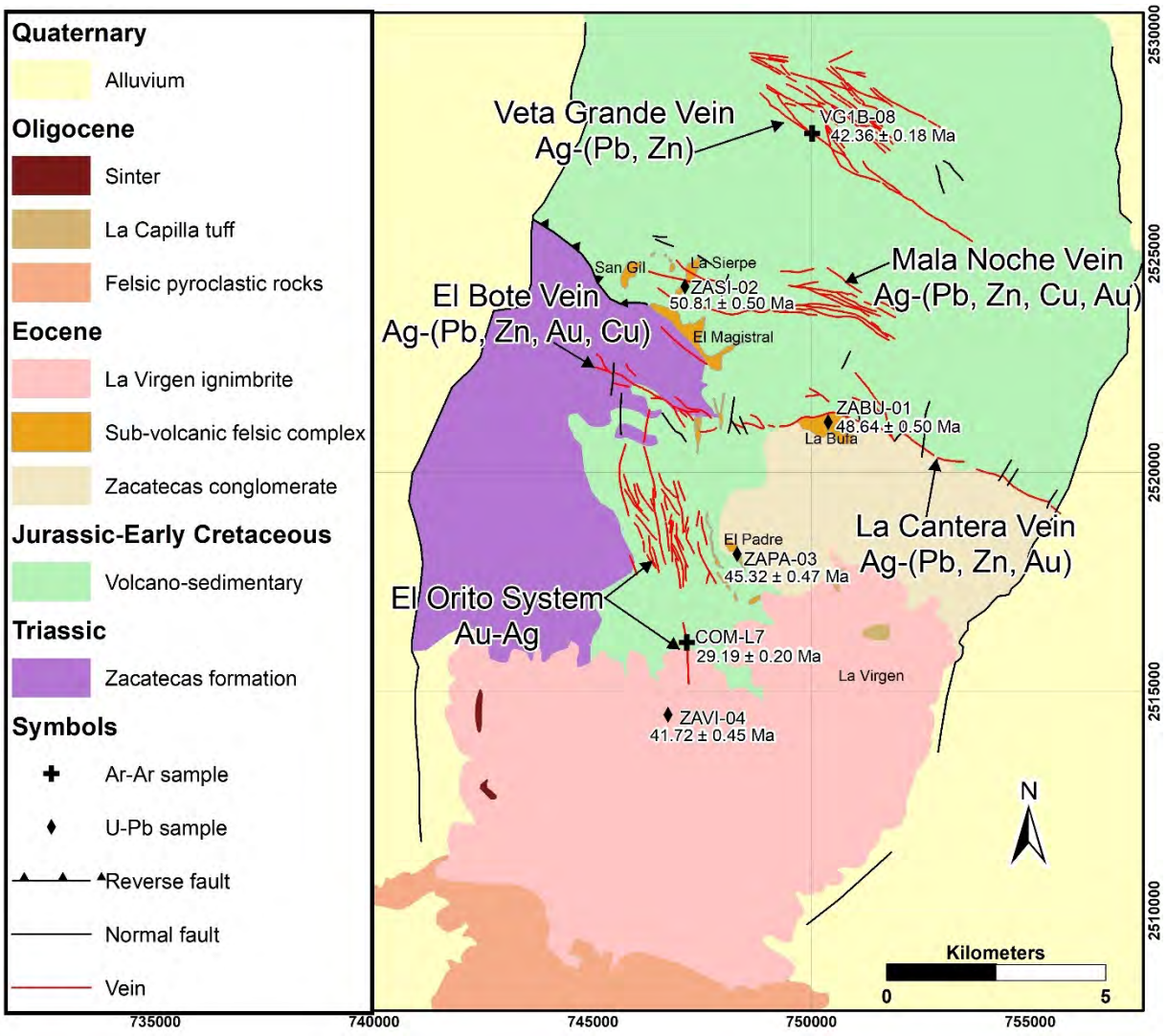

Figure 5. Geological map of the Zacatecas district showing the main vein systems and geochronological sample locations (modified from Perez-Martinez et al., 1961; Ponce et al., 1988; Mexican Geological Service maps Zacatecas F13-B58_GM, Guadalupe F13-B68_GM, and Jerez F13-B67_GM). UTM, ITRF92 datum, zone 13.

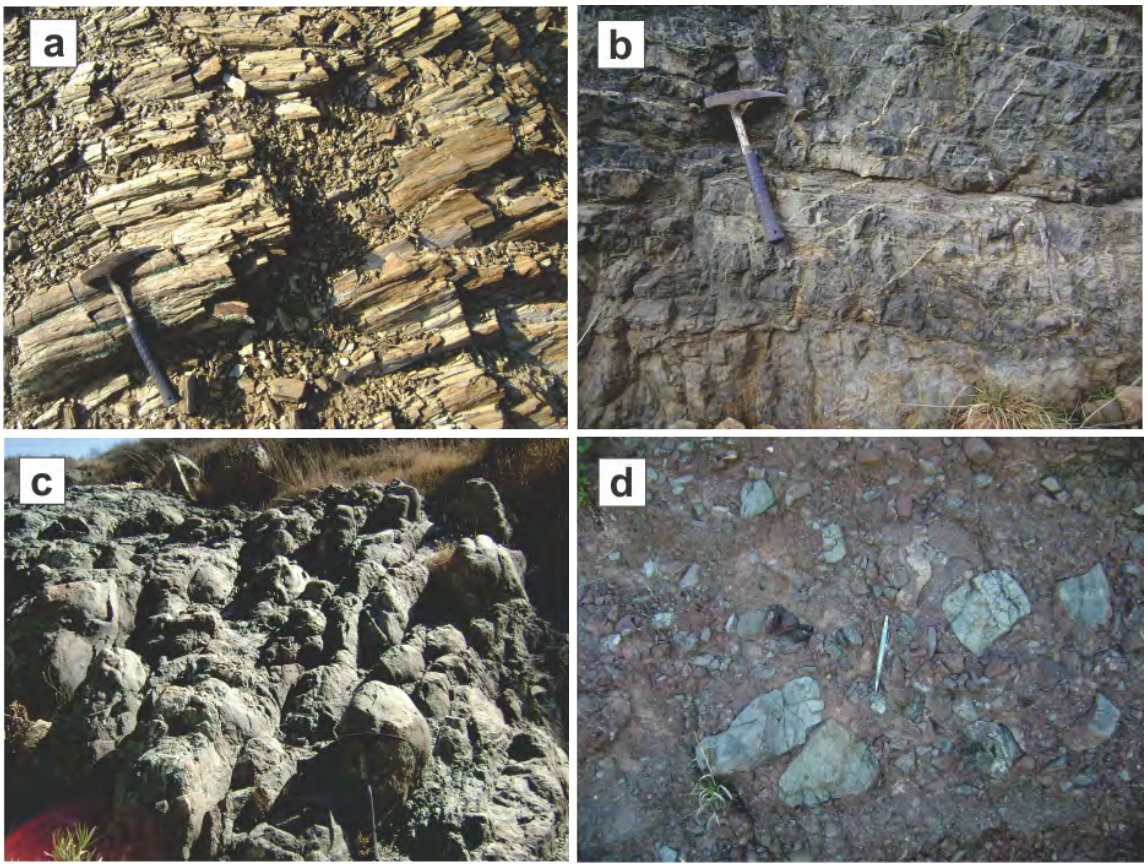

Figure 6. Photographs of Zacatecas district rocks: (a) Metamorphosed clastic sediments of the Triassic Zacatecas Formation (746689E, 2523038N); (b) Late Jurassic–Early Cretaceous impure limestone (747365E, 2523876N), and (c) andesitic to basaltic pillow lavas (746787E, 2523891N); (d) Eocene Zacatecas red conglomerate showing clasts of andesitic rocks, phyllite, and schist in a reddish sandy matrix (748466E, 2518169N). All coordinates are in UTM, ITRF92 datum, zone 13.

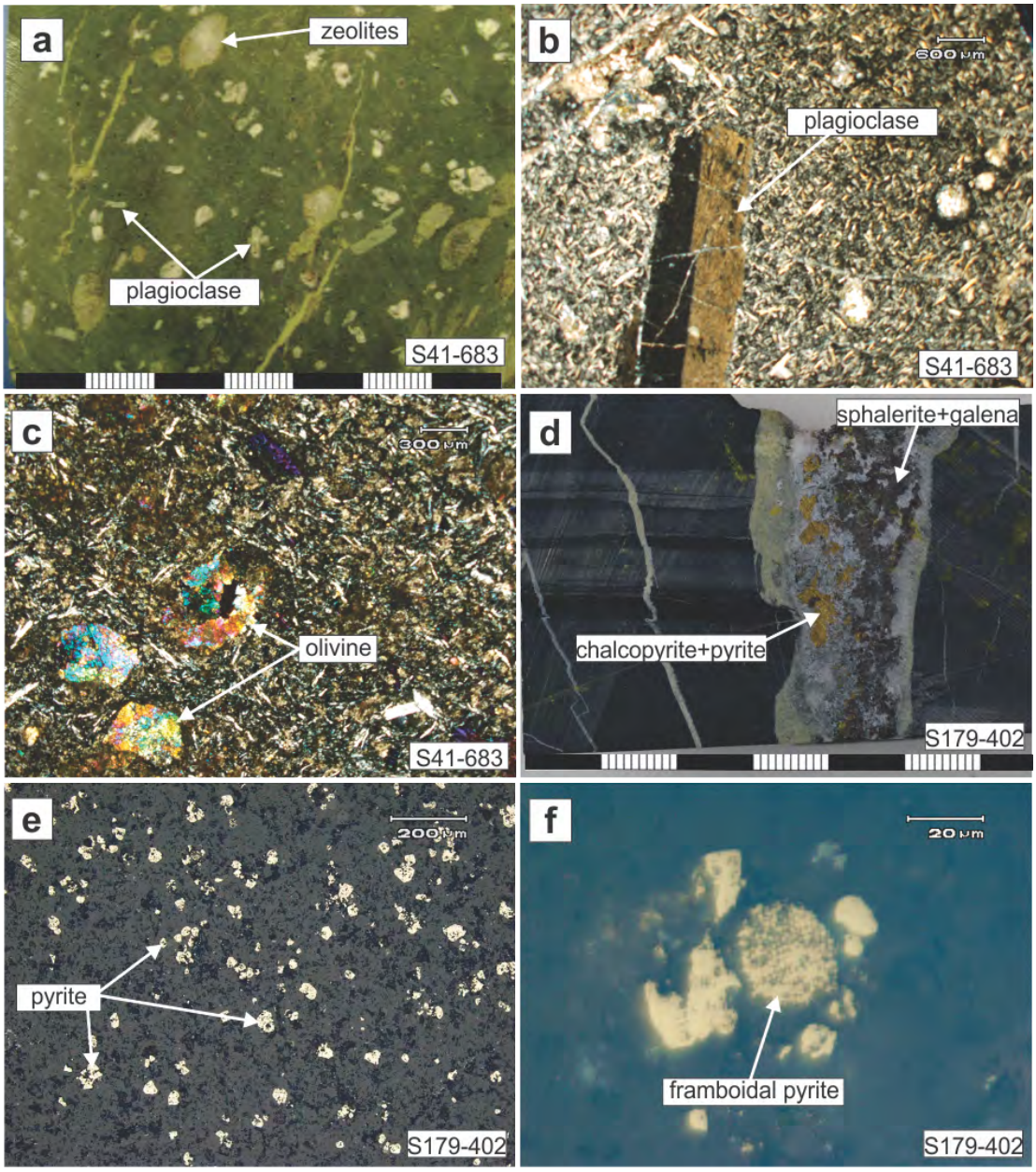

Figure 7. Hand samples and photomicrographs of representative Late Jurassic–Early Cretaceous volcano-sedimentary lithologies. (a–c) Sample of basaltic andesite (S41-683; 747355E, 2524201N) showing porphyritic texture in hand sample (a) and phenocrysts of plagioclase (b) and olivine (c) in a groundmass of plagioclase microlites. (d) Sample of shale (S179-402; 747225E, 25242350N) showing grey and black laminations crosscut by a vein; (e) fine-grained disseminated and (f) framboidal pyrite in shale.

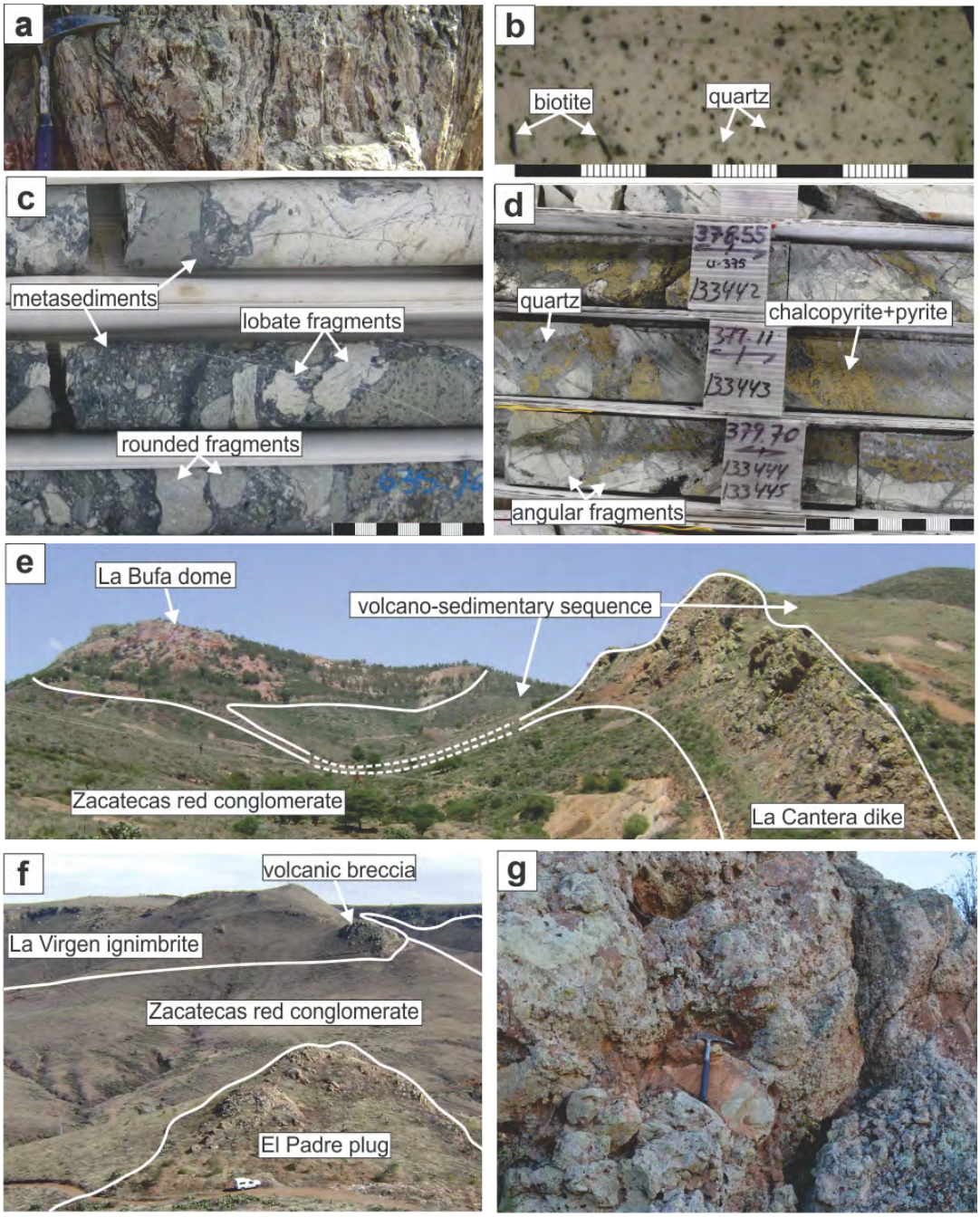

Figure 8. Photographs showing Eocene igneous rocks. (a) Surface outcrop of the La Sierpe plug showing vertical flow-banded texture (vertical face; 746966E, 2523906N). (b) Sample of drillcore of the La Sierpe plug at depth showing porphyritic texture (drillhole COS-41 at 896 m depth; 747372E, 2524200N). (c) Magmatic breccia with globular peperitic texture of grey rounded and white lobate clasts of porphyritic rhyolite in a matrix of black fine-grained metasediment (DDH S-179 from 633–636m). (d) Breccia with angular fragments of rhyolite cemented by chalcopyrite-pyrite-bearing quartz (DDH U-375 from 378–379m). (e) Panoramic view looking northwest showing the eastern end of the la Bufa dome and its continuation to the east as the La Cantera dike (photograph taken from 751947E, 2520682N). (f) Panoramic view to the southeast sowing the El Padre plug intruding the Zacatecas red

conglomerate, the La Virgen ignimbrite lying discordantly on top of the Zacatecas red conglomerate, and the volcanic breccia at the base of the La Virgen ignimbrite (photograph taken from 748328E, 2518097N). (g) Close up of the volcanic breccia outcrop in d showing blocks up to 40 cm wide (748887E, 2517362N). All coordinates are in UTM, ITRF92 datum, zone 13.

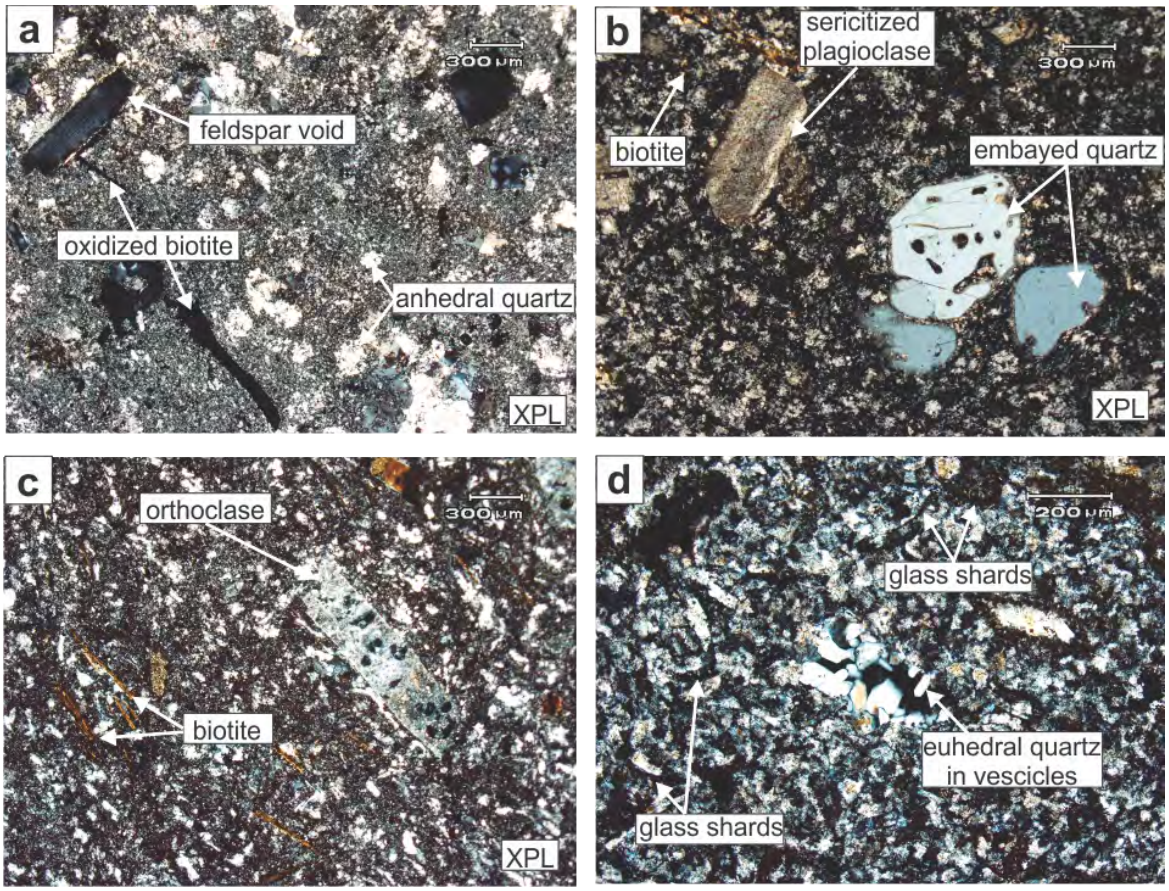

Figure 91. Photomicrographs of the Eocene igneous rocks. (a) Sample from the La Bufa rhyolitic dome showing cavities after argillized feldspars and oxidized biotite in a glassy matrix (ZABU-01; 750195E, 2520755N). (b) Sample from the La Sierpe rhyolitic plug showing sericitized plagioclase, oxidized biotite, and partially reabsorbed quartz phenocrysts set in a cryptocrystalline matrix (ZASI-02; DDH S-41 at 896 m: 747327E, 2524177N). (c) Sample of the El Padre rhyolitic plug showing fine-grained oxidized biotite and dusty aspect of altered orthoclase in a partially devitrified matrix (ZAPA-03; 748383E, 2517921N). (d) Sample from the La Virgen ignimbrite showing preserved glass shards in a partially devitrified matrix and euhedral quartz crystals growing in vesicles (ZAVI-04; 746915E, 2515212N).

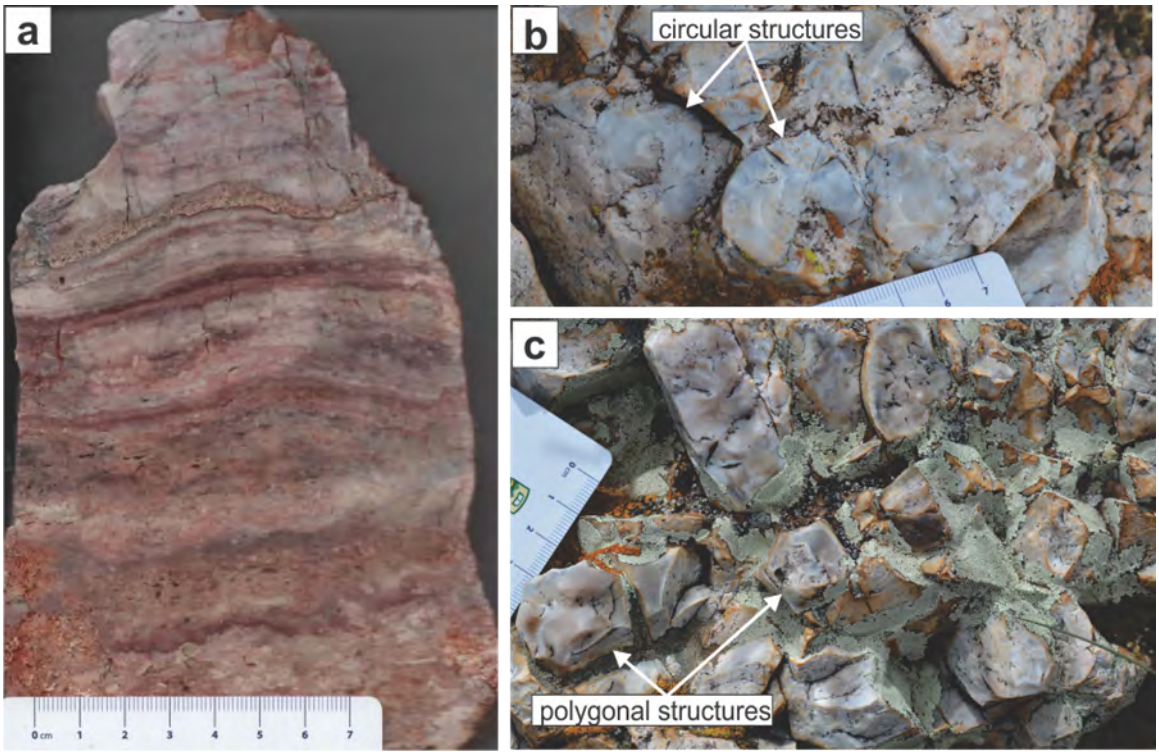

Figure 10. Photographs showing macroscopic textures of sinter deposits. (a) Vertical section of a sample of sinter showing subhorizontal bands of amorphous silica. (b, c) Plan views showing circular and polygonal mud-crack structures, respectively (E742718, N2512882).

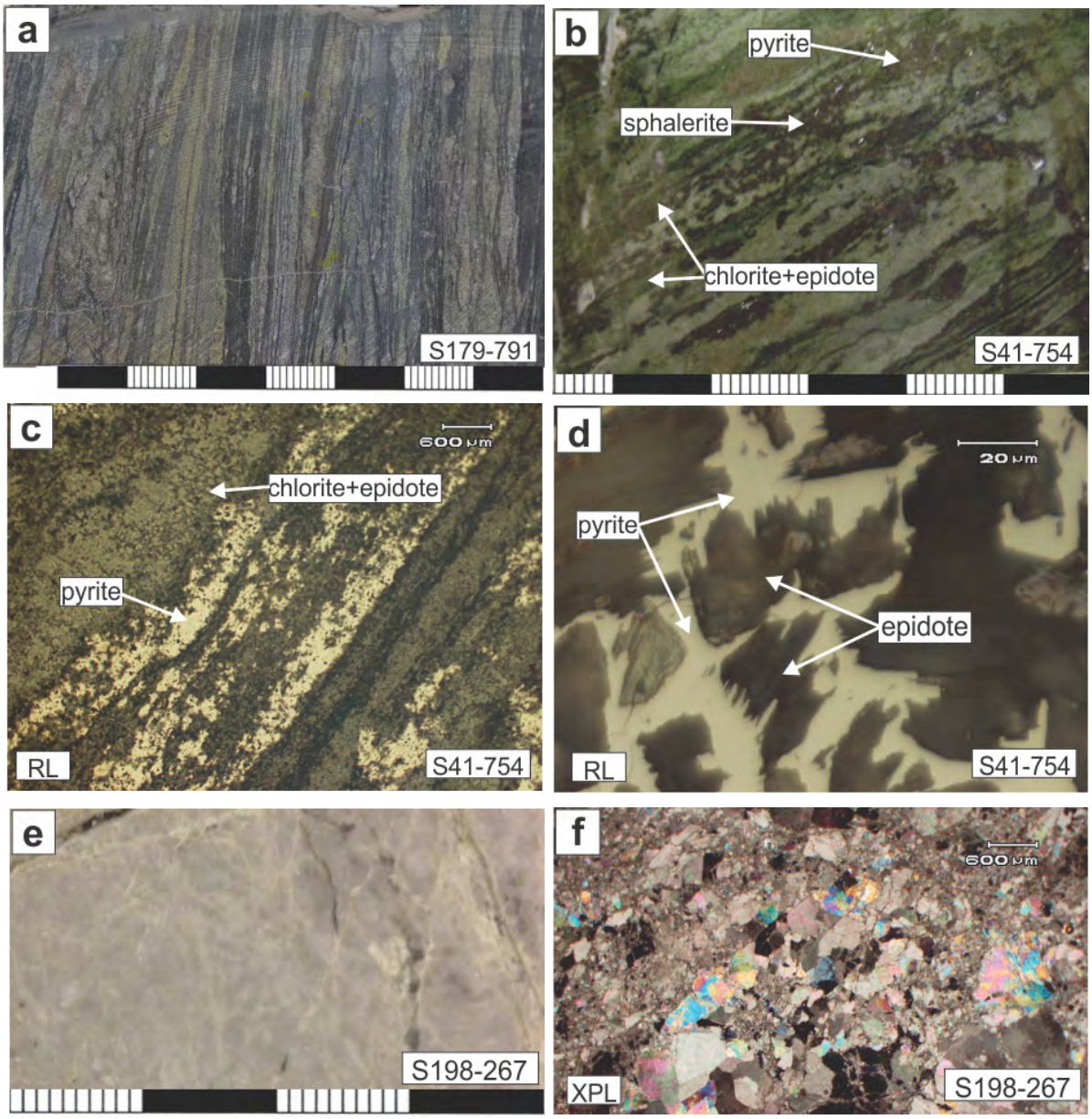

Figure 11. Hand sample photographs and photomicrographs from Mala Noche drill core showing alteration of Jurassic–Cretaceous volcano-sedimentary rocks. (a) Hornfels consist of laminations of hardened grey to black shale and fine-grained quartzite interbanded with chlorite-epidote layers. (b) Pyrite and sphalerite replacing chlorite-epidote laminations (DDH S-41 at 754 m; projected sample location 747355E, 2524201N). (c) Polished section of b showing chlorite-epidote and pyrite in plane polarized reflected light (RL). (d) Close up of c showing pyrite replacing epidote crystals in reflected light. (e) Sample of marble (DDH S198 at 267m; projected sample location E745320, N2524,692). (f) Photomicrograph of e showing a roughly equigranular mosaic of calcite and dolomite

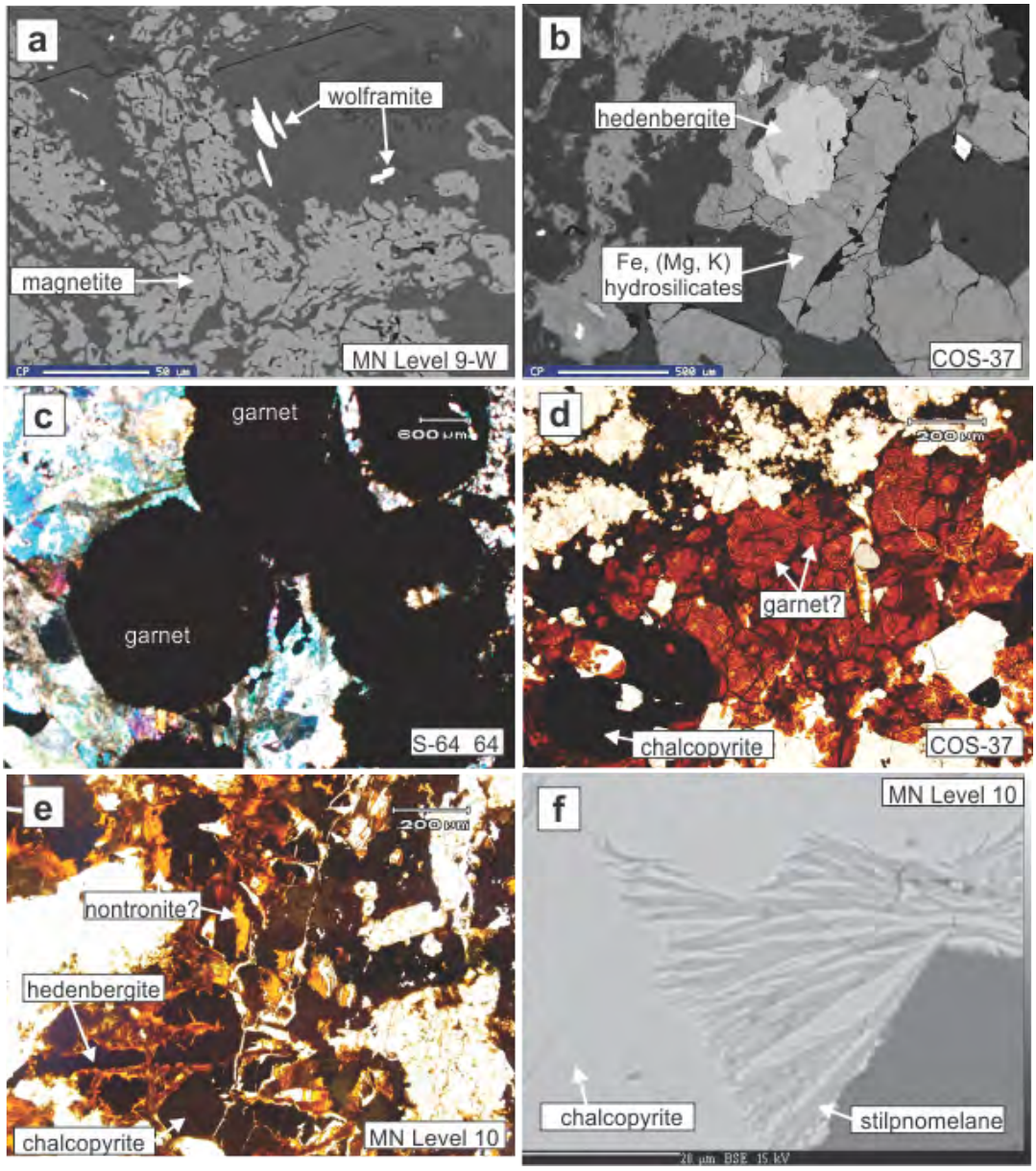

Figure 12. Back scattered electron (BSE) images and photomicrographs showing skarn-type alteration minerals from the Mala Noche mine and drill core samples: (a) BSE image of wolframite associated with magnetite; sample from underground mine level 9-W (747445E, 2523630N at 2205 masl). (b) BSE image of sample Cos-37 (DDH U-37 at 164 m; 747779E, 2523876N) showing hedenbergite altered to Fe-Mg hydrosilicates (grunerite–cummingtonite). (c) Photomicrograph of sample S-64 (DDH S-64 at 64 m; projected sample location 747172E, 2523732N) showing isotropic subhedral garnet crystals under crossed nicols. (d) Rounded crystals altered to Fe-hydrosilicates and replaced by chalcopyrite (sample Cos-37). (e) Photomicrograph of sample from underground level 10 (748139E, 2523400N at 2154 masl) showing hedenbergite retrograded to nontronite and replaced by chalcopyrite, and (f) back scattered electron image of stilpnomelane replacing chalcopyrite.

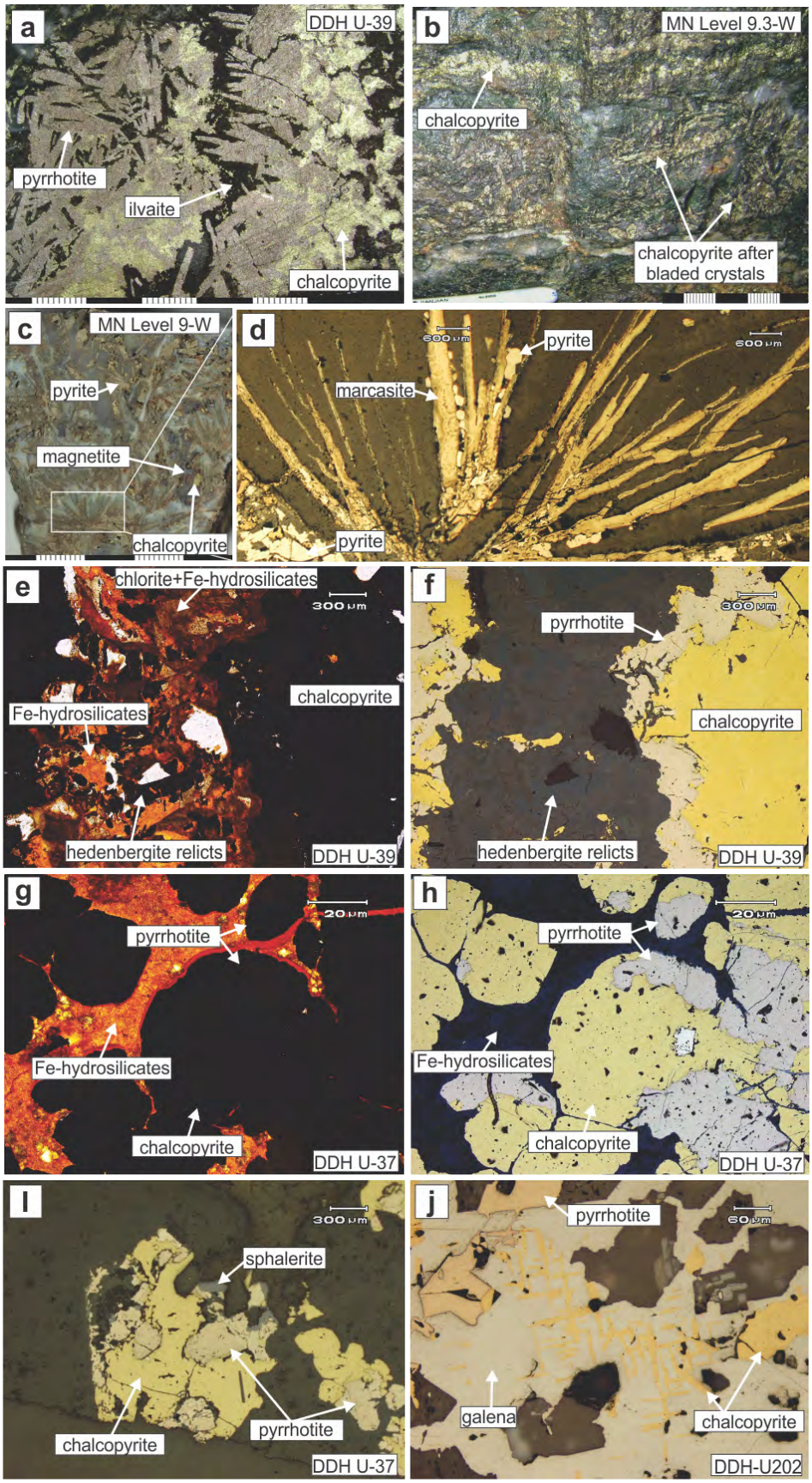
a
DDH U-39
pyrrhotite
ilvaite
chalcopyrite
b
MN Level 9.3-W
chalcopyrite
chalcopyrite after bladed crystals
c
MN Level 9-W
pyrite
magnetite
chalcopyrite
d
600 µm
pyrite
marcasite
pyrite
e
chlorite+Fe-hydrosilicates
300 µm
chalcopyrite
Fe-hydrosilicates
hedenbergite relicts
DDH U-39
f
300 µm
pyrrhotite
chalcopyrite
hedenbergite relicts
DDH U-39
g
20 µm
pyrrhotite
Fe-hydrosilicates
chalcopyrite
DDH U-37
h
20 µm
pyrrhotite
Fe-hydrosilicates
chalcopyrite
DDH U-37
I
300 µm
sphalerite
chalcopyrite
pyrrhotite
DDH U-37
j
pyrrhotite
60 µm
galena
chalcopyrite
DDH-U202

Figure 13. Photographs and reflected light photomicrographs of the Mala Noche skarn-type high Cu grade samples showing mineral associations and textures: (a) Sample from DDH U-39 (projected sample location E748097, N2523786 at 173.5 m) showing pyrrhotite replacing chalcopyrite and intergrown with ilvaite crystals. (b) Photo from underground wall level 9.3–W, showing semi-massive chalcopyrite replacing tabular bladed crystals (probably amphiboles). (c) Mineral association of pyrite, magnetite, and chalcopyrite in a groundmass of grey quartz (sample from underground level 9 west). (d) Close-up of c showing texture of marcasite and pyrite replacing radially elongated crystals of possible amphibole precursors. (e–f) Photomicrographs showing alteration and remnants of hedenbergite replaced by chalcopyrite and rimmed by pyrrhotite (e, transmitted light; f, reflected light; sample from DDH U-39; projected sample location E748097, N2523786 at 171 m). (g–h) Photomicrographs in transmitted and reflected light, respectively, showing isometric crystals (possible garnet) replaced by chalcopyrite and pyrrhotite surrounded by Fe-hydrosilcates (from DDH U-37; projected sample location E747779, N2523876 at 162 m). (i) Euhedral isometrically shaped crystal (probably garnet) replaced by chalcopyrite, pyrrhotite, and minor sphalerite (DDH U-37; projected sample location E747779, N2523876 at 162 m). (j) Sample from DDH U-202 (projected sample location E747827, N2523550) showing pyrrhotite and chalcopyrite replacing galena along cleavage planes.

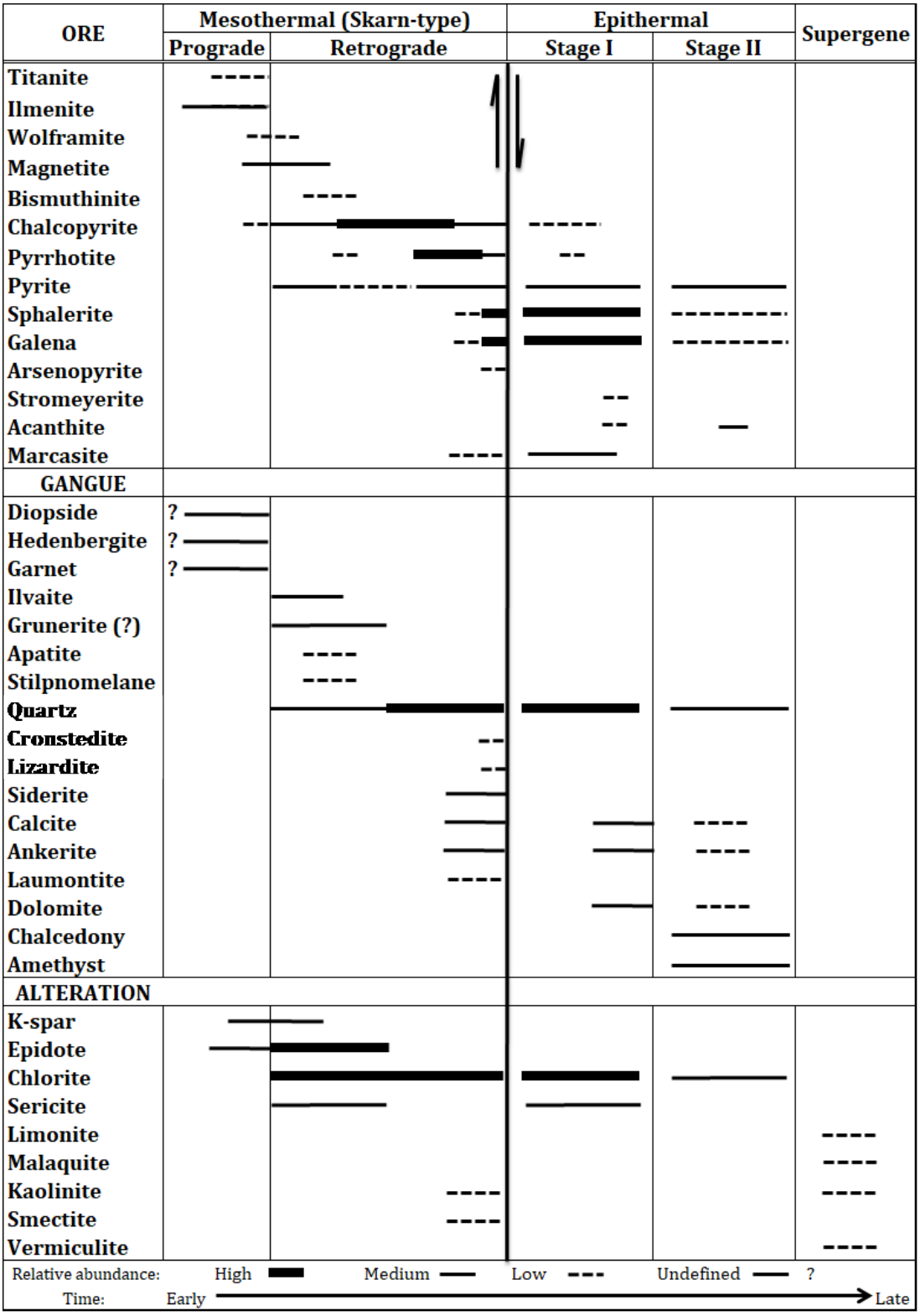

Figure 14. Mineral paragenesis of the Mala Noche skarn and intermediate-sulfidation epithermal mineralization.

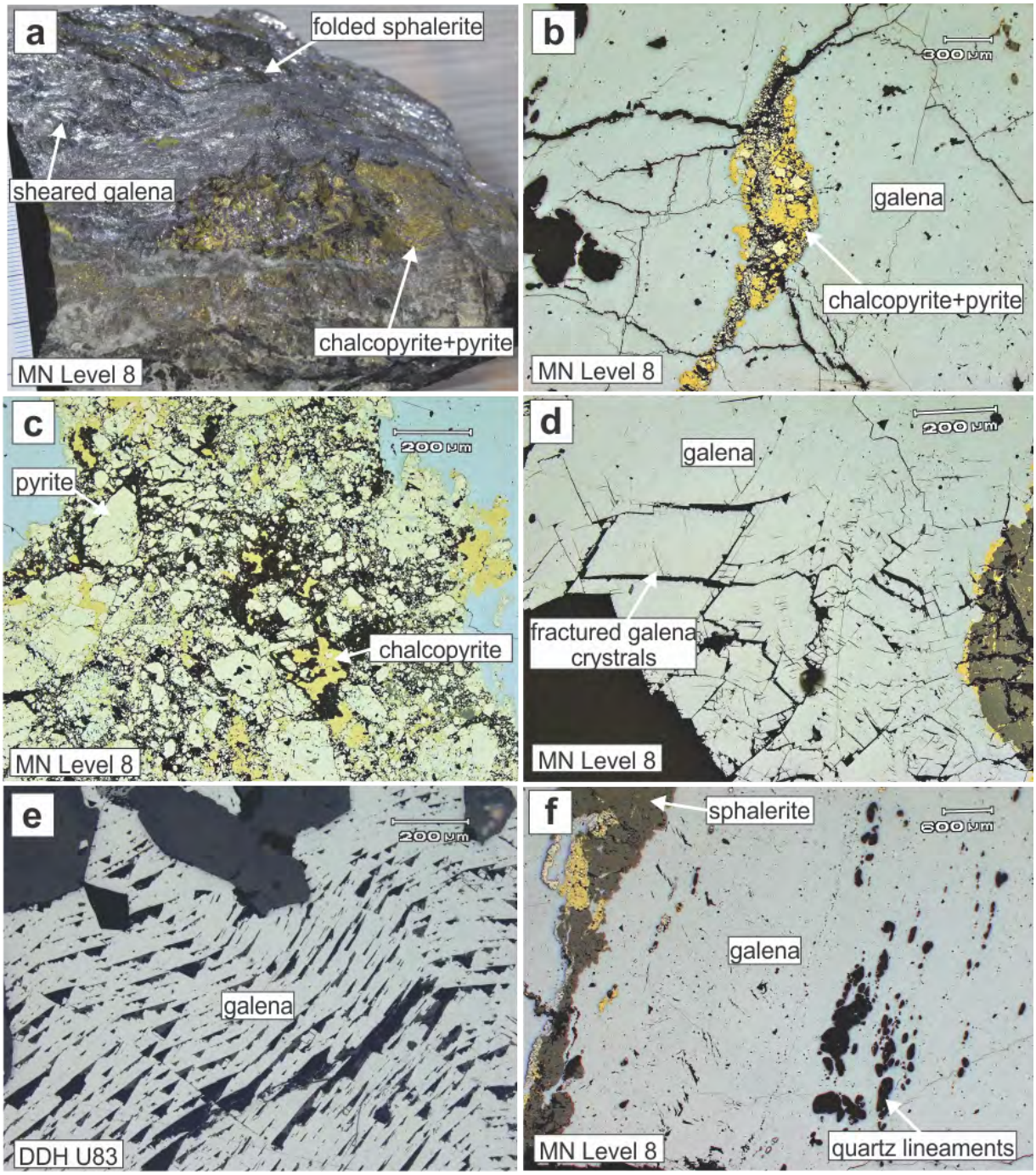

Figure 15. Mala Noche skarn-type mineralization showing post-mineral deformational textures in massive sulfides. (a) Hand specimen photograph of sheared galena with a folded band of sphalerite, and sigmoidal shaped lens of chalcopyrite and pyrite. Reflected light photomicrographs of: (b) sigmoidal shaped aggregate of chalcopyrite and pyrite; (c) cataclastic texture in pyrite and chalcopyrite; (d) fractured crystals of galena; (e) deformed triangular cleavage pits in galena; (f) lineaments of rounded quartz grains in galena that exhibit undulose extinction in transmitted light.

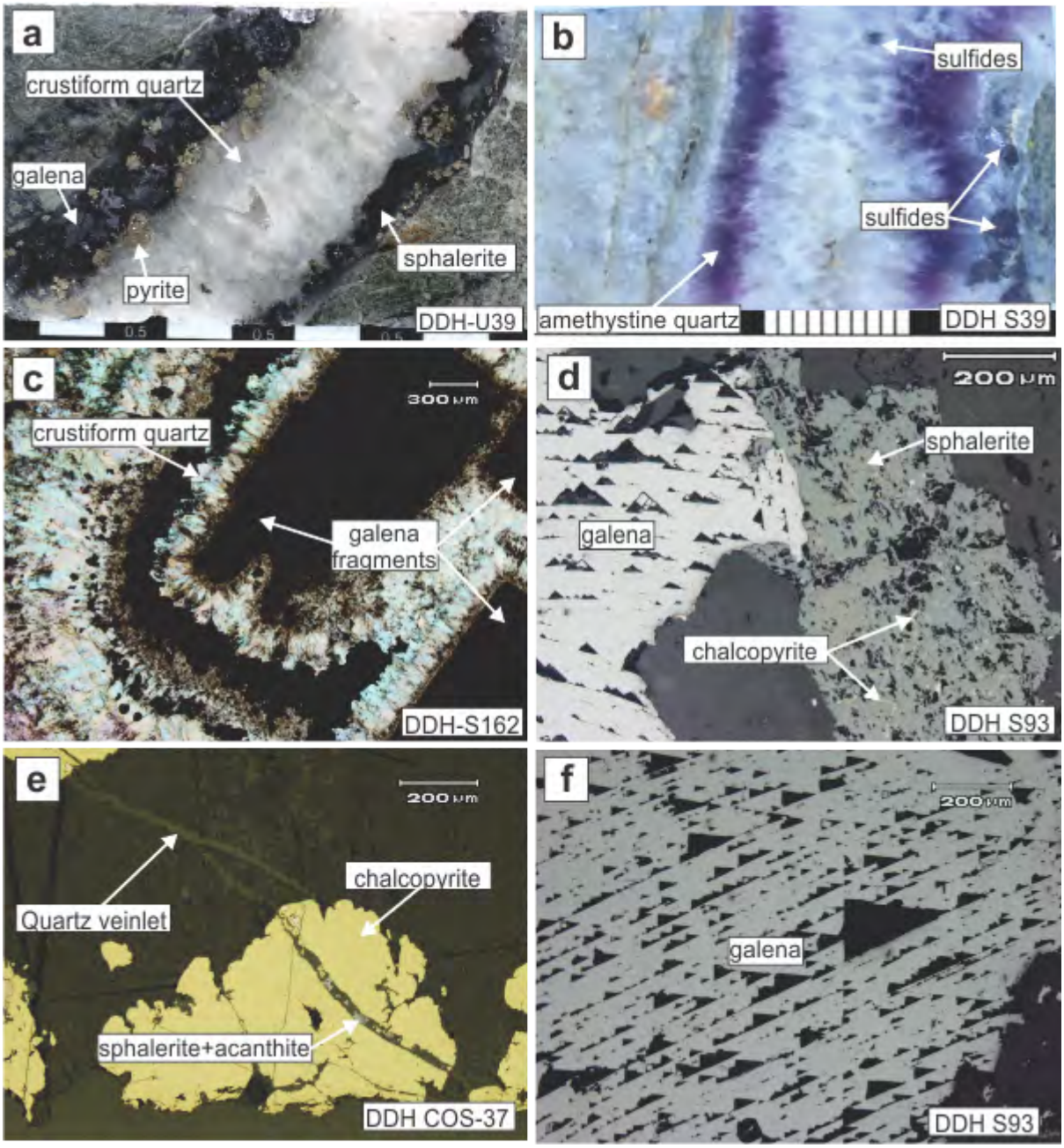

Figure 16. Photographs and photomicrographs of the Mala Noche Zn-Pb-Ag-rich intermediate-sulfidation epithermal mineralization showing textures and ore mineral associations: (a) Early sulfide-rich vein showing discontinuous bands of sphalerite, galena, pyrite, and crustiform quartz with vuggy cavities at the center. (b) Later sulfide-poor vein showing crustiform amethystine quartz. (c) Cockade texture formed by crustiform quartz that coats pre-existing fragments of galena. (d) Mineral association of galena, sphalerite, and blebs of chalcopyrite. (e) Micro-veinlet of quartz with sphalerite and acanthite crosscutting skarn-type stage chalcopyrite and associated alteration minerals. (f) Photomicrograph showing undeformed triangular cleavage pits in galena.

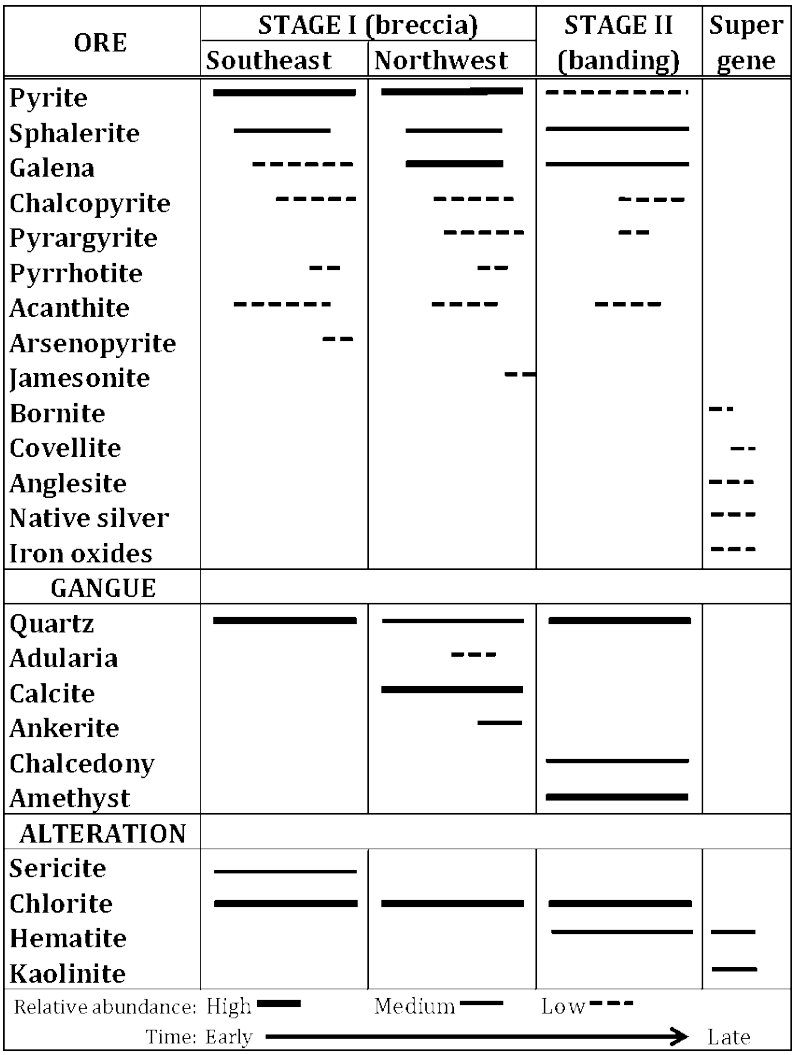

Figure 17. Mineral paragenesis of the Veta Grande Vein.

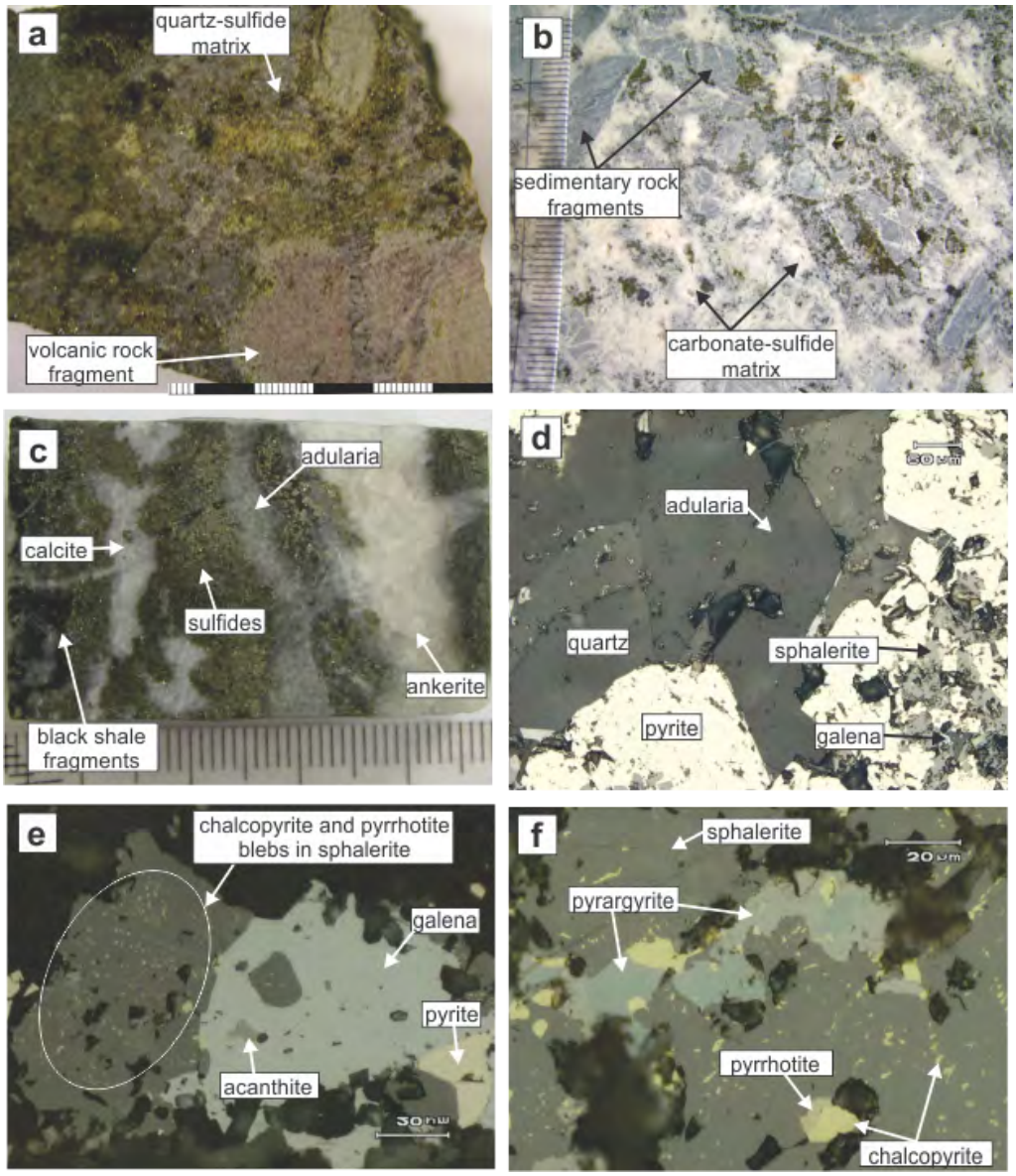

Figure 18. Hand samples and photomicrographs showing representative features of the Veta Grande stage I mineralization. (a) Southeast breccia showing fragments of volcanic rocks and a quartz-sulfide matrix (sample SA-1 from the El Refugio level; 752468E, 2526042N). (b) Northwest breccia showing fragments of sedimentary rocks and carbonate-sulfide matrix (sample OSDH6-S14 from drillhole 08VGX006; projected sample location 750090E, 2527129). (c) Vein sample showing the dated adularia associated with sulfides, ankerite, and calcite (sample VG1B-S8 from drillhole 08VGX001B; projected sample location 750738E, 2526639). (d) Reflected light microphotograph of sample shown in c showing euhedral quartz and adularia crystals associated with pyrite, sphalerite, and galena. (e, f) Reflected light microphotographs showing the association of Ag-bearing minerals with base-metal sulfides (e: sample OSDH1B-S4 from drillhole 08VGX001B projected sample location 750738E, 2526639; f: sample DP-04

from the Santa Rita level, 749815E, 2527748N).

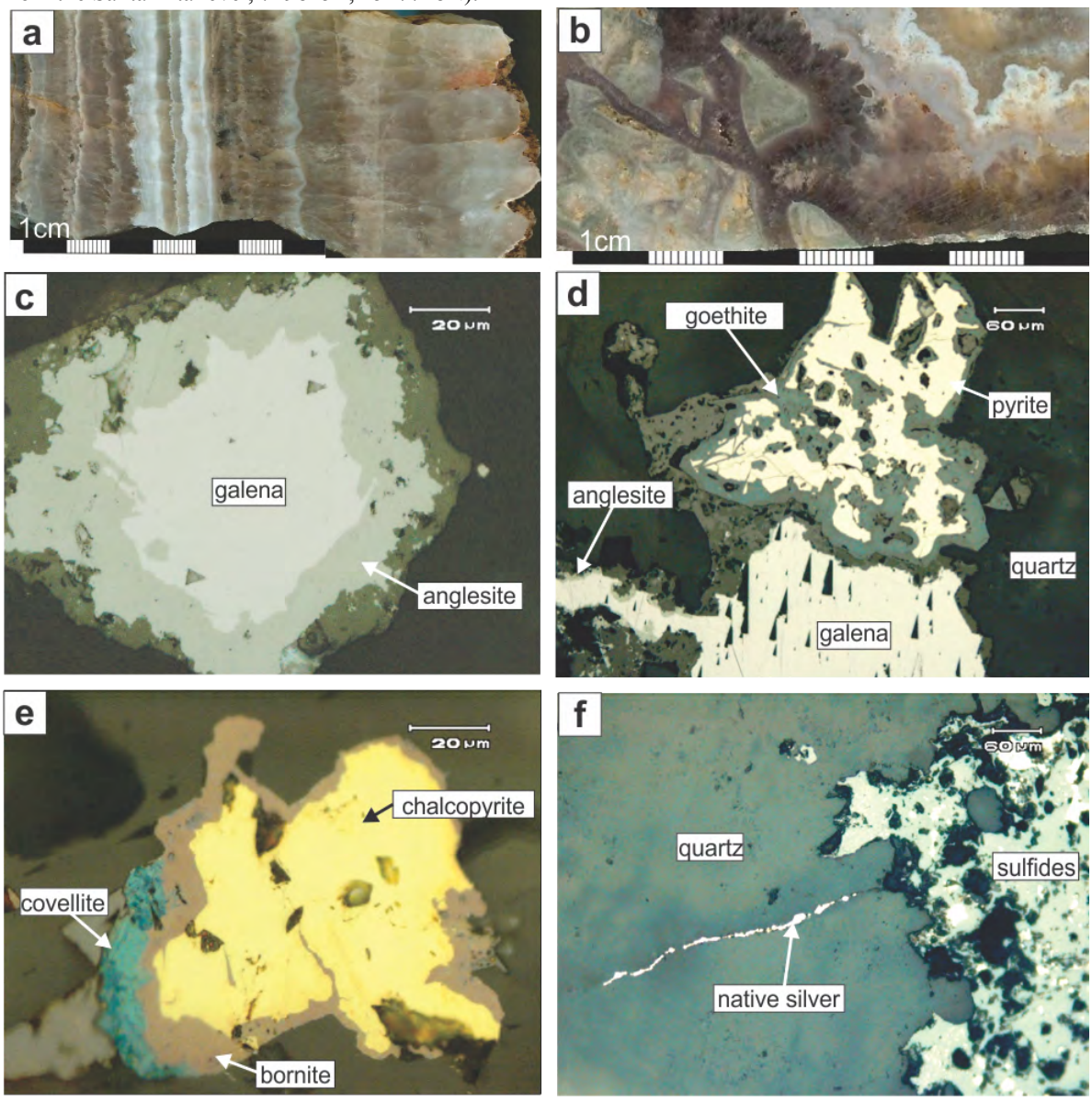

Figure 19. Hand samples and microphotographs showing representative features of the Veta Grande stage II mineralization. (a) Crustiform banding and prismatic crystalline quartz, amethyst, and chalcedony, with discontinuous bands containing sulfides and sulfosalts (dark bands; sample SA-3; surface sample location 751685E, 2526286N). (b) Stage II quartz enclosing fragments of stage I breccia (sample from drillhole SAD9536; projected sample location 751678E, 2526252N). Reflected light microphotographs: (c) supergene replacement of galena by anglesite; (d) supergene oxidation of pyrite to goethite associated with a halo of supergene anglesite replacing galena; (e) supergene replacement of chalcopyrite by bornite, and bornite by covellite; (f) native silver in a fracture associated with oxidized sulfides.

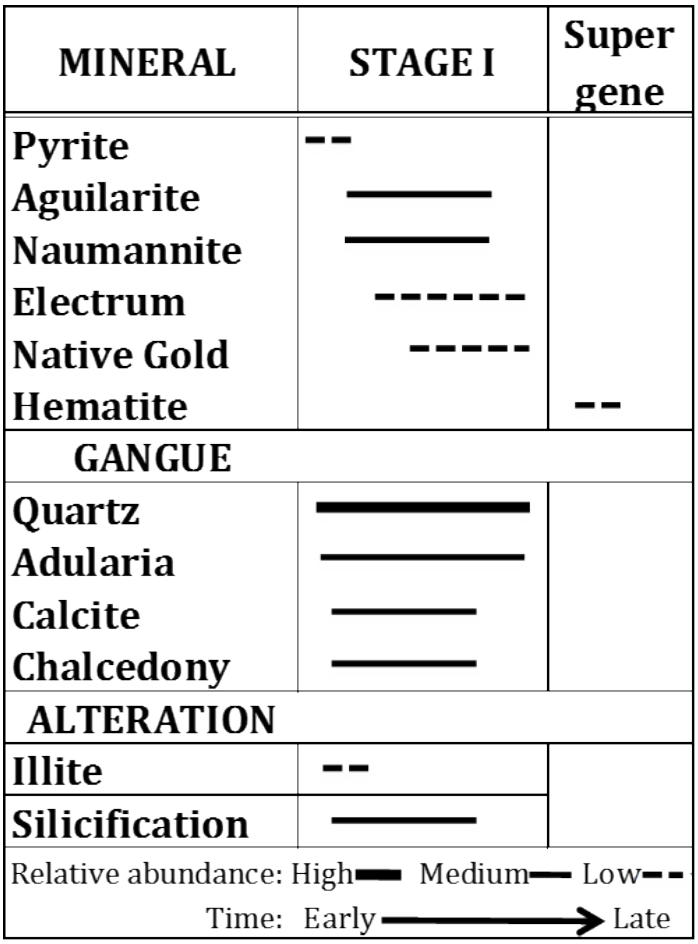

Figure 20. Mineral paragenesis of the El Compas Vein.

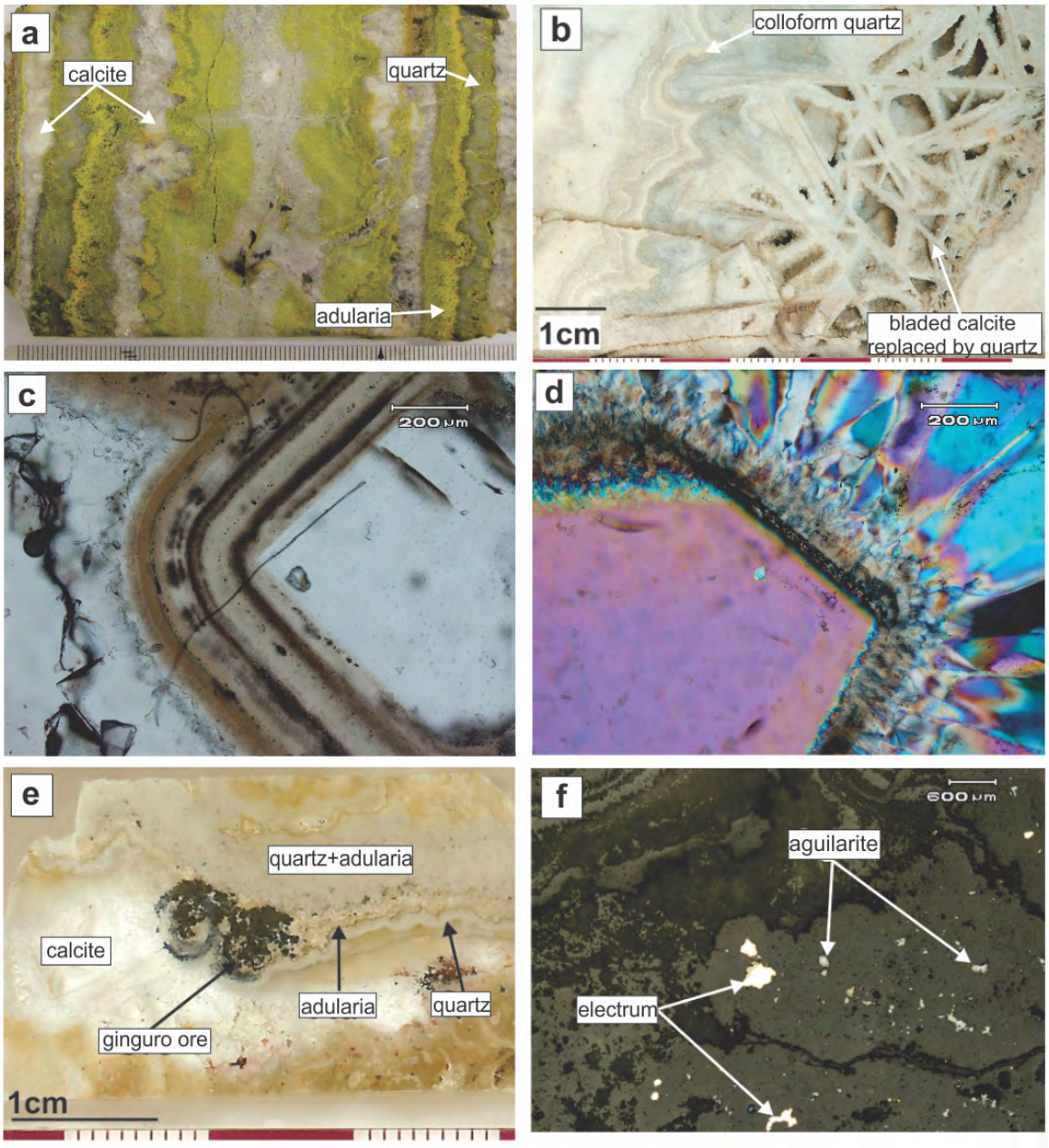

Figure 21. Hand samples and microphotographs showing representative features of the El Compas vein (El Orito System). (a) Hand sample stained with sodium cobaltinitrite showing alternating bands of greenish to white quartz, calcite, and adularia (stained yellow; sample from the El Compas underground mine, level 7). (b) Hand specimen showing bladed calcite texture with interstitial microcrystalline quartz and pinacoids of calcite (sample from the El Compas mine dump; 747259E, 2515568N). (c, d) Thick section of a sample from the El Compas underground mine stock pile showing flamboyant and plumose textures, in plane- and cross-polarized light. (e) Scanned thick section showing electrum, aguilarite, and naumannite related to bands of microcrystalline quartz and adularia (sample from drillhole 09COM043 at 63 m). (f) Close up of e in reflected light showing aguilarite and electrum grains set in a matrix of quartz and adularia.

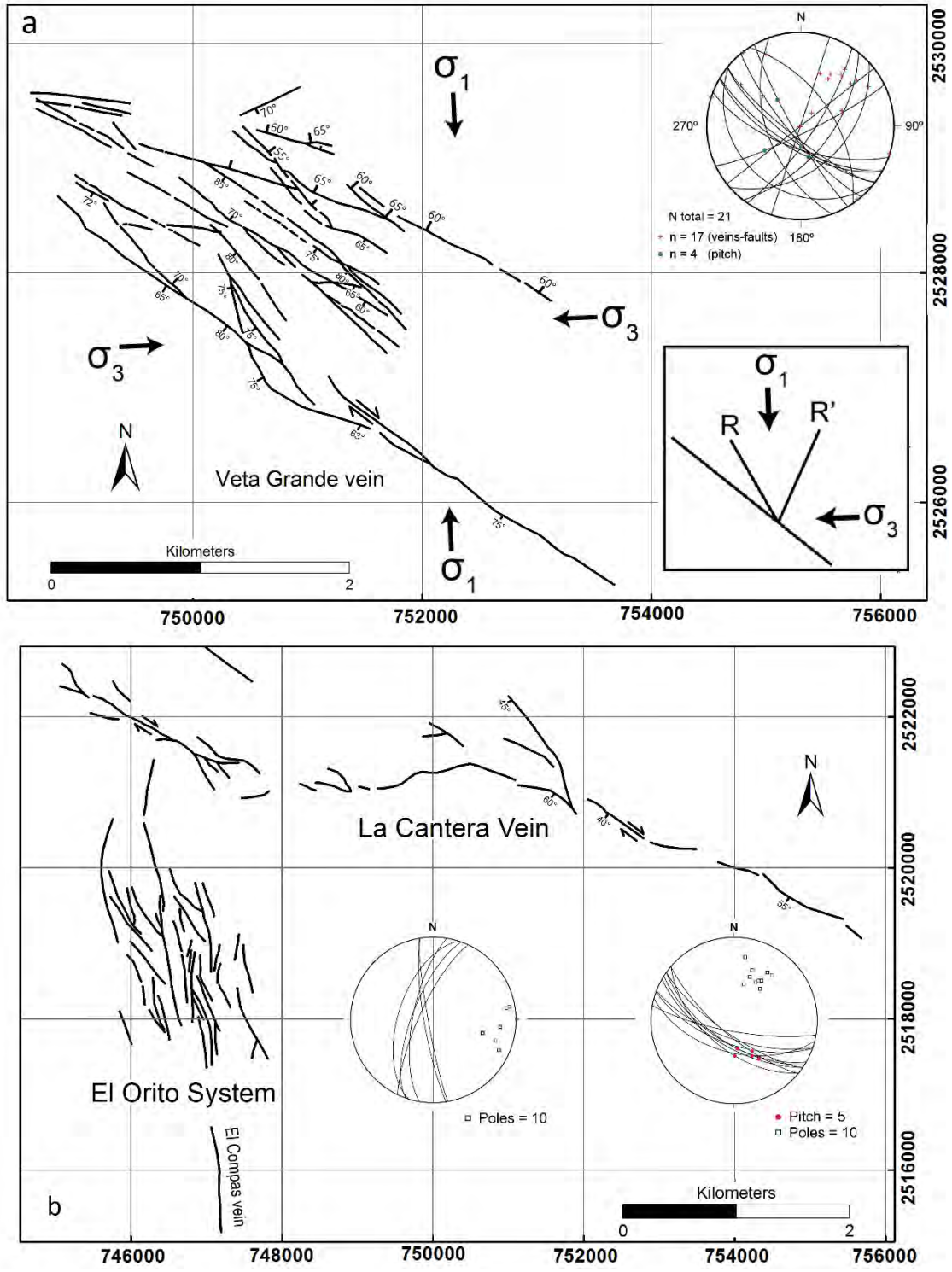

Figure 22. Structural maps of the (a) Veta Grande, and (b) La Cantera ENE-striking dextral strike-slip fault systems, and (b) El Orito N–S-striking normal fault system (modified from Perez-Martinez et al., 1961).

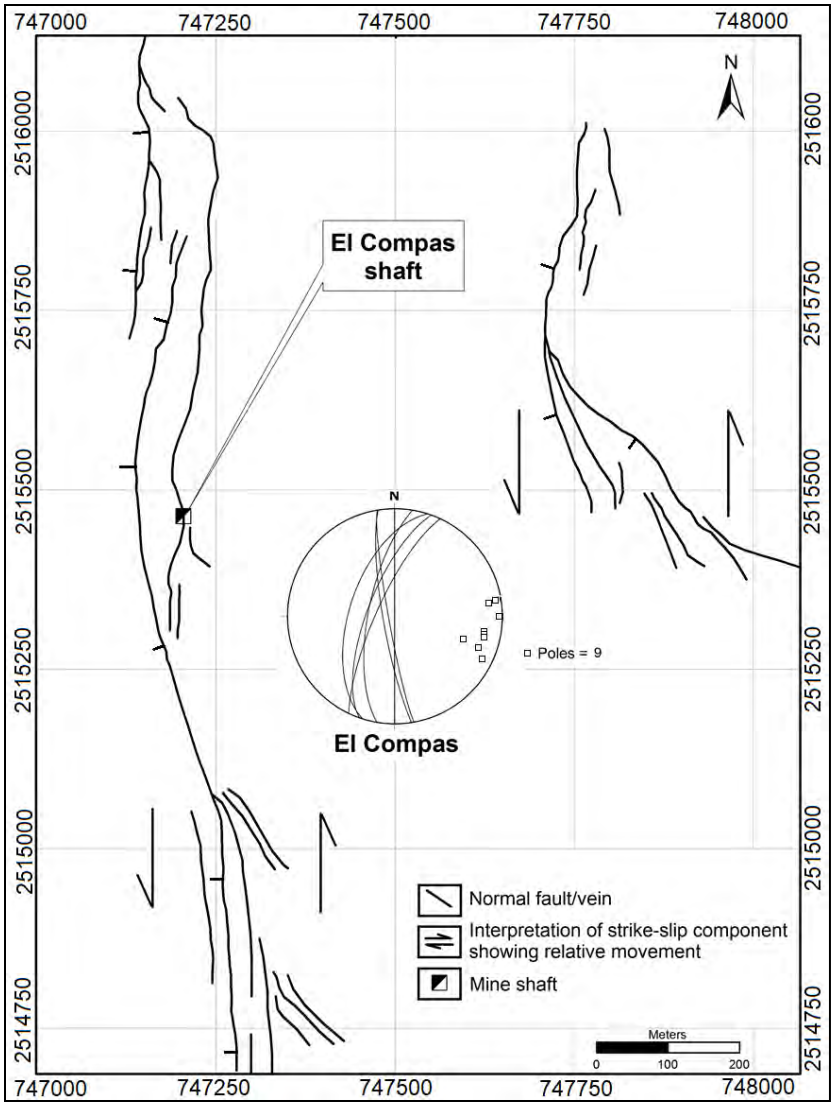

Figure 23. Surface map of the El Compas veins showing second-order NW-striking vein patterns.

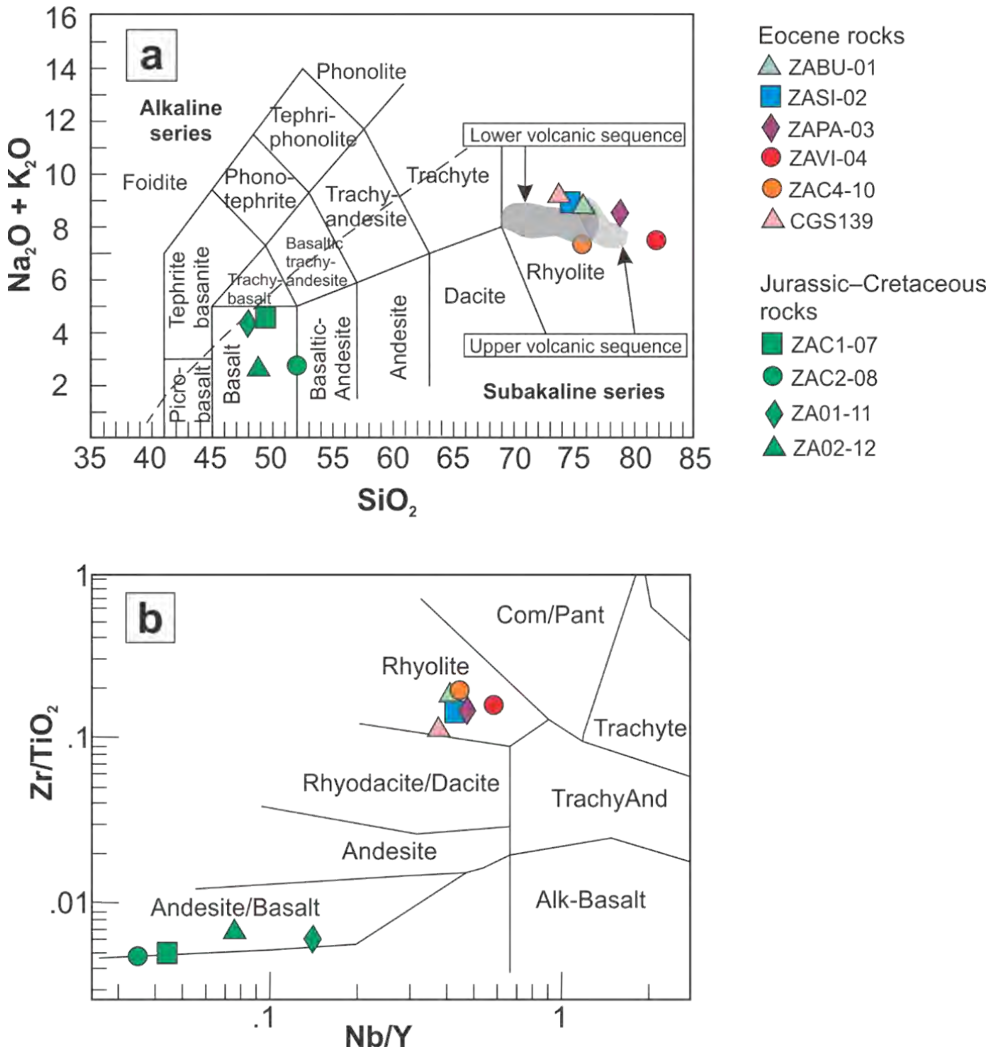

Figure 24. (a) Total alkali vs. silica diagram (LeBas et al., 1986); alkaline-subalkaline boundary from Irvine and Baragar (1971) showing the major element classification of the Jurassic–Cretaceous lava flows and Eocene volcanic and hypabyssal rocks from the Zacatecas district; and (b) Zr/TiO_2 vs. Nb/Y diagram (Winchester and Floyd 1977) showing their corresponding trace element classification.

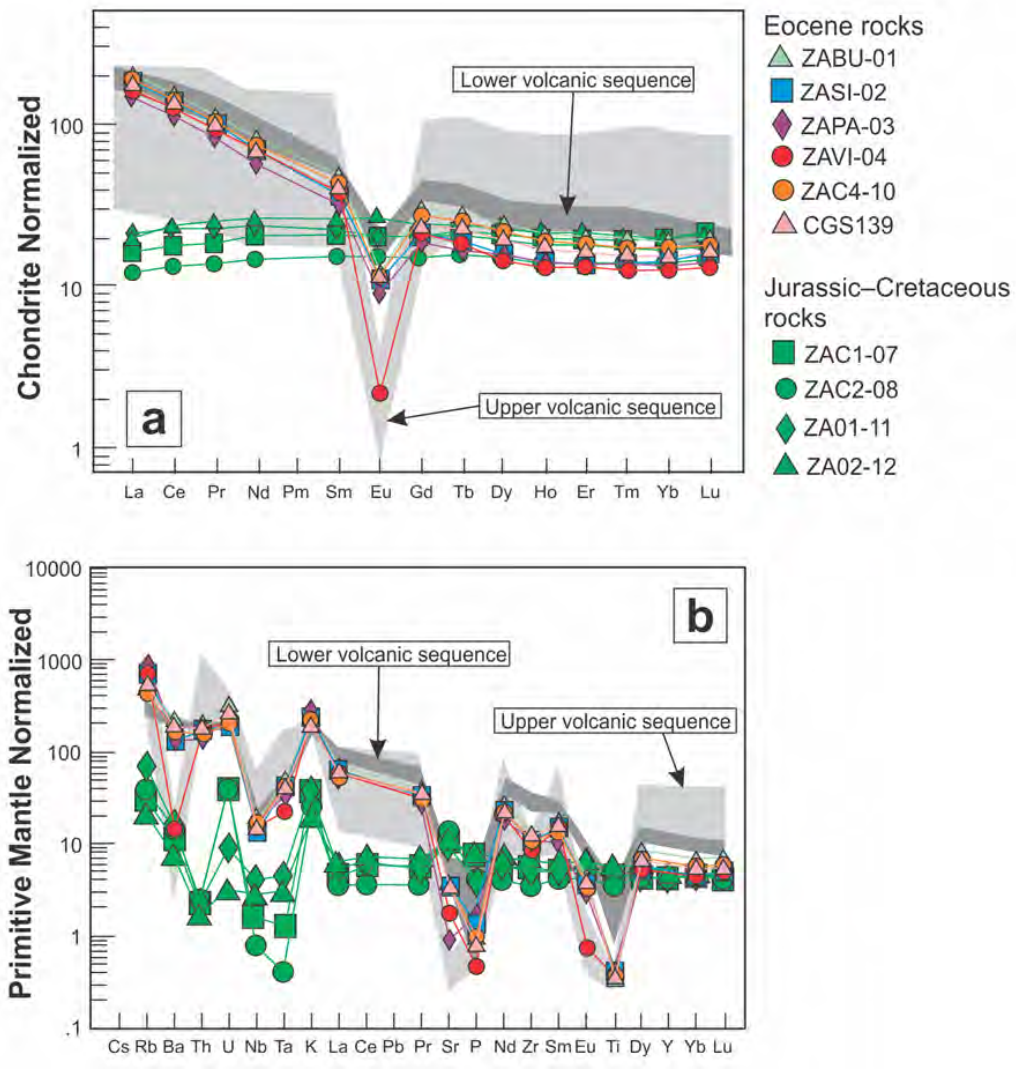

Figure 25. (a) Chondrite-normalized REE diagram, and (b) primitive mantle-normalized extended trace element diagram for samples from the Zacatecas district (normalization values of Sun and McDonough, 1989). The compositional ranges of the lower and upper volcanic sequences of the southern Mesa Central are shown in dark and light gray, respectively (data from Orozco-Esquivel et al., 2002).

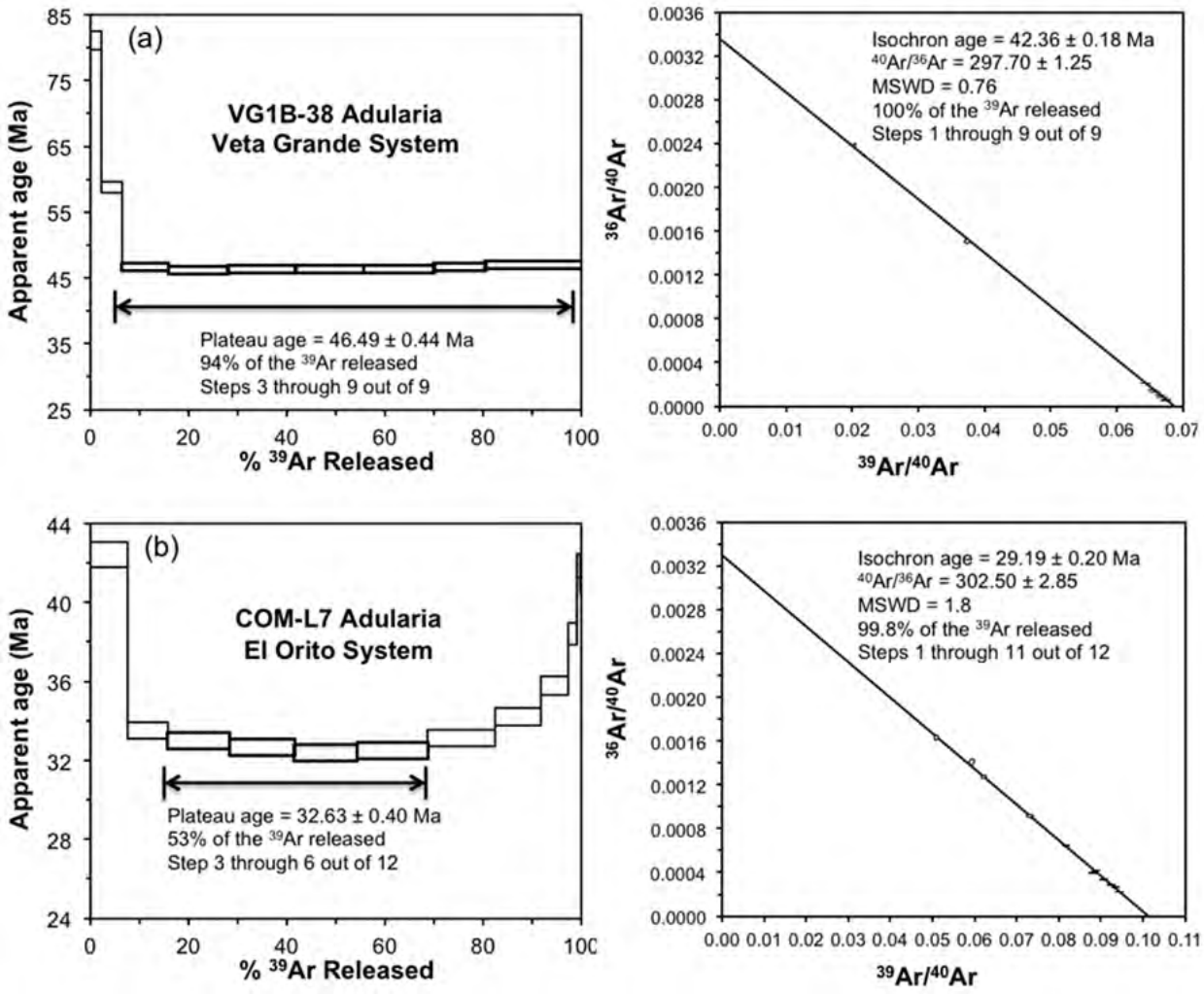

Figure 26. Apparent $^{40}Ar/^{39}Ar$ age spectra and inverse isochron diagrams for adularia samples from (a) the Veta Grande vein (VG1B-08), and (b) the El Compas vein (COM-L7). All errors are drawn at 1σ error, but calculated ages are reported to 2σ.

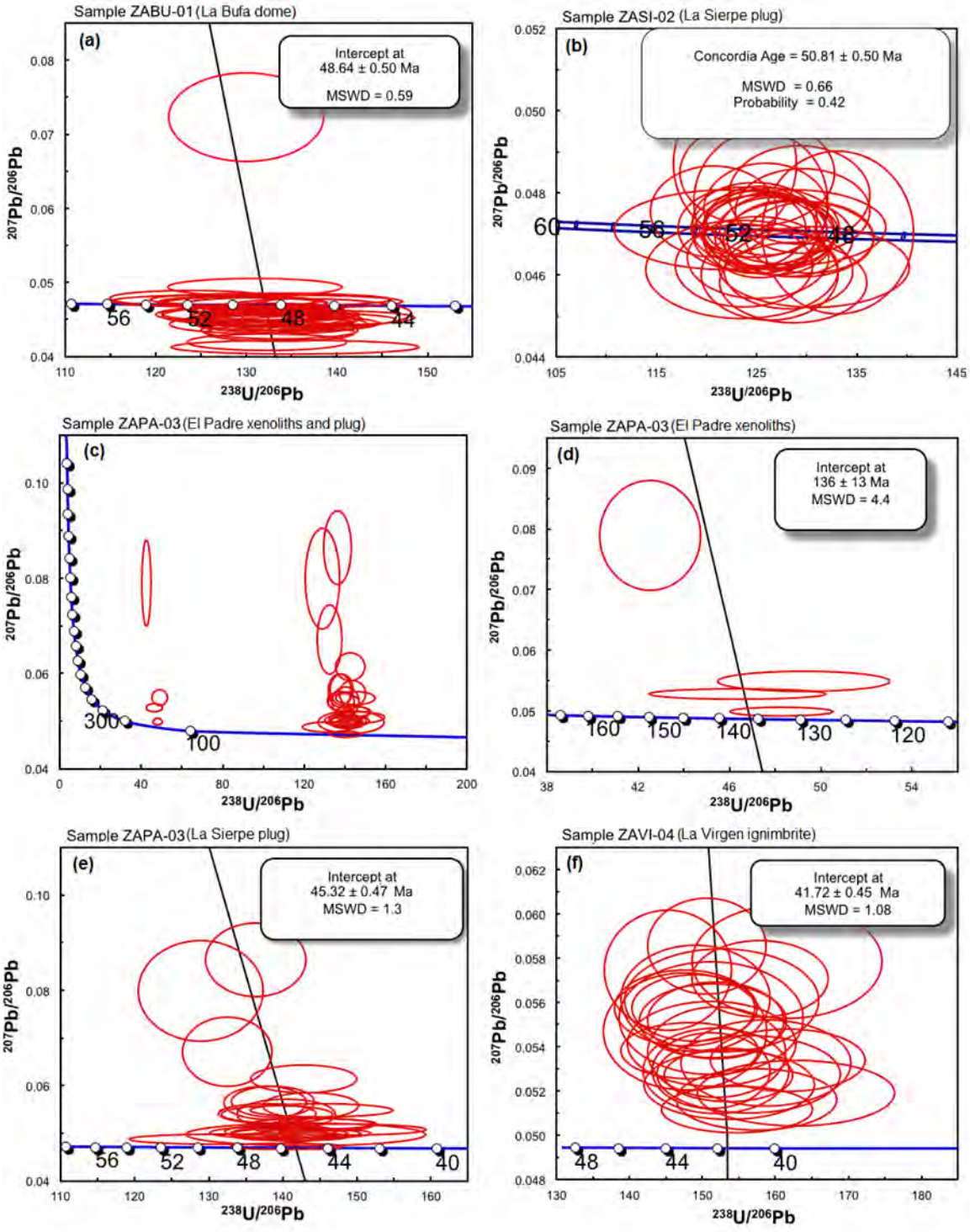
Sample ZABU-01 (La Bufa dome)
(a)
Intercept at
48.64 ± 0.50 Ma
MSWD = 0.59
Sample ZASI-02 (La Sierpe plug)
(b)
Concordia Age = 50.81 ± 0.50 Ma
MSWD = 0.66
Probability = 0.42
Sample ZAPA-03 (El Padre xenoliths and plug)
(c)
Sample ZAPA-03 (El Padre xenoliths)
(d)
Intercept at
136 ± 13 Ma
MSWD = 4.4
Sample ZAPA-03 (La Sierpe plug)
(e)
Intercept at
45.32 ± 0.47 Ma
MSWD = 1.3
Sample ZAVI-04 (La Virgen ignimbrite)
(f)
Intercept at
41.72 ± 0.45 Ma
MSWD = 1.08
207Pb/206Pb
238U/206Pb

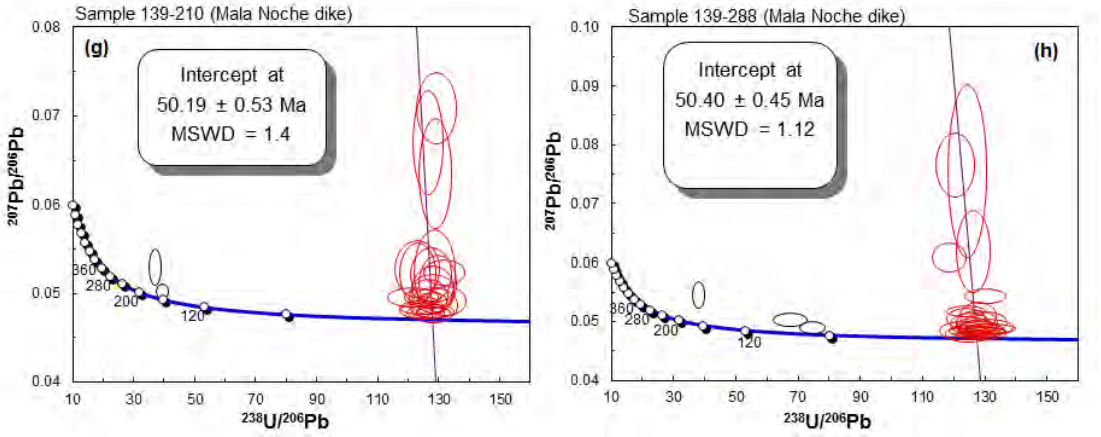

Figure 27. Tera-Wasserburg concordia diagrams for volcanic and hypabyssal rocks of the Zacatecas district. See text for details.

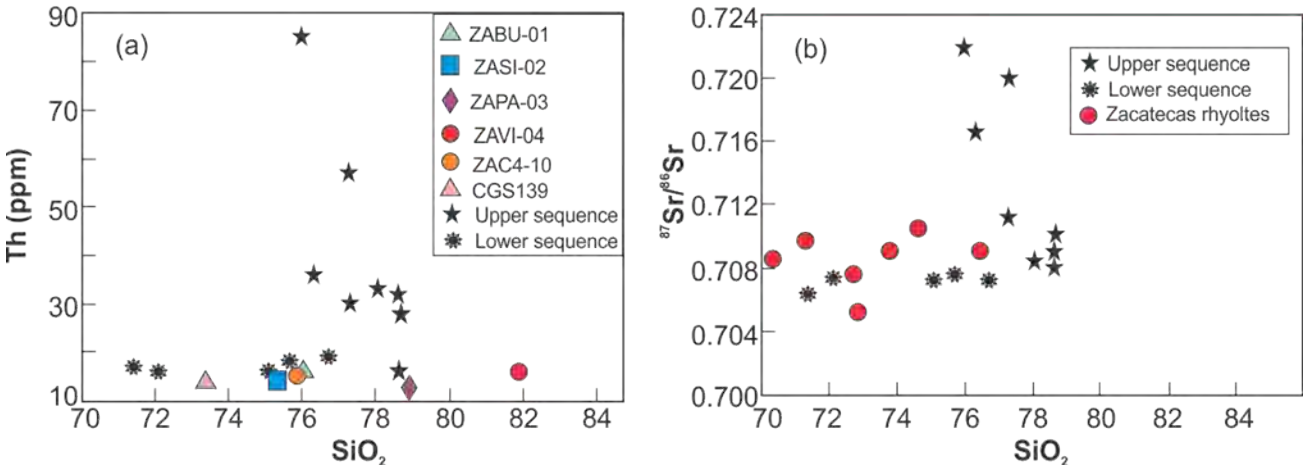

Figure 28. (a) Plot of Th versus SiO_2 for Eocene volcanic and hypabyssal rocks from the Zacatecas district and the southern Mesa Central (upper and lower volcanic sequences; Orozco-Esquivel et al., 2002). (b) Initial strontium isotope ratios versus silica contents for the Zacatecas district felsic volcanic and subvolcanic intrusive rocks (Verma, 1984) and for the southern Mesa Central (upper and lower sequences; Orozco-Esquivel et al., 2002).

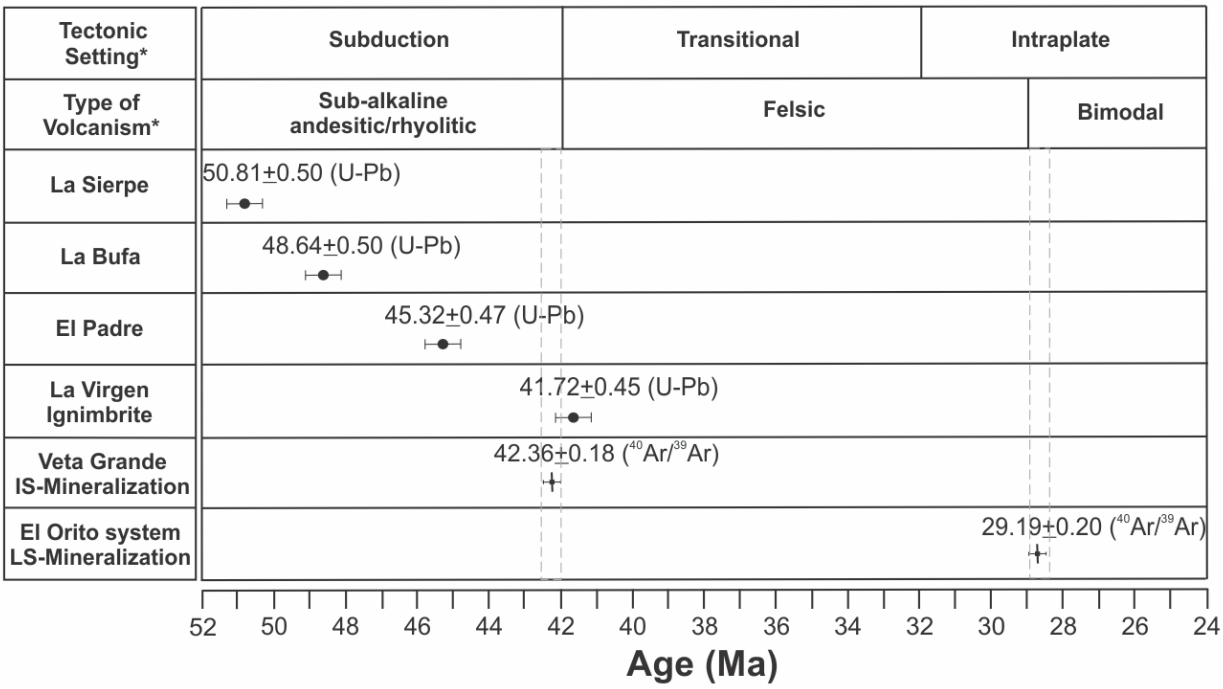

Figure 29. Summary of U-Pb and ^{39}Ar/^{40}Ar geochronology from this study; tectonic setting and type of volcanism from Tristan-Gonzalez et al. (2009).

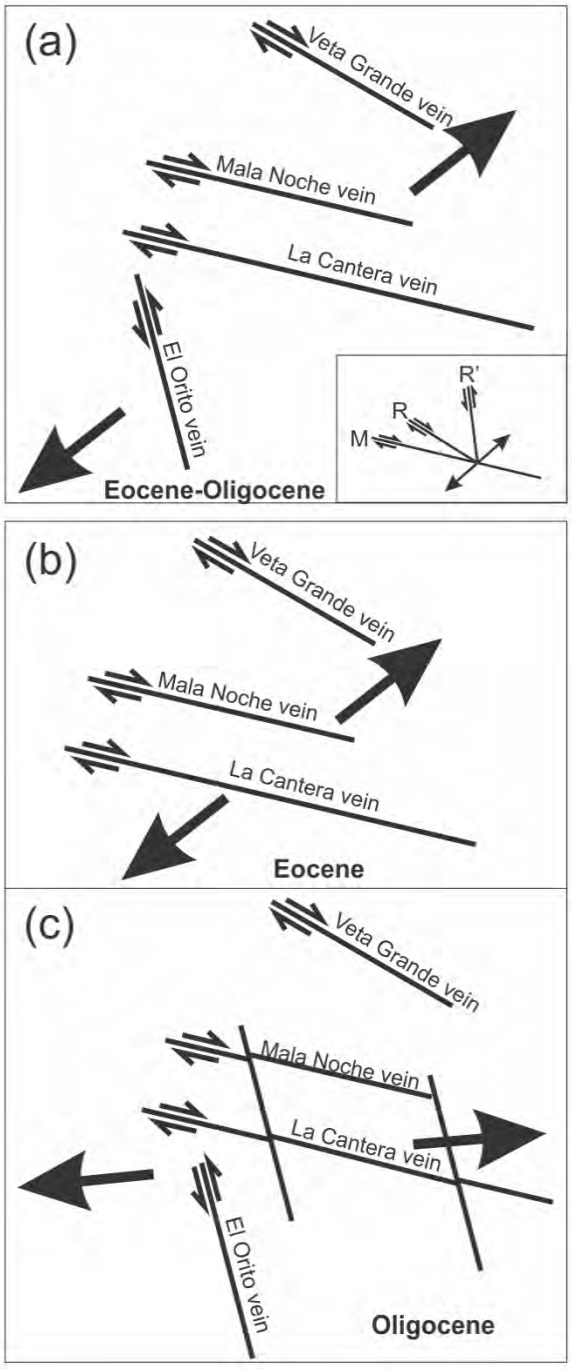

Figure 30. Possible models of fault kinematics and stress field for the Zacatecas fault systems. (a) Transtensional stress regime prevalent in the Eocene-Oligocene, proposed by Nelson (2005): here, the El Orito vein is interpreted to represent a secondary fault (R') related to the La Cantera main fault. The inset shows a Riedel model for a dextral strike-slip system (Petit, 1987). Model proposed here and by Tristan-Gonzalez et al. (2012) for a transtensional stress regime in the Eocene (b), overprinted by Basin and Range extension in the Oligocene (c). Abbreviations: M = main fault plane; R = synthetic secondary shears; R' = antithetic secondary shears.

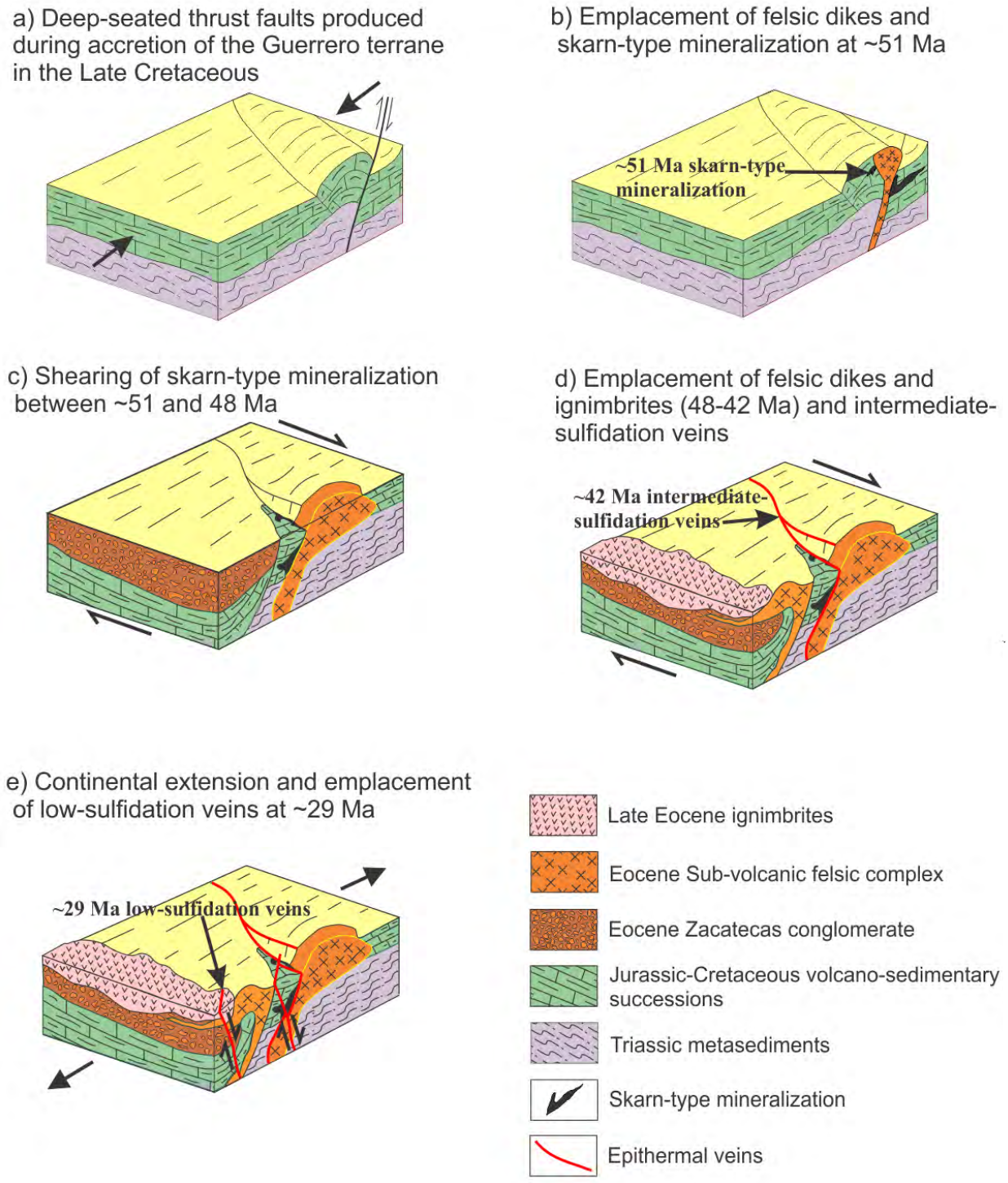

Figure 31. Cartoons showing a model for the multiple mineralization events in the Zacatecas district (see text for explanation).

1. Analytical Methods and Samples

Results of electron microprobe analyses, wole-rock geochemistry, $^{40}Ar/^{39}Ar$, U-Pb, and locations and descriptions of samples analyzed for geochemistry and geochronology are listed in Appendix A–E.

1.1 Electron Microprobe Analyses

Quantitative analyses of sulfide and selenide minerals were obtained by wavelength dispersive spectrometry (WDS) using a JEOL 8900 electron microprobe at the University of Alberta. Sulfide minerals from the Mala Noche and Veta Grande veins were analyzed for S, As, Ag, Au, W, Pb, Bi, Fe, Sb, Cu, and Zn, and the El Compas vein selenides were analyzed for S, Ag, Au, Br, Se, Cl, and Hg. The instrument was operated at an accelerating voltage of 20 kV and current of 20 nA, with peak and background count times at 20 and 10 s, respectively. A CAMECA-SX-100 electron microprobe was used under energy dispersive spectroscopy (EDS) mode to aid in the identification of silicate and oxide minerals and to obtain images under back-scattered electron (BSE) mode. The operating conditions of the instrument were an accelerating voltage of 15 kV and a current of 20 nA.

1.2 Whole Rock Geochemistry

Major- and trace-element compositions of eleven samples of volcanic host rock were analyzed at Actlabs Laboratories in Ontario, Canada. Four samples of basaltic lava flows are from the Jurassic-Cretaceous volcano-sedimentary succession, and the other six are from the Eocene subvolcanic and volcanic rocks. The analytical package used was 4E-research, which includes a combination of inductively coupled plasma (ICP), inductively coupled plasma emission mass spectrometry (ICP-MS), and instrumental neutron activation analysis (INAA) methods. Detection limits for each element along with full analyses are listed in Appendix C. Replicate analyses of certificated standards indicate accuracy to generally within 5 relative percent for major elements and 10 relative percent for trace elements.

1.3 $^{40}Ar/^{39}Ar$ Geochronology

Adularia was identified with the aid of petrography and sodium cobaltinitrite staining of drill core and underground hand samples. One sample was selected from the low-sulfidation El Orito system (COM-L7) and another from the stage I intermediate-sulfidation Veta Grande system (VG1B-S8).

Adularia is rare at Veta Grande, and where present occurs as small rhombohedral crystals up to 100 μm long intergrown with quartz and sulfides (Fig. 18c–d). To separate adularia from this sample, a roughly defined band with a high concentration of adularia mixed with sulfides was sawn off with a fine diamond saw, and then

crushed and sieved to select the fraction between 85 and 100 μm. Sulfides were removed using heavy liquids (bromoform), and the sample was analyzed by XRD to check purity. Small amounts of quartz were detected, but it was too finely intergrown with the adularia to be removed without further crushing.

The sample from the El Orito system was collected from Level 7 of the El Compas mine. In this system, adularia occurs as fine-grained (<80 μm) euhedral crystals intergrown with microcrystalline quartz and calcite in banded veins (Fig. 21a). A band with the highest proportion of adularia (~90%) was carefully separated with a fine diamond saw, and crushed to hand pick aggregates of adularia in a matrix of quartz. These aggregates were lightly crushed again and sieved to collect the fraction between 85 and 100μm. This fraction was cleaned ultrasonically and analyzed by XRD to determine purity. Small amounts of quartz and calcite were detected by XRD in addition to adularia, but it was decided not to attempt further purification because of the risk of fragmenting individual adularia crystals (which can cause mechanical homogenization of the K-Ar distribution in the sample; Richards and Noble 1998).

The two adularia samples were sent to the Nevada Isotope Geochronology Laboratory at the University of Las Vegas for Ar isotopic analysis. The samples were wrapped in aluminum foil and loaded together with neutron fluence and neutron-induced argon interference monitors in sealed silica tubes. Loaded tubes were packed in an aluminum container and sent for irradiation at the U.S. Geological Survey TRIGA Reactor, Denver, CO. Neutron fluence was monitored using the Fish Canyon Tuff sanidine standard (28.02 Ma; Renne et al., 1988). Neutron induced argon interference from K and Ca was corrected using correction factors determined by repeated analysis of synthetic K-glass and optical grade CaF_2 fragments (($^{40}Ar/^{39}Ar)_K$ = 1.74 (± 67.07%) x 10^{-2}, ($^{36}Ar/^{37}Ar)_{Ca}$ = 2.16 (± 8.78%) x 10^{-4}, and ($^{39}Ar/^{37}Ar)_{Ca}$ = 6.70 (± 1.60%) x 10^{-4}). After irradiation the samples were fused under a 20 W CO_2 beam laser using the step-heating method. The $^{40}Ar/^{39}Ar$ ratios of the gas released from each step were measured using a MAP 215-50 mass spectrometer. Atmospheric argon aliquots were analyzed repeatedly to monitor mass spectrometer discrimination and sensitivity. Measured $^{40}Ar/^{36}Ar$ ratios were 279.72 ± 0.43% during this work, thus a discrimination correction of 1.0565 (4 AMU) was applied to measured isotope ratios. Final data reduction and age calculations were performed using LabSPEC software.

1.4 U/Pb Geochronology

Six samples of Eocene volcanic and subvolcanic rocks collected from surface outcrops and drill-core were dated by the U-Pb zircon method. Zircon crystals were separated at the University of Alberta using standard crushing and mineral separation techniques: approximately 10 kg of each sample was pulverized, and zircons were separated using a Wilfley table, a Frantz isodynamic separator, and heavy liquids (methylene iodide). A population of about 100 zircons was selected by hand under a binocular microscope based on size, morphology, and optical clarity. Zircons are euhedral with prismatic or elongated habit and well-developed

growth zoning, and range in size between 30 and 150 μm in the longest dimension. These characteristics are typical of magmatic zircons (Fig. 1; Shore and Fowler, 1996). Zircons that show textural evidence of inherited cores were avoided. The selected zircons were mounted in epoxy resin for analysis using laser ablation multicollector inductively coupled plasma mass spectrometry (LA-MC-ICP-MS) at the University of Alberta Radiogenic Isotope Facility. The laser spot used was 30 μm, and the analytical procedure is described in detail by Simonetti et al. (2005). Descriptions of the samples and their locations are provided in Apendix B and summarized below.

Sample ZABU-01 was taken from the top of the La Bufa rhyolite dome, avoiding xenoliths and obvious alteration; surface weathering rinds were removed in the field. This sample represents the youngest volcanic flow from this dome.

Sample ZASI-02 is from the rhyolitic La Sierpe plug. It was collected from drill core (hole S38) at a depth of ~750 m. The hole was drilled vertically down a feeder zone of the rhyolitic La Sierpe plug, which is inferred from the fact that the drill hole intersects rhyolite at the top, bottom, and intermittently along the length of the hole, with vertical flow-banding textures and subvertical contacts with the metasedimentary country rock. The sample was taken from a central section of one interval of rhyolite, avoiding contacts with the metasedimentary rock and flow-banded zones containing xenoliths.

Sample ZAPA-03 was taken from an outcrop of the El Padre rhyolitic plug. The sample has a porphyritic texture with laminar fabric surrounding sparse xenoliths of andesitic rock. Surface weathering rinds were removed in the field and xenoliths were avoided as far as possible.

Sample ZAVI-04 was taken from the upper level of the La Virgen ignimbrite, where the rock is crystal-rich and the number of xenoliths decreases. The sample was taken on the La Virgen plateau away from obvious hydrothermal alteration haloes or weathering.

Samples CGS139-210 and CGS139-288 are from rhyolite dikes that run parallel to the Mala Noche vein, and are spatially associated with Cu-rich mineralization. The samples were taken from drillhole CG-08-139 at 210.30–211.3 m, and 288.5–291.10 m depth, respectively. They consist of pale gray to whitish rhyolite with scarce phenocrysts of sericitized plagioclase set in a cryptocrystalline silica groundmass. Both samples were taken away from contacts with the metasedimentary rock and avoiding xenoliths.

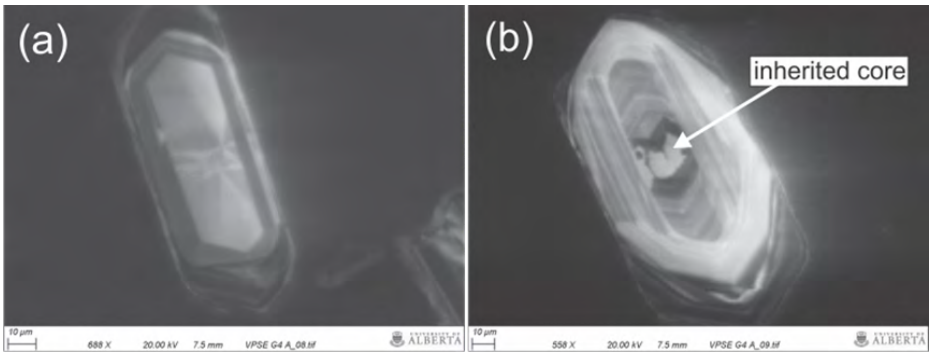

Figure 1. Cathodoluminescence images of representative zircons from sample CGS139 showing (a) prismatic habit and growth zoning typical of magmatic zircons, and (b) inherited core.

Appendix A: Microprobe Data

Veta Grande

Sample	Mineral	S	As	Ag	Au	W	Pb	Bi	Fe	Sb	Cu	Zn	Total
		W%	W%	W%	W%	W%	W%	W%	W%	W%	W%	W%	W%
SCDH36-S8	Bornite	25.4	0.1	0.7	0.0	n.a	0.0	0.1	10.5	0.0	61.2	0.0	98.1
OSDH1B-S8	Galena	12.6	0.0	0.0	0.0	n.a	80.0	0.3	0.7	0.0	0.0	0.0	93.6
OSDH6-S9	Jamesonite	20.7	0.1	0.0	0.0	n.a	38.1	0.0	2.8	35.8	0.0	0.0	97.5
OSDH6-S9	Galena	13.0	0.1	0.0	0.0	n.a	80.2	0.4	0.0	0.1	0.1	0.0	93.9
OSDH6-S9	Chalcopyrite	32.4	0.1	0.2	0.0	n.a	0.0	0.1	25.4	4.4	29.8	0.0	92.3
OSDH6-S9	Jamesonite	21.1	0.1	0.0	0.0	n.a	38.8	0.2	2.5	35.6	0.0	0.0	98.4
OSDH6-S2	Acanthite	14.2	0.1	81.7	0.1	n.a	0.0	0.0	0.0	0.0	0.1	0.0	96.2
OSDH6-S2	Chalcopyrite	34.0	0.1	0.4	0.0	n.a	0.0	0.1	29.0	0.3	33.6	0.0	97.5
OSDH6-S2	Acanthite	16.5	0.0	79.2	0.0	n.a	0.0	0.1	0.1	0.0	0.7	0.0	96.7
OSDH6-S2	Chalcopyrite	34.5	0.0	0.1	0.0	n.a	0.0	0.1	29.9	0.0	34.0	0.0	98.4
DP-04	Pyrargyrite	17.3	0.2	58.5	0.0	n.a	0.0	0.0	0.3	21.5	0.9	2.8	101.5
DP-04	Pyrrhotite	38.8	0.0	0.0	0.0	n.a	0.0	0.2	58.2	0.0	0.1	2.4	99.7
DP-04	Pyrite	52.6	0.1	0.0	0.0	n.a	0.0	0.2	45.8	0.0	0.0	2.1	100.8
DP-04	Pyrargyrite	17.2	0.2	58.5	0.0	n.a	0.0	0.1	0.4	22.1	0.9	2.8	102.0
DP-04	Sphalerite	33.6	0.0	0.0	0.0	n.a	0.0	0.1	6.4	0.0	0.0	58.8	99.0
TVG	Acanthite	13.0	0.1	73.8	0.2	n.a	0.0	0.0	0.0	0.0	0.2	0.1	87.3
TVG	Anglesite	6.8	0.0	0.0	0.0	n.a	63.1	0.2	0.0	0.0	0.0	0.0	70.1
TVG	Galena	13.2	0.0	0.0	0.0	n.a	82.6	0.0	0.0	0.1	0.0	0.0	96.0
TVG	Acanthite	11.1	0.2	70.6	0.3	n.a	0.0	0.0	0.0	0.0	0.2	0.3	82.6
TVG	Acanthite	13.6	0.0	80.8	0.1	n.a	0.0	0.1	0.0	0.0	0.3	0.0	94.9
TVG	Acanthite	13.9	0.1	77.9	0.1	n.a	0.0	0.0	0.0	0.0	0.3	0.2	92.4

Mala Noche

Sample	Mineral	S	As	Ag	Au	W	Pb	Bi	Fe	Sb	Cu	Zn	Total
		W%	W%	W%	W%	W%	W%	W%	W%	W%	W%	W%	W%
MW9-W-4-2	Sphalerite	34.2	0.0	0.0	n.a	0.0	0.0	0.1	12.5	0.0	0.0	53.0	99.8
MW9-W-4-3	Sphalerite	34.2	0.0	1.5	n.a	0.0	0.0	0.1	12.4	0.0	0.0	53.1	101.3
MW9-W-4-4	Chalcopyrite	34.8	0.0	0.0	n.a	0.0	0.0	0.0	36.7	0.0	29.2	0.1	100.9
MW9-W-1c-1	Chalcopyrite	34.7	0.0	0.0	n.a	0.0	0.0	0.0	36.4	0.0	29.3	0.2	100.7
MW9-W-1c-2	Wolframite	0.0	0.0	7.3	n.a	57.4	0.0	0.1	21.4	0.0	0.0	0.0	86.2
MW9-W-1b-1	Wolframite	0.0	0.0	11.2	n.a	58.6	0.0	0.1	21.3	0.0	0.0	0.0	91.3
MW9-W-1b-2	Pyrite	53.2	0.0	0.0	n.a	0.0	0.0	0.0	45.8	0.0	0.4	0.1	99.5
MW9-W-1a-1	Chalcopyrite	34.5	0.0	0.0	n.a	0.1	0.0	0.0	36.6	0.0	29.4	0.0	100.6
MW9-W-1a-2	Chalcopyrite	34.7	0.0	0.0	n.a	0.0	0.0	0.0	36.2	0.0	29.4	0.1	100.4
MW9-W-1-1	Chalcopyrite	34.7	0.0	0.0	n.a	0.0	0.0	0.0	36.8	0.0	29.3	0.1	100.9
MW9-W-11-1	Pyrite	52.0	0.1	0.0	n.a	0.0	0.0	0.1	44.7	0.0	0.0	0.0	97.0
MW9-W-11-2	Sphalerite	33.9	0.0	0.0	n.a	0.0	0.0	0.0	11.7	0.0	0.0	54.0	99.7
COS37-1-1	Chalcopyrite	34.7	0.0	0.0	n.a	0.0	0.0	0.0	36.4	0.0	29.4	0.2	100.7
COS37-1-2	Pyrrhotite	39.8	0.0	0.0	n.a	0.0	0.0	0.1	55.9	0.0	0.0	0.0	95.8
COS37-1-3	Chalcopyrite	34.6	0.1	0.0	n.a	0.0	0.0	0.0	34.3	0.0	28.2	1.2	98.3
COS37-3-1	Pyrite	53.8	0.0	0.0	n.a	0.0	0.0	0.0	44.4	0.0	0.1	0.1	98.3
COS37-3-2	Pyrrhotite	39.9	0.0	0.0	n.a	0.0	0.0	0.0	56.8	0.0	0.0	0.0	96.8
COS37-2-1	Chalcopyrite	34.5	0.0	0.0	n.a	0.0	0.0	0.0	35.9	0.0	28.9	0.3	99.6
COS37-2-2	Chalcopyrite	34.7	0.0	0.0	n.a	0.0	0.0	0.1	36.5	0.0	29.2	0.1	100.5
COS37-2-3	Pyrrhotite	40.1	0.0	0.0	n.a	0.0	0.0	0.0	56.5	0.0	0.0	0.0	96.8
BOTE21-2b-1	Sphalerite	34.2	0.0	0.0	n.a	0.0	0.0	0.0	10.7	0.0	0.6	54.1	99.7

El Compas

Sample	Mineral	Ag	Au	S	Br	Se	Cl	Hg	Total
		W%	W%	W%	W%	W%	W%	W%	W%
09COM043	Electrum	31.1	67.8	0.1	n.a.	n.a.	n.a.	n.a.	98.9
09COM043	Aguilarite	76.9	0.0	9.1	0.0	10.8	0.2	0.1	97.0
09COM043	Aguilarite	76.7	0.0	6.9	0.0	16.5	0.1	0.2	100.3
09COM043	Aguilarite	76.0	0.0	7.0	0.0	16.5	0.1	0.2	99.8
09COM043	Aguilarite	77.6	0.0	7.4	0.0	15.4	0.1	0.2	100.7
09COM043	Aguilarite	76.6	0.0	7.2	0.0	15.8	0.1	0.0	99.7
09COM043	Aguilarite	78.3	0.2	9.3	0.0	10.5	0.2	0.1	98.6
09COM043	Aguilarite	78.4	0.0	9.6	0.0	10.0	0.2	0.1	98.4
09COM043	Aguilarite	76.9	0.1	7.7	0.0	14.7	0.1	0.2	99.7
09COM043	Aguilarite	77.4	0.0	7.5	0.0	15.1	0.1	0.3	100.5
09COM043	Aguilarite	77.6	0.0	7.7	0.0	14.5	0.1	0.2	100.1
09COM043	Aguilarite	76.9	0.0	7.8	0.0	14.1	0.1	0.2	99.2
09COM043	Aguilarite	77.3	0.0	8.4	0.0	12.6	0.1	0.2	98.7
09COM043	Aguilarite	78.5	0.0	9.0	0.0	10.9	0.1	0.1	98.6

Appendix B: Locations and descriptions of samples analyzed for geochemistry and geochronology.

Sample	Location	UTM Easting (ITRF92)	UTM Northing (ITRF92)	Sample type/hole name (depth)	Analysis	Description
ZABU-01	La Bufa dome	750195	2520755	Outcrop	Litho-geochemistry; U-Pb	Gray pale to pinkish rhyolite with an average of 2% phenocrysts (1–2 mm) of sanidine, quartz, orthoclase, and rare biotite, in a vitreous matrix.
ZASI-02	La Sierpe dike	747327	2524177	Drill hole S38 (750–758 m)	Litho-geochemistry; U-Pb	Gray to whitish rhyolite, varying in texture from aphanitic to flow banded, with <1% quartz, K-feldspar, and accessory biotite, set in a microcrystalline matrix, commonly with disseminations of very fine-grained pyrite.
ZAPA-03	El Padre dome	748383	2517921	Outcrop	Litho-geochemistry; U-Pb	Pink to reddish rhyolite with ~3% phenocrysts of sanidine, quartz, orthoclase (up to 3 mm long), and fine-grained biotite. The matrix is vitreous and shows vertical flow banding surrounding xenoliths.
ZAVI-04	La Virgen ignimbrite	746915	2515212	Outcrop	Litho-geochemistry; U-Pb	Pinkish rhyolitic welded ignimbrite containing pumice with eutaxitic texture and broken crystals of quartz, sanidine, and biotite in a partially devitrified matrix.
ZAC1-07	Mala Noche Volcano-sediments	748702	2524005	Drill hole CGS151 (15.4–27.8 m)	Litho-geochemistry	Basaltic-andesite with porphyritic texture formed by plagioclase phenocrysts in a cryptocrystalline matrix. Sample taken from the volcano-sedimentary succession.
ZAC2-08	MalaNoche Volcano-sediments	749485	2523575	Drill hole CGS154 (396–399 m)	Litho-geochemistry	Basaltic-andesite with porphyritic texture formed by plagioclase phenocrysts in a cryptocrystalline matrix. Sample taken from the volcano-sedimentary succession.
ZAC4-10	Sierpe dike	747358	2524160	Drill hole CGS41 (100–102 m)	Litho-geochemistry	Gray rhyolite with aphanitic flow banded texture and disseminations of very fine-grained pyrite
ZA01-11	El Compas Volcano-sediments	746945	2515958	Drill hole 08-COM-34 (50-50.6m)	Litho-geochemistry	Redish colour andesite with porphyritic texture formed by microlites of plagioclase in a vitreous matrix with oxidized pyrite finely disseminated
ZA02-12	El Compas Volcano-sediments	747322	2516410	Drill hole 08-COM-31 (143.5-144m)	Litho-geochemistry	Grey colour porphyritic andesite with ~10% phenocrysts of plagioclase (~3 mm in size) set in a vitreous matrix.
CGS139-210	Mala Noche	746850	2523925	Drill hole CGS139	Litho-geochemistry;	Sample of pale gray to whitish rhyolitic dike. The main phenocrysts

	dikes			(210.30–211.3 m)	U-Pb	are ~1% plagioclase (~1 mm in size) set in a cryptocrystalline silica groundmass with fine-grained disseminated pyrite. Plagioclase shows strong pervasive sericitic alteration.
CGS139-288	Mala Noche dikes	746850	2523925	Drill hole CGS139 (288.5–291.10 m)	Litho-geochemistry; U-Pb	Sample of pale gray to whitish rhyolitic dike. Phenocrysts of plagioclase (~1 mm in size) are set in a cryptocrystalline silica groundmass with fine-grained disseminated pyrite, and altered to sericite.
CGS198	Mala Noche dikes	745320	2524692	Drill hole CGS198 (267.40–269.50 m)	Litho-geochemistry	White, compact marble with a roughly equigranular texture, composed primarily of recrystallized calcite.
COM-L7	El Compas vein	747109	2515904	Level 7 underground mine (70 m)	$^{40}Ar/^{39}Ar$	Banded vein consisting of greenish quartz inter-banded with white quartz, creamy adularia, and calcite bands.
VG1B-S8	Veta Grande vein	750738	2526639	Drill hole 08VGX01B (420m)	$^{40}Ar/^{39}Ar$	Breccia vein cemented by >5% sulphides (pyrite>sphalerite>galena>argentite) and gangue minerals (quartz, calcite, adularia, and late ankerites)

Appendix C. Geochemical analyses of rocks from the Zacatecas district

Symbol	Unit	Method	Detection Limit	ZABU-01	ZASI-02	ZAPA-03	ZAVI-04	ZAC1-07	ZAC2-08	ZAC4-10	ZA01-11	ZA02-12	CGS139
SiO2	%	FUS-ICP	0.01	74.17	73.75	78.83	81.94	46.19	50.67	74.34	46.19	47.18	72.12
Al2O3	%	FUS-ICP	0.01	12.87	12.14	10.44	9.01	15.94	16.87	13.13	16.35	15.72	11.80
Fe2O3(T)	%	FUS-ICP	0.01	1.88	1.36	1.86	1.46	10.24	9.38	1.93	9.89	10.16	4.99
MnO	%	FUS-ICP	0.001	0.03	0.03	0.03	0.01	0.20	0.19	0.04	0.16	0.17	0.04
MgO	%	FUS-ICP	0.01	0.27	0.48	0.07	0.04	5.54	4.95	0.59	6.35	9.10	0.17
CaO	%	FUS-ICP	0.01	0.42	0.68	0.08	0.10	9.80	11.37	0.73	11.46	10.02	0.07
Na2O	%	FUS-ICP	0.01	1.45	1.23	0.21	0.58	3.49	1.95	1.32	2.87	1.79	0.17
K2O	%	FUS-ICP	0.01	7.27	7.23	0.28	6.86	0.83	0.75	5.86	1.32	0.71	6.74
TiO2	%	FUS-ICP	0.001	0.09	0.07	0.08	0.07	1.21	0.92	0.10	1.37	1.58	0.10
P2O5	%	FUS-ICP	0.01	0.03	0.02	0.04	0.01	0.12	0.13	0.02	0.13	0.16	0.01
LOI	%	FUS-ICP		1.44	1.87	0.77	0.34	6.31	3.43	2.55	4.86	3.84	0.40
Total	%	FUS-ICP	0.01	99.93	98.85	100.70	100.40	99.87	100.60	100.60	100.90	100.40	98.61
Au	ppb	INAA	1	< 1	< 1	< 1	64.00	< 1	< 1	< 1	< 1	< 1	22.00
Ag	ppm	INAA / TD-ICP	0.5	< 0.5	0.70	< 0.5	< 0.5	< 0.5	< 0.5	< 0.5	< 0.5	< 0.5	< 0.5
As	ppm	INAA	1	102.00	35.00	33.00	27.00	< 1	9.00	2.00	18.00	3.00	90.00
Ba	ppm	FUS-ICP	1	938.00	1473.00	901.00	97.00	63.00	135.00	954.00	90.00	187.00	1850.00
Be	ppm	FUS-ICP	1	4.00	< 1	1.00	1.00	< 1	< 1	4.00	< 1	< 1	2.00
Bi	ppm	FUS-MS	0.1	< 0.1	0.70	< 0.1	< 0.1	< 0.1	< 0.1	< 0.1	< 0.1	< 0.1	< 0.1
Br	ppm	INAA	0.5	< 0.5	< 0.5	< 0.5	< 0.5	< 0.5	< 0.5	< 0.5	< 0.5	< 0.5	< 0.5
Cd	ppm	TD-ICP	0.5	< 0.5	< 0.5	< 0.5	< 0.5	0.60	< 0.5	< 0.5	0.60	< 0.5	< 0.5
Co	ppm	INAA	0.1	1.40	16.00	1.20	1.30	41.40	35.00	1.40	42.70	42.90	4.10
Cr	ppm	INAA	0.5	< 0.5	6.60	9.10	4.50	55.80	166.00	6.30	305.00	233.00	105.00
Cs	ppm	FUS-MS	0.1	47.20	10.60	13.90	11.30	2.30	4.00	31.60	11.40	2.00	8.80
Cu	ppm	TD-ICP	1	4.00	42.00	10.00	12.00	53.00	42.00	1.00	47.00	49.00	415.00
Ga	ppm	FUS-MS	1	17.00	15.00	10.00	10.00	15.00	14.00	17.00	15.00	15.00	13.00
Ge	ppm	FUS-MS	0.5	1.90	1.10	1.40	1.50	1.50	2.30	1.50	1.30	1.30	0.90
Hf	ppm	FUS-MS	0.1	3.70	4.50	3.40	3.10	1.80	1.30	4.30	2.30	2.80	2.80
Hg	ppm	INAA	1	< 1	< 1	< 1	< 1	< 1	< 1	< 1	< 1	< 1	< 1
In	ppm	FUS-MS	0.1	< 0.1	< 0.1	< 0.1	< 0.1	< 0.1	< 0.1	< 0.1	< 0.1	< 0.1	< 0.1
Ir	ppb	INAA	1	< 1	< 1	< 1	< 1	< 1	< 1	< 1	< 1	< 1	< 1
Mo	ppm	FUS-MS	2	< 2	< 2	< 2	< 2	< 2	< 2	< 2	< 2	< 2	8.00
Nb	ppm	FUS-MS	0.2	10.00	13.40	9.90	12.00	1.30	0.70	12.50	3.60	2.20	8.70
Ni	ppm	TD-ICP	1	3.00	3.00	4.00	4.00	40.00	59.00	3.00	105.00	174.00	10.00
Pb	ppm	TD-ICP	5	25.00	14.00	14.00	13.00	< 5	< 5	7.00	< 5	< 5	21.00
Rb	ppm	FUS-MS	1	450.00	301.00	511.00	426.00	28.00	28.00	306.00	54.00	16.00	350.00
S	%	TD-ICP	0.001	0.01	0.18	0.00	0.00	0.02	0.02	0.01	0.00	0.08	1.11
Sb	ppm	INAA	0.1	35.40	4.10	73.40	12.90	0.70	2.50	1.70	2.00	1.60	3.40
Sc	ppm	INAA	0.01	3.47	3.96	3.01	3.21	38.80	36.70	3.76	37.20	29.60	3.27
Se	ppm	INAA	0.5	< 0.5	< 0.5	< 0.5	< 0.5	< 0.5	< 0.5	< 0.5	< 0.5	< 0.5	< 0.5
Sn	ppm	FUS-MS	1	< 1	6.00	7.00	< 1	< 1	1.00	8.00	< 1	2.00	4.00
Sr	ppm	FUS-ICP	2	75.00	74.00	19.00	38.00	196.00	348.00	65.00	231.00	248.00	120.00
Ta	ppm	FUS-MS	0.01	1.81	1.91	1.48	0.88	0.06	0.02	1.86	0.22	0.15	1.44
Th	ppm	FUS-MS	0.05	14.20	15.90	12.30	16.00	0.26	0.14	14.90	0.26	0.17	14.80
U	ppm	FUS-MS	0.01	4.09	6.68	4.56	3.66	1.10	1.00	5.76	0.23	0.08	5.65
V	ppm	FUS-ICP	5	6.00	< 5	20.00	24.00	364.00	281.00	5.00	248.00	256.00	7.00
W	ppm	INAA	1	< 1	< 1	< 1	10.00	< 1	< 1	< 1	< 1	< 1	< 1
Y	ppm	FUS-ICP	1	23.00	31.00	20.00	20.00	28.00	19.00	26.00	25.00	28.00	26.00
Zn	ppm	INAA / TD-ICP	1	49.00	14.00	16.00	11.00	80.00	46.00	80.00	64.00	73.00	60.00
Zr	ppm	FUS-MS	1	124.00	132.00	108.00	100.00	63.00	44.00	145.00	86.00	109.00	93.00
La	ppm	FUS-MS	0.05	45.30	45.30	36.40	38.40	3.74	2.79	44.90	4.83	4.53	39.40
Ce	ppm	FUS-MS	0.05	82.90	89.60	71.50	77.20	10.60	7.87	84.60	13.40	14.20	79.30
Pr	ppm	FUS-MS	0.01	9.55	10.30	7.91	8.74	1.70	1.27	9.39	2.11	2.33	8.67
Nd	ppm	FUS-MS	0.05	33.20	37.00	27.80	31.70	9.26	6.63	33.80	10.70	11.90	29.80
Sm	ppm	FUS-MS	0.01	5.58	7.18	4.85	5.84	3.09	2.27	6.09	3.32	3.88	5.58
Eu	ppm	FUS-MS	0.005	0.64	0.67	0.54	0.13	1.13	0.86	0.69	1.15	1.48	0.62
Gd	ppm	FUS-MS	0.01	4.38	5.99	3.85	4.27	4.05	2.99	5.15	4.01	4.75	4.39
Tb	ppm	FUS-MS	0.01	0.71	1.00	0.63	0.67	0.79	0.57	0.83	0.75	0.87	0.74
Dy	ppm	FUS-MS	0.01	4.01	5.87	3.77	3.66	5.15	3.71	4.66	4.78	5.60	4.48
Ho	ppm	FUS-MS	0.01	0.80	1.13	0.75	0.74	1.08	0.76	0.89	0.99	1.17	0.85
Er	ppm	FUS-MS	0.01	2.30	3.25	2.14	2.10	3.14	2.23	2.52	2.91	3.48	2.40
Tl	ppm	FUS-MS	0.05	3.96	2.75	8.88	2.88	0.08	0.18	1.84	0.47	0.16	3.01
Tm	ppm	FUS-MS	0.005	0.36	0.49	0.33	0.32	0.48	0.34	0.39	0.43	0.51	0.37
Yb	ppm	FUS-MS	0.01	2.49	3.15	2.29	2.13	3.26	2.30	2.63	2.76	3.27	2.47
Lu	ppm	FUS-MS	0.002	0.40	0.49	0.36	0.33	0.53	0.36	0.42	0.43	0.51	0.36

Appendix D: $^{40}Ar/^{39}Ar$ Data

Sample VG1B-38, Adularia, 8.40 mg, J = 0.001632 ± 0.20%

4 amu discrimination = 1.0565 ± 0.43%, 40/39K = 0.01738 ± 67.07%, 36/37Ca = 0.0002157 ± 8.78%, 39/37Ca = 0.0006702 ± 1.60%

step	T (C)	^{36}Ar	^{37}Ar	^{38}Ar	^{39}Ar	^{40}Ar	%^{40}Ar*	%^{39}Ar rlsd	Ca/K	^{40}Ar*/^{39}ArK	Age (Ma)	1s.d.
1	650	3.21	1.80	1.03	25.67	1267.70	52.3	2.2	0.476	28.148	81.03	0.72
2	750	2.18	2.38	1.11	50.20	1342.77	69.6	4.3	0.322	20.299	58.80	0.43
3	850	0.32	0.28	1.55	111.49	1691.85	96.7	9.5	0.017	16.027	46.58	0.27
4	920	0.23	0.21	1.93	140.97	2087.50	98.1	12.0	0.010	15.882	46.17	0.27
5	990	0.31	0.11	2.26	161.80	2411.93	97.7	13.8	0.005	15.937	46.32	0.27
6	1060	0.32	0.10	2.29	163.62	2440.30	97.7	13.9	0.004	15.937	46.32	0.28
7	1120	0.38	0.08	2.31	166.91	2502.81	97.3	14.2	0.003	15.963	46.40	0.27
8	1160	0.41	0.06	1.72	122.50	1874.66	96.3	10.4	0.003	16.062	46.68	0.28
9	1400	0.98	0.06	3.33	229.85	3577.82	95.2	19.6	0.002	16.164	46.97	0.28
					Cumulative %39Ar rlsd =			100.0		Total gas age =	47.80	0.21
										Plateau age = (steps 3-9)	46.49	0.22
										Isochron age = (steps 1-9)	42.36	0.09

Sample COM-L7, Adularia, 13.80 mg, J = 0.001655 ± 0.20%

4 amu discrimination = 1.0565 ± 0.43%, 40/39K = 0.01738 ± 67.07%, 36/37Ca = 0.0002157 ± 8.78%, 39/37Ca = 0.0006702 ± 1.60%

step	T (C)	^{36}Ar	^{37}Ar	^{38}Ar	^{39}Ar	^{40}Ar	%^{40}Ar*	%^{39}Ar rlsd	Ca/K	^{40}Ar*/^{39}ArK	Age (Ma)	1s.d.
1	650	4.20	7.04	2.52	122.72	2404.52	67.1	7.6	0.387	14.382	42.44	0.32
2	750	0.71	6.33	1.94	133.38	1513.66	91.5	8.3	0.320	11.329	33.51	0.20
3	850	0.89	0.16	2.89	202.23	2226.90	92.6	12.5	0.005	11.151	32.99	0.20
4	920	0.80	0.14	3.03	213.52	2302.69	93.6	13.2	0.004	11.034	32.65	0.20
5	990	0.61	0.12	2.89	204.99	2165.62	94.8	12.7	0.004	10.950	32.40	0.19
6	1060	0.79	0.15	3.28	230.16	2457.13	94.0	14.3	0.004	10.982	32.50	0.20
7	1120	1.21	0.14	3.23	223.32	2514.46	91.1	13.8	0.004	11.207	33.15	0.20
8	1160	1.36	0.10	2.28	151.56	1859.16	86.5	9.4	0.005	11.569	34.22	0.22
9	1200	1.26	0.07	1.45	89.60	1231.26	81.2	5.6	0.005	12.110	35.80	0.24
10	1240	0.69	0.05	0.51	28.76	474.38	74.1	1.8	0.012	13.007	38.42	0.27
11	1290	0.29	0.05	0.18	9.29	170.25	77.2	0.6	0.039	14.183	41.86	0.31
12	1400	0.25	0.05	0.10	3.68	101.40	62.1	0.2	0.083	14.033	41.42	0.47
					Cumulative %39Ar rlsd =			100.0		Total gas age =	34.02	0.14
										Plateau age = (steps 3-6)	32.63	0.20
										Isochron age = (steps 1-11)	29.19	0.10

Appendix E: U/Pb Data

Sample ZABU-01	^{206}Pb (cps)	^{204}Pb (cps)	^{207}Pb/^{206}Pb	2 σ	^{207}Pb/^{235}U	2 σ	^{206}Pb/^{238}U	2 σ	ρ	^{207}Pb*/^{206}Pb* age (Ma)	2 σ error (Ma)	^{207}Pb*/^{235}U age (Ma)	2 σ error (Ma)	^{206}Pb*/^{238}U age (Ma)	2 σ error (Ma)
ZABU-36	51632	2	0.04515	0.00078	0.04477	0.00262	0.00719	0.00040	0.956	-47	41	44	3	46	3
ZABU-40	31336	14	0.04579	0.00162	0.04622	0.00361	0.00732	0.00051	0.892	-13	83	46	3	47	3
ZABU1-23	28949	24	0.04440	0.00079	0.04497	0.00243	0.00735	0.00037	0.944	-89	43	45	2	47	2
ZABU1-5	44010	0	0.04500	0.00080	0.04566	0.00304	0.00736	0.00047	0.964	-56	43	45	3	47	3
ZABU1-30	20559	4	0.04127	0.00076	0.04203	0.00355	0.00739	0.00061	0.976	-271	46	42	3	47	4
ZABU1-6	192877	14	0.04740	0.00071	0.04872	0.00398	0.00745	0.00060	0.983	69	35	48	4	48	4
ZABU1-9	90600	0	0.04570	0.00067	0.04706	0.00254	0.00747	0.00039	0.962	-18	35	47	2	48	2
ZABU1-16	42882	51	0.04493	0.00083	0.04630	0.00253	0.00747	0.00038	0.942	-59	44	46	2	48	2
ZABU-34	36579	4	0.04321	0.00092	0.04454	0.00243	0.00748	0.00038	0.921	-155	52	44	2	48	2
ZABU1-19	27825	39	0.04349	0.00094	0.04486	0.00257	0.00748	0.00040	0.926	-140	53	45	2	48	3
ZABU1-28	44212	7	0.04520	0.00083	0.04663	0.00269	0.00748	0.00041	0.948	-45	44	46	3	48	3
ZABU1-11	36142	30	0.04447	0.00083	0.04610	0.00261	0.00752	0.00040	0.945	-85	45	46	3	48	3
ZABU1-15	68055	26	0.04579	0.00066	0.04750	0.00248	0.00752	0.00038	0.962	-13	34	47	2	48	2
ZABU-39	57419	5	0.04553	0.00065	0.04725	0.00271	0.00753	0.00042	0.968	-27	34	47	3	48	3
ZABU-33	52907	3	0.04448	0.00098	0.04621	0.00260	0.00753	0.00039	0.920	-84	53	46	3	48	2
ZABU-35	182311	5	0.04770	0.00070	0.04958	0.00412	0.00754	0.00062	0.984	85	34	49	4	48	4
ZABU1-13	35060	16	0.04441	0.00107	0.04624	0.00331	0.00755	0.00051	0.941	-88	58	46	3	48	3
ZABU1-29	24067	7	0.04194	0.00092	0.04370	0.00257	0.00756	0.00041	0.928	-230	54	43	2	49	3
ZABU1-17	103982	66	0.04646	0.00061	0.04842	0.00261	0.00756	0.00039	0.970	22	31	48	3	49	3
ZABU1-22	32668	29	0.04492	0.00077	0.04692	0.00261	0.00758	0.00040	0.951	-60	41	47	3	49	3
ZABU1-18	92784	47	0.04700	0.00070	0.04944	0.00254	0.00763	0.00038	0.957	49	35	49	2	49	2
ZABU1-14	187305	49	0.04931	0.00095	0.05192	0.00327	0.00764	0.00046	0.952	163	45	51	3	49	3
ZABU-32	109418	2	0.04725	0.00065	0.05010	0.00291	0.00769	0.00043	0.971	62	33	50	3	49	3
ZABU-31	53351	85	0.07233	0.00488	0.07671	0.00662	0.00769	0.00041	0.623	995	131	75	6	49	3
ZABU1-7	44730	1	0.04545	0.00097	0.04830	0.00293	0.00771	0.00044	0.936	-31	51	48	3	49	3
ZABU1-24	32313	30	0.04582	0.00083	0.04869	0.00293	0.00771	0.00044	0.954	-12	43	48	3	49	3
ZABU1-26	77294	24	0.04729	0.00068	0.05054	0.00290	0.00775	0.00043	0.968	64	34	50	3	50	3
ZABU1-10	91228	0	0.04564	0.00082	0.04917	0.00265	0.00781	0.00040	0.942	-22	43	49	3	50	3
ZABU1-12	95524	40	0.04744	0.00066	0.05171	0.00387	0.00791	0.00058	0.983	72	33	51	4	51	4
ZABU1-8	78847	0	0.04788	0.00085	0.05329	0.00331	0.00807	0.00048	0.958	93	41	53	3	52	3

Sample ZASI-02	^{206}Pb (cps)	^{204}Pb (cps)	^{207}Pb/^{206}Pb	2 σ	^{207}Pb/^{235}U	2 σ	^{206}Pb/^{238}U	2 σ	ρ	^{207}Pb*/^{206}Pb* age (Ma)	2 σ error (Ma)	^{207}Pb*/^{235}U age (Ma)	2 σ error (Ma)	^{206}Pb*/^{238}U age (Ma)	2 σ error (Ma)
ZASI2-1	74278	76	0.04755	0.00084	0.05061	0.00232	0.00772	0.00033	0.923	77	41	50	2	50	2
ZASI2-2	100847	76	0.04714	0.00079	0.05140	0.00242	0.00791	0.00035	0.934	56	40	51	2	51	2
ZASI2-3	50396	72	0.04714	0.00082	0.05262	0.00240	0.00810	0.00034	0.924	56	41	52	2	52	2
ZASI2-4	22524	65	0.04754	0.00091	0.05429	0.00254	0.00828	0.00035	0.913	76	45	54	2	53	2
ZASI2-5	25028	40	0.04706	0.00091	0.05178	0.00218	0.00798	0.00030	0.888	52	45	51	2	51	2
ZASI2-6	54616	56	0.04688	0.00076	0.05004	0.00251	0.00774	0.00037	0.947	43	38	50	2	50	2
ZASI2-7	70725	57	0.04698	0.00077	0.05178	0.00235	0.00799	0.00034	0.932	48	39	51	2	51	2
ZASI2-8	32616	53	0.04602	0.00091	0.05023	0.00243	0.00792	0.00035	0.913	-1	47	50	2	51	2
ZASI2-9	53429	69	0.04642	0.00081	0.05116	0.00252	0.00799	0.00037	0.935	20	42	51	2	51	2
ZASI2-10	80163	73	0.04735	0.00074	0.05230	0.00228	0.00801	0.00033	0.933	67	37	52	2	51	2
ZASI2-11	54436	89	0.04624	0.00082	0.05155	0.00251	0.00808	0.00037	0.931	10	42	51	2	52	2
ZASI2-12	54365	141	0.04696	0.00077	0.05107	0.00213	0.00789	0.00030	0.919	47	39	51	2	51	2
ZASI2-13	99085	157	0.04705	0.00074	0.05156	0.00224	0.00795	0.00032	0.932	52	37	51	2	51	2
ZASI2-14	76927	140	0.04705	0.00075	0.05107	0.00206	0.00787	0.00029	0.918	52	38	51	2	51	2
ZASI2-15	80536	152	0.04794	0.00098	0.05116	0.00250	0.00774	0.00034	0.909	96	48	51	2	50	2
ZASI2-16	104742	146	0.04691	0.00071	0.04966	0.00213	0.00768	0.00031	0.936	45	36	49	2	49	2
ZASI2-17	30785	135	0.04703	0.00162	0.04873	0.00281	0.00751	0.00035	0.803	51	80	48	3	48	2
ZASI2-18	62986	136	0.04849	0.00105	0.05346	0.00293	0.00800	0.00040	0.918	123	50	53	3	51	3
ZASI2-19	70231	132	0.04714	0.00075	0.05192	0.00244	0.00799	0.00035	0.942	56	37	51	2	51	2
ZASI2-20	29470	118	0.04760	0.00091	0.05211	0.00232	0.00794	0.00032	0.902	79	45	52	2	51	2
ZASI2-21	73792	19	0.04870	0.00142	0.05467	0.00274	0.00814	0.00033	0.813	133	67	54	3	52	2
ZASI2-23	52991	19	0.04614	0.00098	0.05151	0.00345	0.00810	0.00051	0.949	5	50	51	3	52	3
ZASI2-24	77002	18	0.04619	0.00080	0.04873	0.00302	0.00765	0.00046	0.960	8	41	48	3	49	3
ZASI2-25	77184	45	0.04717	0.00074	0.05047	0.00300	0.00776	0.00044	0.964	58	37	50	3	50	3
ZASI2-28	51491	50	0.04582	0.00080	0.04912	0.00245	0.00777	0.00036	0.937	-12	42	49	2	50	2
ZASI2-31	102374	19	0.04711	0.00079	0.05326	0.00407	0.00820	0.00061	0.976	55	40	53	4	53	4
ZASI2-32	54837	33	0.04610	0.00075	0.04958	0.00218	0.00780	0.00032	0.929	3	39	49	2	50	2
ZASI2-36	85335	33	0.04690	0.00076	0.05039	0.00217	0.00779	0.00031	0.927	44	38	50	2	50	2
ZASI2-37	26769	27	0.04777	0.00141	0.05252	0.00276	0.00797	0.00035	0.827	88	69	52	3	51	2

Sample ZAPA-03	^{206}Pb (cps)	^{204}Pb (cps)	^{207}Pb/^{206}Pb	2 σ	^{207}Pb/^{235}U	2 σ	^{206}Pb/^{238}U	2 σ	ρ	^{207}Pb*/^{206}Pb* age (Ma)	2 σ error (Ma)	^{207}Pb*/^{235}U age (Ma)	2 σ error (Ma)	^{206}Pb*/^{238}U age (Ma)	2 σ error (Ma)
ZAPA03-13	36325	111	0.05081	0.00095	0.04736	0.00313	0.00676	0.00043	0.959	232	43	47	3	43	3
ZAPA03-23	35858	105	0.04989	0.00078	0.04731	0.00186	0.00688	0.00025	0.917	190	36	47	2	44	2
ZAPA03-25	21305	71	0.05178	0.00107	0.04912	0.00217	0.00688	0.00027	0.884	276	47	49	2	44	2
ZAPA03-6	32147	83	0.05470	0.00112	0.05196	0.00301	0.00689	0.00037	0.935	400	45	51	3	44	2
ZAPA03-8	22932	63	0.05192	0.00091	0.04969	0.00256	0.00694	0.00034	0.940	282	40	49	2	45	2
ZAPA03-20	37853	137	0.05579	0.00222	0.05350	0.00289	0.00696	0.00025	0.678	444	86	53	3	45	2
ZAPA03-21	44709	140	0.04985	0.00083	0.04784	0.00203	0.00696	0.00027	0.919	188	38	47	2	45	2
ZAPA03-1	30275	138	0.04980	0.00194	0.04797	0.00480	0.00699	0.00064	0.921	186	88	48	5	45	4
ZAPA03-26	31613	123	0.06130	0.00238	0.05916	0.00333	0.00700	0.00029	0.725	650	81	58	3	45	2
ZAPA03-7	107779	84	0.04920	0.00071	0.04802	0.00224	0.00708	0.00031	0.950	157	34	48	2	45	2
ZAPA03-2	32670	92	0.05004	0.00080	0.04891	0.00232	0.00709	0.00032	0.942	197	37	48	2	46	2
ZAPA03-5	172927	71	0.04717	0.00052	0.04626	0.00210	0.00711	0.00031	0.971	58	26	46	2	46	2
ZAPA03-18	50234	183	0.05398	0.00256	0.05297	0.00324	0.00712	0.00027	0.631	370	103	52	3	46	2
ZAPA03-9	40495	46	0.05027	0.00116	0.04959	0.00247	0.00716	0.00032	0.886	207	53	49	2	46	2
ZAPA03-19	82227	101	0.04999	0.00096	0.04943	0.00211	0.00717	0.00027	0.892	194	44	49	2	46	2
ZAPA03-10	44496	92	0.05398	0.00149	0.05344	0.00278	0.00718	0.00032	0.847	370	61	53	3	46	2
ZAPA03-4	33905	75	0.05012	0.00099	0.04983	0.00268	0.00721	0.00036	0.930	201	45	49	3	46	2
ZAPA03-16	38811	138	0.05651	0.00265	0.05622	0.00322	0.00722	0.00024	0.576	473	100	56	3	46	2
ZAPA03-27	39044	88	0.05418	0.00166	0.05418	0.00269	0.00725	0.00028	0.786	378	68	54	3	47	2
ZAPA03-28	120340	147	0.05640	0.00283	0.05650	0.00339	0.00726	0.00024	0.550	468	107	56	3	47	2
ZAPA03-12	30594	223	0.08636	0.00631	0.08734	0.00730	0.00733	0.00030	0.485	1346	135	85	7	47	2
ZAPA03-15	65649	244	0.06702	0.00594	0.06972	0.00670	0.00754	0.00028	0.387	838	174	68	6	48	2
ZAPA03-22	109232	154	0.04877	0.00086	0.05105	0.00404	0.00759	0.00059	0.975	137	41	51	4	49	4
ZAPA03-11	25152	213	0.07978	0.00863	0.08532	0.01029	0.00776	0.00041	0.443	1191	200	83	10	50	3
ZAPA03-14	27151	97	0.05492	0.00135	0.15374	0.01033	0.02030	0.00127	0.930	409	54	145	9	130	8
ZAPA03-17	96133	120	0.04985	0.00059	0.14236	0.00569	0.02071	0.00079	0.956	188	27	135	5	132	5
ZAPA03-3	32339	78	0.05278	0.00070	0.15689	0.01089	0.02156	0.00147	0.982	319	30	148	10	137	9
ZAPA03-29	116974	352	0.07898	0.00740	0.25617	0.02636	0.02352	0.00100	0.413	1172	175	232	21	150	6

Sample ZAVI-04	^{206}Pb (cps)	^{204}Pb (cps)	^{207}Pb/^{206}Pb	2 σ	^{207}Pb/^{235}U	2 σ	^{206}Pb/^{238}U	2 σ	ρ	^{207}Pb*/^{206}Pb* age (Ma)	2 σ error (Ma)	^{207}Pb*/^{235}U age (Ma)	2 σ error (Ma)	^{206}Pb*/^{238}U age (Ma)	2 σ error (Ma)
ZAVI04-26	16332	96	0.05191	0.00121	0.04395	0.00315	0.00614	0.00042	0.946	282	52	44	3	39	3
ZAVI04-9	15059	97	0.05341	0.00115	0.04554	0.00263	0.00618	0.00033	0.928	346	48	45	3	40	2
ZAVI04-15	15539	95	0.05786	0.00210	0.04938	0.00371	0.00619	0.00041	0.876	524	78	49	4	40	3
ZAVI04-6	16265	106	0.05329	0.00159	0.04631	0.00310	0.00630	0.00038	0.895	341	66	46	3	41	2
ZAVI04-18	10764	91	0.05705	0.00141	0.04982	0.00270	0.00633	0.00031	0.890	494	54	49	3	41	2
ZAVI04-28	17007	103	0.05162	0.00113	0.04522	0.00276	0.00635	0.00036	0.933	269	50	45	3	41	2
ZAVI04-10	16310	100	0.05275	0.00143	0.04653	0.00330	0.00640	0.00042	0.924	318	60	46	3	41	3
ZAVI04-16	19620	115	0.05118	0.00086	0.04559	0.00260	0.00646	0.00035	0.956	249	38	45	3	42	2
ZAVI04-24	16825	93	0.05227	0.00127	0.04691	0.00313	0.00651	0.00040	0.931	297	55	47	3	42	3
ZAVI04-30	13684	90	0.05271	0.00098	0.04734	0.00238	0.00651	0.00030	0.929	316	42	47	2	42	2
ZAVI04-29	15442	116	0.05609	0.00190	0.05069	0.00399	0.00655	0.00047	0.903	456	73	50	4	42	3
ZAVI04-13	17836	98	0.05377	0.00167	0.04879	0.00290	0.00658	0.00033	0.854	362	68	48	3	42	2
ZAVI04-31	11075	92	0.05518	0.00141	0.05010	0.00282	0.00658	0.00033	0.891	420	56	50	3	42	2
ZAVI04-8	19302	106	0.05291	0.00157	0.04804	0.00295	0.00659	0.00035	0.875	325	66	48	3	42	2
ZAVI04-21	11846	94	0.05517	0.00136	0.05023	0.00300	0.00660	0.00036	0.911	419	54	50	3	42	2
ZAVI04-3	13127	82	0.05414	0.00156	0.04934	0.00339	0.00661	0.00041	0.907	377	64	49	3	42	3
ZAVI04-22	15589	103	0.05295	0.00139	0.04827	0.00246	0.00661	0.00029	0.856	326	59	48	2	42	2
ZAVI04-1	12509	112	0.05530	0.00208	0.05045	0.00393	0.00662	0.00045	0.876	424	82	50	4	43	3
ZAVI04-25	8260	92	0.05855	0.00177	0.05363	0.00286	0.00664	0.00029	0.824	551	65	53	3	43	2
ZAVI04-7	12676	109	0.05618	0.00196	0.05199	0.00343	0.00671	0.00038	0.849	460	76	51	3	43	2
ZAVI04-20	11470	95	0.05575	0.00122	0.05163	0.00268	0.00672	0.00032	0.906	442	48	51	3	43	2
ZAVI04-17	14293	109	0.05381	0.00103	0.05003	0.00277	0.00674	0.00035	0.938	363	43	50	3	43	2
ZAVI04-5	14242	106	0.05468	0.00216	0.05109	0.00375	0.00678	0.00042	0.843	399	86	51	4	44	3
ZAVI04-2	11397	90	0.05575	0.00140	0.05209	0.00306	0.00678	0.00036	0.904	442	55	52	3	44	2
ZAVI04-14	10957	109	0.05744	0.00221	0.05452	0.00340	0.00688	0.00034	0.786	508	83	54	3	44	2

sample CGS139_210	^{206}Pb (cps)	^{204}Pb (cps)	^{207}Pb/^{206}Pb	2 σ	^{207}Pb/^{235}U	2 σ	^{206}Pb/^{238}U	2 σ	ρ	^{207}Pb*/^{206}Pb* age (Ma)	2 σ error (Ma)	^{207}Pb*/^{235}U age (Ma)	2 σ error (Ma)	^{206}Pb*/^{238}U age (Ma)	2 σ error (Ma)
S139-210-1	17973	47	0.04954	0.00162	0.05394	0.00282	0.00790	0.00032	0.780	173	75	53	3	51	2
S139-210-4	23406	75	0.05039	0.00219	0.05428	0.00338	0.00781	0.00035	0.715	213	98	54	3	50	2
S139-210-5	22583	83	0.04914	0.00133	0.05115	0.00247	0.00755	0.00030	0.828	155	62	51	2	48	2
S139-210-6	53498	97	0.04780	0.00048	0.05142	0.00191	0.00780	0.00028	0.963	89	24	51	2	50	2
S139-210-8	17626	102	0.06353	0.00504	0.06800	0.00585	0.00776	0.00026	0.388	726	160	67	6	50	2
S139-210-9	11754	73	0.05243	0.00390	0.05618	0.00484	0.00777	0.00034	0.504	304	161	55	5	50	2
S139-210-10	44922	71	0.04794	0.00060	0.05131	0.00210	0.00776	0.00030	0.952	96	29	51	2	50	2
S139-210-11	16568	57	0.05055	0.00131	0.05442	0.00274	0.00781	0.00034	0.857	220	59	54	3	50	2
S139-210-12	98659	51	0.04920	0.00076	0.05309	0.00179	0.00783	0.00023	0.887	157	36	53	2	50	1
S139-210-13	23230	56	0.05230	0.00115	0.05469	0.00257	0.00758	0.00032	0.884	298	49	54	2	49	2
S139-210-14	22298	68	0.04837	0.00090	0.05280	0.00197	0.00792	0.00026	0.867	117	43	52	2	51	2
S139-210-15	43504	65	0.04785	0.00062	0.05249	0.00216	0.00796	0.00031	0.950	92	30	52	2	51	2
S139-210-16	13698	57	0.05109	0.00264	0.05431	0.00348	0.00771	0.00029	0.591	245	115	54	3	50	2
S139-210-17	5013	63	0.07084	0.00327	0.07557	0.00468	0.00774	0.00032	0.667	953	92	74	4	50	2
S139-210-18	40635	55	0.04954	0.00077	0.05482	0.00228	0.00803	0.00031	0.928	174	36	54	2	52	2
S139-210-19	18050	71	0.04869	0.00160	0.05233	0.00317	0.00780	0.00040	0.841	133	75	52	3	50	3
S139-210-20	4545	53	0.06694	0.00480	0.07292	0.00572	0.00790	0.00025	0.402	836	143	71	5	51	2
S139-210-21	7316	62	0.05222	0.00276	0.05853	0.00388	0.00813	0.00032	0.601	295	117	58	4	52	2
S139-210-23	33283	42	0.04818	0.00076	0.05420	0.00217	0.00816	0.00030	0.920	108	37	54	2	52	2
S139-210-24	136273	66	0.04824	0.00052	0.05324	0.00256	0.00800	0.00038	0.975	111	25	53	2	51	2
S139-210-25	35324	68	0.04953	0.00094	0.05615	0.00333	0.00822	0.00046	0.947	173	44	55	3	53	3
S139-210-28	11197	67	0.05270	0.00261	0.05909	0.00414	0.00813	0.00040	0.706	316	109	58	4	52	3
S139-210-30	17940	45	0.05211	0.00247	0.05638	0.00361	0.00785	0.00034	0.671	290	105	56	3	50	2

sample CGS139_288	^{206}Pb (cps)	^{204}Pb (cps)	^{207}Pb/^{206}Pb	2 σ	^{207}Pb/^{235}U	2 σ	^{206}Pb/^{238}U	2 σ	ρ	^{207}Pb*/^{206}Pb* age (Ma)	2 σ error (Ma)	^{207}Pb*/^{235}U age (Ma)	2 σ error (Ma)	^{206}Pb*/^{238}U age (Ma)	2 σ error (Ma)
S139-288-1	12194	148	0.05421	0.00544	0.05820	0.00625	0.00779	0.00030	0.356	380	211	57	6	50	2
S139-288-2	27682	106	0.04971	0.00169	0.05369	0.00291	0.00783	0.00033	0.779	181	77	53	3	50	2
S139-288-4	47568	67	0.04795	0.00119	0.05306	0.00287	0.00803	0.00039	0.888	97	58	52	3	52	2
S139-288-5	38040	83	0.04848	0.00126	0.05450	0.00300	0.00815	0.00040	0.882	123	60	54	3	52	3
S139-288-6	15265	26	0.04797	0.00089	0.05084	0.00238	0.00769	0.00033	0.919	98	43	50	2	49	2
S139-288-7	217563	101	0.05169	0.00072	0.05749	0.00243	0.00807	0.00032	0.944	272	32	57	2	52	2
S139-288-8	24414	26	0.04962	0.00147	0.05457	0.00281	0.00798	0.00034	0.818	177	68	54	3	51	2
S139-288-10	59996	28	0.04929	0.00103	0.05364	0.00225	0.00789	0.00029	0.867	162	48	53	2	51	2
S139-288-11	23394	21	0.04918	0.00064	0.05282	0.00226	0.00779	0.00032	0.952	156	30	52	2	50	2
S139-288-12	228065	366	0.06184	0.00572	0.06749	0.00670	0.00791	0.00029	0.363	669	187	66	6	51	2
S139-288-13	51856	19	0.05054	0.00141	0.05620	0.00276	0.00806	0.00033	0.824	220	63	56	3	52	2
S139-288-14	51856	22	0.04986	0.00141	0.05277	0.00267	0.00768	0.00032	0.830	188	64	52	3	49	2
S139-288-15	94147	24	0.04870	0.00068	0.05096	0.00262	0.00759	0.00038	0.963	134	32	50	3	49	2
S139-288-16	15796	21	0.04902	0.00112	0.05180	0.00303	0.00766	0.00041	0.921	149	53	51	3	49	3
S139-288-18	29892	27	0.04831	0.00065	0.05255	0.00283	0.00789	0.00041	0.968	114	31	52	3	51	3
S139-288-20	119873	103	0.06085	0.00201	0.07082	0.00355	0.00844	0.00032	0.752	634	70	69	3	54	2
S139-288-21	25834	14	0.05095	0.00189	0.05490	0.00289	0.00781	0.00029	0.711	239	83	54	3	50	2
S139-288-22	105200	5	0.04843	0.00047	0.05172	0.00260	0.00774	0.00038	0.981	120	23	51	3	50	2
S139-288-23	50393	11	0.04902	0.00100	0.05300	0.00236	0.00784	0.00031	0.890	149	47	52	2	50	2
S139-288-24	37161	34	0.07659	0.00439	0.08753	0.00622	0.00829	0.00035	0.591	1111	110	85	6	53	2
S139-288-25	101341	11	0.04775	0.00055	0.05174	0.00212	0.00786	0.00031	0.959	87	27	51	2	50	2
S139-288-26	26318	2	0.04851	0.00095	0.05147	0.00228	0.00770	0.00031	0.896	124	46	51	2	49	2
S139-288-28	76552	8	0.04766	0.00051	0.05180	0.00229	0.00788	0.00034	0.970	83	25	51	2	51	2
S139-288-29	26784	1	0.05432	0.00105	0.05757	0.00260	0.00769	0.00031	0.904	384	43	57	2	49	2
S139-288-30	171197	403	0.07550	0.01194	0.08369	0.01369	0.00804	0.00034	0.256	1082	288	82	13	52	2

Note: ^{207}Pb/^{206}Pb ratios are not corrected for common lead.